

A MAGNETIC α - ω DYNAMO IN AGN DISKS. II. MAGNETIC FIELD GENERATION, THEORIES, AND SIMULATIONS

VLADIMIR I. PARIEV^{1,2} AND STIRLING A. COLGATE

Theoretical Astrophysics Group, T-6, Los Alamos National Laboratory, Los Alamos, NM

AND

J. M. FINN

Plasma Theory Group, T-15, Los Alamos National Laboratory, Los Alamos, NM

Received 2005 July 5; accepted 2006 November 1

ABSTRACT

We show that a dynamo can be produced in an active galactic nucleus (AGN) accretion disk by the Keplerian shear and the helical motions of expanding and twisting plumes of plasma heated by many star passages through the disk. Each plume rotates a fraction of the toroidal flux into poloidal flux, always in the same direction, through a finite angle, and proportional to its diameter. The predicted growth rate of poloidal magnetic flux, based on two analytic approaches and numerical simulations, leads to a rapid exponentiation of a seed field, ~ 0.1 to ~ 0.01 per Keplerian period at the inner part of the disk. The initial value of the seed field may therefore be arbitrarily small, yet through dynamo gain reach saturation very early in the disk history. Because of tidal disruption of stars close to the black hole, the maximum growth rate occurs at a radius of about 100 gravitational radii from the central object. The generated mean magnetic field, a quadrupole field, has predominantly even parity, so that the radial component does not reverse sign across the midplane. The linear growth is predicted to be the same by three different theoretical analyses: the flux conversion model, the mean field approach, and numerical modeling. The common feature is the conducting fluid flow (considered in Paper I), where two coherent large-scale flows occur naturally, the differential winding of Keplerian motion and differential rotation of expanding plumes.

Subject headings: accretion, accretion disks — galaxies: active — magnetic fields

1. INTRODUCTION

A magnetic dynamo is the most plausible mechanism for amplification of magnetic fields in galaxies and clusters of galaxies. There are numerous monographs and review articles devoted to magnetic dynamos in astrophysics; see, e.g., Parker (1979), Moffatt (1978), Stix (1975), Cowling (1981), Roberts & Soward (1992), Childress et al. (1990), Zeldovich et al. (1983), Priest (1982), Busse (1991), Krause & Rädler (1980), Biskamp (1993), and Mestel (1999). Despite a long history and many developments, a number of key issues in the dynamo theory remain unsolved, and hundreds of research papers are published each year in attempts to gain a better understanding of how magnetic dynamos work. Specifically, Chakrabarti et al. (1994) pointed out that the magnetic fields can be generated in the central parts of black hole accretion disks in active galactic nuclei (AGNs), and Colgate & Li (1997) mentioned the need for and possibility of a robust dynamo in AGN accretion disks. Dynamos have also been observed in the laboratory in the Riga experiment (Gailitis et al. 2000, 2001) and the Karlsruhe experiment (Stieglitz & Müller 2001), although these flows only partially simulate astrophysical ones. Flows resulting in a dynamo are essentially three-dimensional (3D) and often, especially under astrophysical circumstances, are chaotic or turbulent.

The shear in a rotating conducting fluid amplifies the magnetic field in a direction perpendicular to the shear and facilitates the growth of the magnetic field. Originally, Parker (1955) proposed a combination of the effects of kinetic helicity of the small-scale

motions of the fluid with the differential rotation to generate large-scale magnetic fields in the Sun. Here we consider just such a dynamo in an application to the differentially rotating flow in the accretion disk around central massive black holes (CMBHs) in the centers of galaxies. The necessary and robust source of helicity is provided by the rising and expanding plumes of the gas heated by the stars' passing through the accretion disk. This property of the rotation of expanding plumes in a rotating frame is discussed at length in Paper I (Pariev & Colgate 2007). This natural and unique coherent flow is supported by experimental evidence (Beckley et al. 2003) and is fundamental to the origin of a robust dynamo in an AGN accretion disk.

The magnetic dynamo in the disk is the essential part of the whole emerging picture of the formation and function of AGNs, and is closely related to the production of magnetic fields within galaxies and clusters of galaxies, as well as the still greater energies and fluxes in the intergalactic medium. Black hole formation, Rossby wave torquing of the accretion disk (Lovelace et al. 1999; Li et al. 2000, 2001a; Colgate et al. 2003), jet formation (Li et al. 2001b), magnetic field redistribution by reconnection and flux conversion, and finally particle acceleration in the radio lobes and jets are the key aspects of this scenario (Colgate & Li 1999; Colgate et al. 2001). Finally, we note that if almost every galaxy contains a CMBH and that if a major fraction of the free energy of its formation is converted into magnetic energy, then only a small fraction of this magnetic energy, as seen in the giant radio lobes (Kronberg et al. 2001), is sufficient to suggest possible feedback in structure formation and in galaxy formation.

This work is arranged as follows: in § 2 we briefly overview the ingredients of the star-disk collision dynamo, with a brief review of the disk conditions and star-disk collisions from Paper I; in § 3 we introduce the flux conversion dynamo analysis with a

¹ Lebedev Physical Institute, Moscow, Russia.

² Currently at Physics Department, University of Wisconsin-Madison, Madison, WI.

discussion of the necessary reconnection and turbulence-driven resistivity; in § 4 the mean field theory is developed; in § 5 the dynamo equations and numerical method are developed; and in § 6 the results of numerical calculations are presented in support of all three approaches. Finally, we end with the conclusions in § 7. We use cgs units throughout the paper.

2. THE INGREDIENTS OF THE STAR-DISK COLLISIONS DYNAMO

A poloidal magnetic field can be one of two types, distinguished by the reflectional symmetry in the equatorial plane: quadrupole (or even) and dipole (or odd). The radial component of a quadrupole field has the same sign above and below the disk plane. The radial component of the dipole field changes sign under the reflection in the disk plane, and vanishes exactly at the disk plane. Rigorous definitions and properties of the odd and even fields are given in Appendix A. As is evident in Figure 1a, the quadrupole field has a large radial component, both within and external to the disk, and it maintains the same radial direction in both spaces. On the other hand, the differential shear of a dipole field, symmetric about the midplane and therefore having no radial component, does not result in winding of the flux within the disk and therefore does not have toroidal gain. Various multipoles higher than the quadrupole have an alternating radial component as a function of radius and therefore a greater possibility of cancellation by reconnection. Differential winding of a symmetric poloidal field by the Keplerian flow results in a uniform toroidal field having the same direction over the disk height and within the disk (Fig. 1b). An α -deformation resulting in a large-scale helicity, on a scale comparable to the radius of the disk, will transform the toroidal field into a poloidal field. This transformed field, or new poloidal flux, must have the same polarity as the original poloidal flux. Then the closure of the dynamo cycle demands that this transformed flux be merged or reconnected with the original poloidal flux, so that it is augmented and hence produces gain. If this transformed flux alternates directions (as would be the case for a dipole field across the thickness of a disk), then the merged flux will be averaged to near zero. Only in the case of the quadrupole field is there a possibility of a coherent addition to the original poloidal field, when the α -deformation, as produced by star-disk collisions, changes sign across the midplane and further rotates only $\pi/2$ radians. We note that star collisions in the opposite, axial, direction equally contribute to the quadrupole poloidal flux. Far above the surface of the disk, the toroidal field produced by the shear of differential rotation from the quadrupole field (Fig. 1b) has in the opposite direction from that inside the disk. The opposite direction of the toroidal field above the disk is not shown in these drawings because, in addition to the dynamo, it presumes the formation of a force-free oppositely directed helix in the conducting half-space above and below the disk. We have, however, predicted and calculated this force-free helix (Li et al. 2001b), and furthermore, as mentioned above, we associate partial dissipation of its free energy with the visible structure of AGN jets. However, the magnitude of the quadrupole field in the region closer to the disk surface and to the midplane should be stronger (as computations actually prove). Therefore, the α -deformation will primarily take the bottom portion of the quadrupole flux and convert it into radial flux above the disk plane directed in the same way as the upper portion of the quadrupole field (Fig. 1d). Therefore, in the accretion disk dynamo, plumes from star-disk collisions entrain and rotate toroidal flux originating primarily from within the disk by $\sim\pi/2$ radians (Fig. 1c). Furthermore, these plumes terminate close to or not far above the

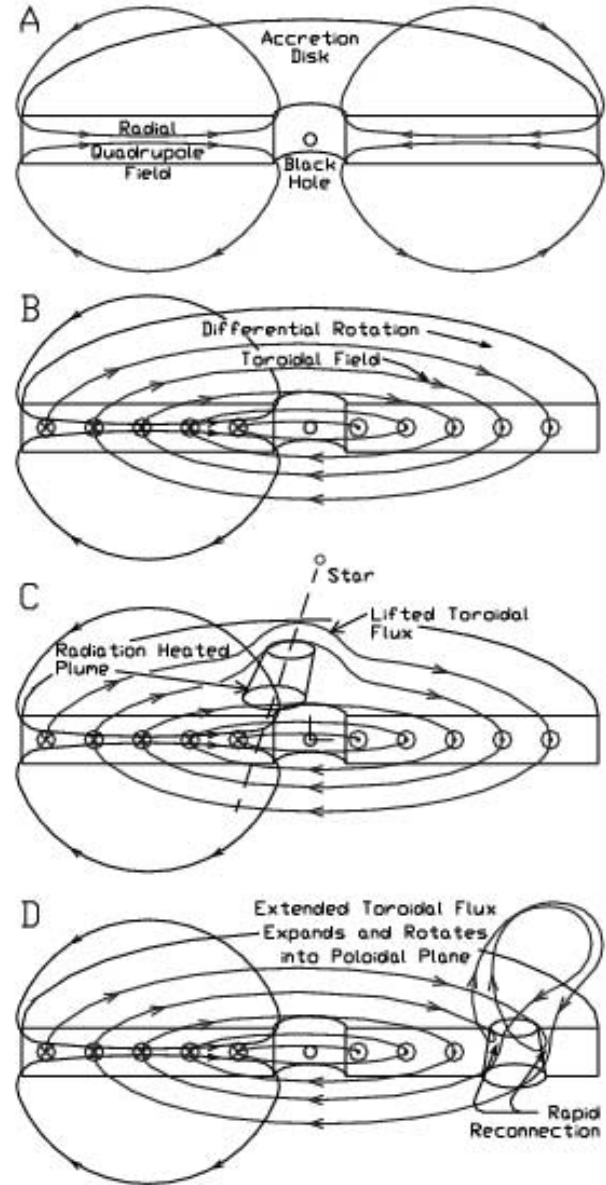


FIG. 1.— α - ω dynamo in a galactic black hole accretion disk. The radial component of the poloidal quadrupole field within the disk (A) is sheared by the differential rotation within the disk, developing a stronger toroidal component (B). As a star passes through the disk it heats, by shock and by radiation, a fraction of the matter of the disk, which expands vertically and lifts a fraction of the toroidal flux within an expanding plume (C). Due to the conservation of angular momentum, the expanding plume and embedded flux rotate $\sim\pi/2$ radians before the matter in the plume and embedded flux falls back to the disk (D). Reconnection allows the new poloidal flux to merge with and augment the original poloidal flux (D).

surface of the disk, and so produce negligible rotation of flux not as displaced from the disk. We then expect this rotated flux, before rotating another π radians, and so before self-cancellation, to reconnect as loops of poloidal flux (Fig. 1d). These loops of flux now merge with the initial poloidal field (Fig. 1a), thereby completing the cycle. To proceed with the dynamo problem, we need to use the following results from Paper I:

1. The distribution of stars in coordinate and velocity space in the central star cluster of an AGN.
2. The velocity and density of the plasma in the disk and in the corona of the disk.

3. The hydrodynamics of the flow resulting from the passage of the star through the disk, i.e., the plumes.

We briefly review the properties of the plumes produced by the star-disk collisions as they relate to the dynamo. Then with these results we estimate the conductivity in order to develop a flux rotation theory of the dynamo.

2.1. The Untwisting or Helicity Generation by the Plume

Let us first introduce a term that is used frequently below. Because of the high conductivity of the plasma considered in this paper, the magnetic field is close to a “frozen-in” state, in which the magnetic field lines follow the motions of the plasma. Imagine now a closed contour attached to the particles of plasma with some magnetic flux passing through this contour. Let us also draw this contour such that it is close to being a plane contour. As the result of plasma motions, this contour can be rotated by some angle. If this rotation happens quickly enough, so that no substantial magnetic field crosses the contour due to diffusion, the magnetic flux passing through this closed contour remains almost unchanged. The component of the magnetic field normal to the plane of the contour and averaged over the surface of the closed contour should have rotated by the same angle as the contour. We call this process “flux rotation.”

We describe the number density of the central stellar cluster and the kinematics of the stellar orbits in Paper I. The most important result of this consideration is that the rate at which stars cross the unit area of the disk surface peaks at a radial distance of about $100\text{--}200 r_g$ from the CMBH, where $r_g = 2GM/c^2 = 3.0 \times 10^{13} M_8 \text{ cm} = 9.5 \times 10^{-6} M_8 \text{ pc}$ is the gravitational radius of the CMBH and M_8 is the mass M of the CMBH expressed in units of 10^8 solar masses: $M_8 = M/10^8 M_\odot$. The rate of star-disk collisions closer to the CMBH than $100 r_g$ is depleted because of the tidal destruction of stars in the gravitational field of the CMBH and because of the grinding of the star orbits into the accretion disk plane. This grinding occurs because of the action of drag, which every star experiences on its passage through the accretion disk. After many passages this drag causes the inclined Keplerian orbit of a star to become coplanar with the disk plane, and the star becomes trapped inside the disk.

The physics and dynamics of a star-disk collision are also considered in Paper I. Here we briefly summarize the results of Paper I for the convenience of the reader. A star collides with the disk at a typical velocity of $5 \times 10^3\text{--}10^4 \text{ km s}^{-1}$. The velocity of escape from the surface of a solar-like star is 600 km s^{-1} . This is 1 order of magnitude smaller than the velocity of the star moving through the gas in the accretion disk. Also, the sound speed in the accretion disk at a radial distance of $\sim 200 r_g$ is $\sim 50 \text{ km s}^{-1}$ (see the Appendix in Paper I for details and more accurate numbers). Therefore, the gravitational field of the star itself does not influence a highly supersonic flow of gas onto the star. In this regard, the physics of a star-disk collision is radically different from the physics of the classical accretion process on either the moving or the resting star. The classical theory of accretion of interstellar gas with zero angular momentum onto stars was developed in Bondi & Hoyle (1944), Bondi et al. (1947), Bondi (1952), and McCrea (1953). Since the peculiar velocities of stars in the Galaxy are much less than 600 km s^{-1} and the sound speed in the interstellar material is also much less than 600 km s^{-1} , the gravitational potential of a star dominates the dynamics of the accretion flow in the near proximity of a star. The radius of the gravitational capture of the gas is much larger than the radius of the star. Captured gas falls almost radially down to the star surface. The presence of a small asymmetry or nonhomogeneity of the surrounding

gas causes nonzero angular momentum, which strongly influence the dynamics of the accretion flow below the gravitational capture radius.

The term “collision” rather than “accretion” is much more appropriate for the description of the interaction of a passing star with the accretion disk. Because of the high velocity of the star, the cross section of the interaction of a star with the gas is equal to the geometric cross section of a star. The high ram pressure of the incoming stream, with the density $\sim 10^{-8}$ to $\sim 10^{-10} \text{ g cm}^{-3}$, strips away the outer layer of a star. The underlying layers, with temperature $\sim 10^6 \text{ K}$ and density $\sim 10^{-5} \text{ g cm}^{-3}$, are exposed. This picture is completely different from the physics of the mixing of the radial accretion stream with the stellar (solar) atmosphere in classical accretion theory as described by Hoyle (1949). A radiation shock is formed in front of the star and a channel of the hot gas is left behind the star. This channel expands sideways inside the accretion disk and heats the surrounding gas. The hot gas is subject to a buoyancy force acting away from the equatorial plane of the disk. As a result of this force, two plumes rising from the two sides of the accretion disk are formed at the location of the star-disk crossing. Note that the amount of gas in the rising plumes and the size of the plumes are much larger than the initial mass and size of the hot channel made by the star.

As explained in Paper I, the plume should expand to several times its original radius by the time it reaches a height of order $2H$ above the disk surface, where H is the semithickness of the disk. The corresponding increase in the moment of inertia of the plume and the conservation of the angular momentum of the plume causes the plume to rotate more slowly relative to the inertial frame. From the viewpoint of the observer in the frame corotating with the Keplerian flow at the radius of the disk at the location of the plume, this means that the plume rotates in a direction opposite to the Keplerian rotation, with an angular velocity equal to some fraction of the local Keplerian angular velocity that depends on the radial expansion ratio. Since the expansion of the plume will not be infinite in the rise and fall time of π radians of the Keplerian rotation of the disk, we expect that the average of the plume rotation will be correspondingly less, or $\Delta\phi < \pi$ or $\sim \pi/2$ radians. Any force or frictional drag that resists this rotation will be countered by the Coriolis force. Finally, we note that kinetic helicity is proportional to

$$h = \mathbf{v} \cdot (\nabla \times \mathbf{v}). \quad (1)$$

For the dynamo, we require one additional dynamic property of the plumes. This is, that the total rotation angle must be finite and preferably $\simeq \pi/2$ radians; otherwise, at a larger angle or after many turns, the vector of the entrained magnetic field would average to a small value, and consequently the dynamo growth rate would be correspondingly small. This property of finite rotation, $\Delta\phi \sim \pi/2$ radians, is a natural property of plumes produced above a Keplerian disk.

Thus, we have derived the approximate properties of an accretion disk around a massive black hole: the high probability of star-disk collisions and the three necessary properties of the resulting plumes, all of which are necessary for a robust dynamo. What is missing from this description is the necessary electrical properties of the medium.

3. THE FLUX ROTATION DYNAMO

3.1. The Conductivity of the Disk and the Corona

Dynamos producing large-scale magnetic fields require a compromise between high and low conductivity. A poor conductor or

an insulator will not allow the field to be dragged with the motion of the medium. Ohmic dissipation will cause the magnetic field to decay, and, if sufficiently rapid, no dynamo will be possible. In the limit of very high conductivity, kinematic exponential growth of the magnetic field has been predicted to occur in the presence of random or chaotic three-dimensional motions of the medium (e.g., Zeldovich et al. 1983; Roberts & Soward 1992). The problem with analytic three-dimensional motions is that, being described as kinematic, they are reversible in the sense that little or no entropy is generated by the motions themselves. The field can be unwrapped by a “non-Maxwell” demon following the line of force. Since the “demon” does not have to “throw away” any information in following the reverse path, no entropy is generated. The chaotic behavior in the time of kinematic mathematically reversible motions does not create entropy because of the time reversal invariance of the equations. The plumes from star-disk collisions indeed occur randomly in time, but since the initial state is as random as the final state, no entropy is generated by just the randomness in time of the plumes themselves. By comparison, if the initial state were a large-amplitude coherent wave, then phase scrambling would indeed alter the entropy, but by a relatively small amount compared to a scattering process that leads to a Maxwell distribution. This lack of a change in entropy is then equivalent to laminar flow (without molecular diffusion) where mixing is reversible. By contrast, the randomness created by fluid turbulence is irreversible, satisfying a principle of maximizing the dissipation of the free energy of shear flow in a fluid. The plumes, although random in time, result in a coherent addition of poloidal flux because every plume translates axially, expands radially, and rotates through nearly the same angle, $\sim \pi/2$.

The negative effect of turbulence on dynamo gain has been documented in three major liquid sodium dynamo experiments: Lyon, Cadarache (Bourgoin et al. 2002), Maryland (Sisan et al. 2004), and Madison (Nornberg et al. 2006; Spence et al. 2006), all using similar flow configurations. Numerous theoretical simulations of these flows, the Dudley-James flow in a sphere (Dudley & James 1989) or the similar von Kármán flow in a cylinder (i.e., two counterrotating radially converging and axially diverging flows) in the kinematic or laminar limit, have been performed: Lyon, Cadarache (Bourgoin et al. 2002; Pétrélis et al. 2003; Marié et al. 2003), Maryland (Peffley et al. 2000; Sweet et al. 2001), and Madison (Bayliss et al. 2006; O’Connell et al. 2005). They all predict exponential dynamo gain at a critical magnetic Reynolds number $Rm_{crit} \sim 50$. Yet the experiments give a null result, i.e., no exponential dynamo gain for experimental flows where $Rm_{exp} > 130 \simeq 2.5Rm_{crit}$ is achieved in the experiments. These null results are interpreted as being due to the negative effects of turbulent diffusion (Bourgoin et al. 2004; Spence et al. 2006; Nornberg et al. 2006; Laval et al. 2006). Our generalized interpretation of these results is that turbulence behaves as an enhanced diffusion of magnetic flux or an enhanced resistivity (Boldyrev & Cattaneo 2004; Ponty et al. 2005). In these experiments the turbulent velocity $v_{turb} \simeq 0.4\langle v \rangle$, where $\langle v \rangle$ is the average shear velocity (Nornberg et al. 2006). Then, the turbulence leads to a decreased conductivity, or an enhanced resistivity, as described by Krause & Rädler (1980):

$$\sigma_{turb} = \frac{\sigma_0}{1 + 4\pi\beta\sigma_0/c^2}, \quad (2)$$

where $\sigma_0 = c^2/(4\pi\eta_0)$ is the conductivity of the fluid, η_0 is the magnetic diffusivity of the same fluid, and σ_{turb} is the effective conductivity in the presence of turbulence. The constant β

is derived from mean field electrodynamics assuming isotropic turbulence:

$$\beta \simeq (\tau_{corr}/3)v_{turb}^2, \quad (3)$$

where τ_{corr} is the mean correlation time of a turbulent fluctuation. Since the correlation time is an eddy turnover time, then $\tau_{corr} = L_{corr}/v_{turb}$, where L_{corr} is an eddy size. We then identify $L_{corr}v_{turb}/3 = \beta$ as a turbulent diffusion coefficient, and the turbulent conductivity becomes the original conductivity decreased by the factor $1 + 4\pi\beta\sigma_0/c^2$. In the limit of a large $\beta \gg \eta_0$, the effective magnetic diffusivity then becomes just the turbulent diffusivity, $\eta_{eff} = \beta \simeq L_{corr}v_{turb}/3$. It is the combination of turbulent diffusivity with fluid resistivity or, equivalently, effective resistivity that determines dynamo gain. In unconstrained flows, L_{corr} becomes the dimension of the largest eddy that can “fit” in the flow, or $L_{corr} = [d(\ln\langle v \rangle)/dx]^{-1} \simeq L/2$, where L is the dimension of the shear flow. This larger effective resistivity then results in a smaller effective magnetic Reynolds number that determines dynamo exponential gain, $Rm_{eff} = L\langle v \rangle/\eta_{eff}$ for a given $\langle v \rangle$ and L . Since $v_{turb} \simeq \langle v \rangle/2$, then $\eta_{eff} \simeq (1/3)(1/4)\langle v \rangle L$ and $Rm_{eff} \simeq 12$. This value of Rm_{eff} is significantly smaller than the predicted value of $Rm_{crit} \sim 50$ for the Dudley-James or von Kármán flows used in the current major experiments. It is even smaller than $Rm_{crit} \approx 17$ for Ponomarenko flow used in Riga dynamo experiment (Ponomarenko 1973; Gailitis & Freiberg 1976).

The critical threshold for dynamo gain, Rm_{crit} , is determined from kinematic dynamo calculations without enhanced turbulent resistivity. For bounded sheared flows, namely, except for all but the special flows mentioned above, $Rm_{crit} \sim 100$. The question is whether there can be any exponential dynamo gain in any unconstrained shear flows.

By way of confirmation, in the two dynamo experiments that have demonstrated positive exponential dynamo gain, the Riga experiment (Gailitis et al. 2000, 2001) and the Karlsruhe experiment (Stieglitz & Müller 2001), turbulence was greatly constrained by the presence of a ridged wall(s) separating the counterflowing shear flows. It was therefore recognized that these experiments did not represent astrophysical dynamos, but, on the other hand, strongly confirmed dynamo theory. We were therefore convinced that a natural constraint of turbulence must exist for the dynamos of astrophysics.

There are at least five constraints on turbulence in shear flow that may alter the magnitude of turbulence, as well as its isotropy. We list five of these constraints, expecting others to be identified:

1. Viscosity.
2. A ridged wall.
3. A positive outward gradient of angular momentum.
4. A gradient of entropy in a gravitational field (e.g., the base of the convection zone of stars).
5. Delay in the onset of fully developed turbulence in unconstrained shear flow.

Viscosity (1) may inhibit all turbulence so that in this limit the properties of turbulence are not relevant. A ridged wall (2) affects the magnitude of turbulence and its isotropy (the law of the walls). The gradients of angular momentum (3) and entropy (4) apply to astrophysical circumstances, where depending on the presence of other instabilities, e.g., the magnetorotational instability or Rossby vortex instability, turbulence may be a small fraction of the average shear flow. Time dependence (5) is similar to viscosity in the case where the initiation time of the shear flow may be very short compared to the development time of the turbulence, as in the case of the plumes driven by star-disk collisions.

This limit leads to negligible levels of turbulence compared to the shear flow.

We choose a gradient of angular momentum and time dependence of the shear flow, e.g., plume flow, as the probable mechanisms of constraint of turbulence for the most likely circumstances for producing an astrophysical dynamo; we choose angular momentum as the circumstance for the accretion in massive black hole formation; and we choose time dependence for the constraint of the transient period of the rise and fall of plumes in astrophysical circumstances.

It is with this uncertainty as to the role of turbulence in dissipating the magnetic flux, as opposed to amplifying it, that the current work was undertaken. Hence, when we discovered the possibility of a combination of (a) a near-laminar shear flow, i.e., Keplerian flow, and (b) a repeated, transient, nonturbulent source of helicity the possibility of a robust astrophysical dynamo become evident. Although the star-disk collisions are random in time, the flow, to first order, is repeatable and therefore not turbulent. The flow resulting from a superposition of many plumes may be chaotic in time, but the superposition of many plumes, all with the same rotation, leads to a net rotated flux in the same direction. On the other hand, the vortices in anisotropic turbulence make an arbitrary number of turns, and so the instantaneous mean value of rotated flux is proportional to the square root of the number of vortices. Thus, we characterize the plumes as semicoherent rather than as a truly chaotic phenomena in which the entropy would be increased. In addition, we discuss next an analysis in which turbulence may augment or possibly limit the “fast dynamo.”

The dynamos with nonvanishing growth rate in the limit of very high conductivity are called “fast dynamos” (Vainshtein & Zeldovich 1972). A classic picture of the fast dynamo mechanism is the stretch-twist-fold process (Sakharov 1982; Vainshtein & Zeldovich 1972). There are strong indications that fast dynamo action is typical for chaotic flows (Lau & Finn 1993; Finn 1992; Finn et al. 1991). However, in the kinematic stage of the dynamo, a sharp exponential decrease in some spatial scales of the magnetic field occurs. The magnetic field becomes concentrated in the narrow sheets or narrow filaments until the frozen-in picture becomes invalid for any conductivity. In the kinematic limit, the thickness of these structures of strong magnetic field is estimated to be $\delta l \sim L \times \text{Rm}^{-1/2}$, where the magnetic Reynolds number $\text{Rm} = vL/\eta$, v is the velocity of the conducting fluid, L is the characteristic dimension of the fluid, and η is magnetic diffusivity due to finite resistivity. The growth of small-scale fields invalidates the kinematic approximation beginning with the resistive scale and up to the larger scales. The structure and the spectrum of this hydromagnetic, turbulent dynamo is expected to be different from the hydrodynamic turbulence because of the action of the magnetic forces. The size δl of the smallest magnetic structures depends on the details and properties of the hydromagnetic regime of the turbulence, which are still the subject of active debate in the literature (Iroshnikov 1963; Kraichnan 1965; Goldreich & Sridhar 1995; Boldyrev 2006), but it is always much smaller than the large-scale L by some positive power of Rm . In the limit of infinite conductivity, no flux can merge in an infinite time, and hence there can be no multiplication of flux at a scale of the system (large scale). Motions with nonzero helicity h at a large scale and the ability to reconnect are required to obtain the growth of the large-scale fields and magnetic flux comparable to the growth rate of the small-scale field. When the large-scale field growth is at a rate comparable to the growth rate of the small-scale field, the characteristic growth time is of the order of the diffusion time, $t_{\text{diff}} = L^2/\eta$.

Yet our ionized disk of thickness $H = 2.6 \times 10^{13}$ cm, velocity $v_K \approx 10^9$ cm s $^{-1}$, and resistivity $\eta \approx 10^7$ cm 2 s $^{-1}$ at 1 eV $\approx 10^4$ K temperature results in $\text{Rm} \approx 10^{15}$. This is a number so large as to preclude useful growth of the magnetic flux and large-scale fields in a Hubble time, which is much shorter than the diffusion time of the magnetic field $t_{\text{diff}} = H^2/\eta = 10^{20}$ s.

Only by invoking the phenomena of turbulent resistivity (above) can the existence of an accretion disk dynamo producing large-scale magnetic fields be made convincing. Turbulent resistivity within the disk is likely to be due to the same turbulence that creates the α -viscosity of the Shakura-Sunyaev disk or the Rossby vortices of the RVI disk. Within the disk, we expect turbulent diffusion of the magnetic flux to be the same as that of angular momentum, and thus proportional to the Shakura-Sunyaev parameter α_{SS} (see Paper I).

Reconnection may be occurring within the turbulence, leading to more rapid dissipation of the magnetic flux than the turbulent cascade alone. However, the force-free fields above (and below) the disk that are produced by the winding of the dynamo-produced large-scale fields need not be dissipated until they are projected large distances away from the disk.

Recognizing this lack of fundamental understanding, but noting that laboratory and astrophysical observations lead to the same order of magnitude for reconnection, we proceed with the assumption that a value of $\text{Rm} \approx 200$ approximates the magnetic diffusion within the disk. In what follows this parameter could be several orders of magnitude larger, but not much smaller, and still result in an effective accretion disk dynamo.

3.2. Estimates of the Dynamo Growth Rate: The Flux Rotation Dynamo

With these values of plume size, frequency, and magnetic diffusivity, as well as Keplerian flow, let us make some estimates of the threshold parameters and the growth rate of the α - ω dynamo, which has been outlined in a previous section. The approach developed below, in the rest of § 3, we call the flux rotation dynamo as opposed to the mean field dynamo. Later, we will compare these approaches, with emphasis on the difference between coherent motions and random averaged variables. We consider for now the linear growth, i.e., when the magnetic field is not strong enough, such that we can neglect the back-reaction of the generated magnetic field on both the Keplerian flow and on the plume flow fields.

Suppose that at some moment of time we have an even-symmetry poloidal magnetic field, B_P (see Appendix A for definitions of even and odd symmetries). The radial component of this field within the disk defines a poloidal flux, F_P , such that at a given radius r , the poloidal flux through one-half of the disk, on either side of the midplane, is $F_P = B_r(\text{area}) = B_r H 2\pi r$, where H is the semithickness of the disk. This flux, within the conducting and differentially rotating Keplerian disk, will be wrapped up into a toroidal magnetic field within the disk, B_T . This toroidal field will be stronger than or a multiple of the initial poloidal field, depending on the number of turns and the resistive dissipation of the currents. Initially, we consider the field without dissipation, so that an initial flux line of poloidal magnetic field B_P will be differentially wrapped n times around the axis, leading to an enhanced B_T . Let us introduce the number of differential turns, n , that occur at a radial distance, r , during time, t , as

$$2\pi n = -t \times r \frac{d\Omega_K}{dr}, \quad (4)$$

where $\Omega_K = (GM/r^3)^{1/2}$ is the Keplerian angular velocity of the disk. We consider the toroidal flux, F_T , in the azimuthal direction

and within the half-thickness of the disk, H to be $F_T = rHB_T$. Then, the increment of this toroidal flux added to the original F_T per dr and per dn differential turns becomes

$$dF_T = dB_T \times H dr = rB_r dt \frac{d\Omega_K}{dr} H dr = -2\pi dn \times B_r H dr. \quad (5)$$

Since $dF_T = dB_T \times H dr$, this is equivalent to $dB_T = -2\pi dn \times B_r$.

If we integrate over dn and over dr to give the change in toroidal flux, ΔF_T , per revolution, we obtain an estimate

$$\Delta F_T \approx -2\pi r n H B_r = -n F_P. \quad (6)$$

The poloidal flux, F_P , in turn is derived from the toroidal flux by the helicity, h , of the plumes driven by star-disk collisions. Each plume lifts a loop of toroidal flux with cross section $dA = HR_{\text{shk}} \simeq H^2$ (Fig. 1), where R_{shk} is the radius of the shock produced by a star (see Paper I for details). The small distortion $\sim(1 + H/r)$ from the circular cross section is neglected. When this unit of area or flux is rotated $\pi/2$ radians in the poloidal direction with the efficiency of a single plume, α_{pl} , it creates an equal unit of poloidal flux $dF_{P,\text{pl}} = -\alpha_{\text{pl}} B_T H^2$ inside the disk. The top parts of the field loops created by the plumes are rising quickly because of the low density of plasma in the corona; even a very weak magnetic field can overcome the gravity acting on a rarefied gas, and the expansion will be at a relativistic Alfvén speed $v_A \lesssim c$. Also, the shearing of the top part of the loops is small, so the toroidal field produced is also small. The rate of this removal of the toroidal and poloidal fields from above the disk to the magnetized jet is higher than the diffusion feeding from the inside of the disk, if $\eta/H \ll c$. We know that $\Omega_K H^2/\eta \sim 1$. Therefore, $\eta/H \sim \Omega_K H$, and, indeed, we have $\Omega_K H \ll c$. In this approximation, only the evolution of F_P and F_T inside the disk defines the dynamo, and it is separate from the evolution of the magnetic fields in the corona of the disk. Each such unit of flux $dF_{P,\text{pl}}$ is only $2H$ in length, and in order to create or to affect a flux tube of length r (poloidal) or $2\pi r$ (toroidal) requires an aligned sum of increments $r/2H$ in number in the poloidal direction and $2\pi r/2H$ in number in the toroidal direction. (Each plume also creates an increment, a pair of equal and opposite vertical fluxes, $dF_Z \simeq \pm dF_{P,\text{pl}}$, which exponentially decrease to near zero regardless of overlapping plumes.)

3.3. Plume Coverage

The fractional area of one side of the disk inside radius r covered by plumes at any one time, $\bar{q}_{<r}$, can be estimated as $\bar{q}_{<r} \approx N(<r)H^2/r^2$ because each of total $N(<r)$ stars (eq. [2] in Paper I) with impact radii inside a given radius r crosses the disk two times in approximately one Keplerian period $T_K(r) = 2\pi/\Omega_K(r)$. Each such crossing produces one plume of radius $\approx H$ on each side of the disk.

Each plume exists for time $T_K/2$ before falling back to the disk surface. Then, in the spirit of a flux rotation explanation of the dynamo, we evaluate the fractional contribution to the total poloidal flux by each rotated plume. The plumes occur randomly over the area of the disk, but their contribution to the average flux, either poloidal or toroidal, is independent of their position on the surface, because the coherence of the plume rotation ensures an effect proportional to the algebraic sum of the number of plumes, regardless of their location. Therefore, we can rearrange, *gedanken*-wise, the location of the plumes over the disk without affecting the result. We therefore rearrange and align a fraction of the plumes, $r/2H$ in number, to create a single, continuous tube

of poloidal flux, $B_{\text{pl}}H^2$, and length r , where $B_{\text{pl}} = \alpha_{\text{pl}}B_T$. We have enough plumes, $N(<r)$, to create $N_{\text{tube}} = N(<r)/(r/2H)$ such flux tubes. These poloidal flux tubes of width $2H$ then collectively cover a fraction in azimuth or a sector of angular width of

$$\Delta\phi = \frac{2HN_{\text{tube}}}{2\pi r} = \frac{2H^2}{\pi r^2} N(<r) \quad (7)$$

and produce a poloidal flux per half-revolution of

$$\Delta F_P = N_{\text{tube}} H^2 B_{\text{pl}} = -N_{\text{tube}} H^2 \alpha_{\text{pl}} B_T. \quad (8)$$

We can express N_{tube} from equation (7) as

$$N_{\text{tube}} = \frac{\pi r}{H} \Delta\phi. \quad (9)$$

We then note that $\Delta\phi = \bar{q}_{<r}$, by construction, and therefore the poloidal flux created by $N(<r)$ plumes per half-revolution becomes

$$\begin{aligned} \Delta F_P &= -\bar{q}_{<r} \frac{\pi r}{H} H^2 \alpha_{\text{pl}} B_T \\ &= -\pi r H \bar{q}_{<r} \alpha_{\text{pl}} B_T = -\bar{q}_{<r} \alpha_{\text{pl}} \pi F_T. \end{aligned} \quad (10)$$

We define a parameter α_m as $\alpha_m = \bar{q}_{<r} \alpha_{\text{pl}}$ to give $\Delta F_P = -2\pi \alpha_m F_T$ per revolution. Here α_m becomes an efficiency for the rotation of toroidal flux into poloidal flux per radian of revolution averaged over all the plumes.

Then the time derivative considering two plumes per Keplerian period becomes

$$\frac{dF_P}{dt} = -\Omega_K \alpha_m F_T. \quad (11)$$

Similarly, from equation (6) we obtain

$$\frac{dF_T}{dt} = -\frac{\Omega_K}{2\pi} \frac{3}{2} F_P, \quad (12)$$

because one Keplerian revolution, $T_K = 2\pi/\Omega_K$, corresponds to $n = 3/2$ differential turns, according to expression (4).

In addition, we must consider the fractional flux cancellation of each of these two flux transformations. This leads to partial cancellation of each orthogonal component by the other, and to partial self-cancellation as well. Finally, second-order effects, as well as the different dissipation rates of the two fluxes, must be considered. These effects are usually averaged in mean field theory, but here we consider them separately because we are concerned with a semicoherent flow as opposed to a turbulent dynamo.

3.4. Toroidal Multiplication with Losses

We considered above that the flux is frozen within the disk fluid flow. Now we consider the relaxation of this condition by resistive diffusion or reconnection.

Resistive dissipation of the currents supporting these fields limits the growth of toroidal field. Here, we consider the saturation of the toroidal multiplication alone with a fixed poloidal field. After many turns, this additional toroidal magnetic field reaches a saturation value determined by the balance of the multiplication rate with resistive diffusion. The toroidal magnetic field changes

fastest in the vertical direction on the scale H ; therefore, the dissipation rate is estimated to be

$$\frac{dF_T}{dt} \approx -\frac{\eta}{H^2} F_T = -\frac{F_T}{\text{Rm}_\Omega} \Omega_K \frac{r^2}{H^2}, \quad (13)$$

where magnetic Reynolds number with respect to Keplerian rotation is defined as

$$\text{Rm}_\Omega = \frac{\Omega_K r^2}{\eta}. \quad (14)$$

If we add this loss to the gain of equation (12), we then have

$$\frac{dF_T}{dt} = \left(-\frac{3}{4\pi} F_P - \frac{F_T}{\text{Rm}_\Omega} \frac{r^2}{H^2} \right) \Omega_K. \quad (15)$$

Thus, the toroidal field saturates after $\text{Rm}_\Omega H^2/r^2$ turns. In view of equation (15), the limiting, steady state is achieved when

$$\frac{F_T}{F_P} = -\frac{3}{4\pi} \text{Rm}_\Omega \frac{H^2}{r^2}.$$

This limiting value of the ratio F_T/F_P can be measured separately in the laboratory (in $H \approx r$ geometry), without the motions producing the α -effect of the complete dynamo, by applying an external, fixed poloidal initial field. The same situation may apply to the galaxy if a small residual poloidal flux is left over from the initial AGN phase, i.e., this dynamo, and therefore no further dynamo in the galactic disk would be required, even though one likely exists (Ruzmaikin et al. 1988; Ferrière & Schmitt 2000; Kulsrud 1999). Furthermore, this ratio represents the maximum possible toroidal multiplication that should offset losses in the rotation of toroidal flux back into poloidal flux to achieve a net positive dynamo growth rate. Thus, if the toroidal amplification is large, the efficiency of rotation of toroidal flux back into poloidal flux, α_m , can be small, and the dynamo will still be growing.

To this toroidal multiplication and resistive loss we must add the back-reaction effects of the helicity or flux rotation mechanism(s) of the “ α_m -effect.”

3.5. Production of Poloidal Flux and Losses

In order to calculate α_m of equation (11), we require both $\bar{q}_{<r}$ and α_{pl} . The coverage factor, $\bar{q}_{<r}$, is straightforward to estimate from the star-disk collision rate and plume size, but the efficiency of the helical deformation by a single plume (eq. [1]) is more problematic. The simplest and ideal concept of poloidal flux production by a plume is that a plume of radius $\approx H/2$ rises a distance $\approx 2H$ above the disk with trapped flux, $dF_{T,\text{pl}} = B_T H^2$, rotates this flux exactly $\pi/2$ radians, i.e., into the poloidal direction, falls back, merges with the disk matter; and releases this now-poloidal flux by diffusion or reconnection so that this unit of poloidal flux adds in the same direction, i.e., coherently, to F_P . Of course this sequence of rotation, rise, fall, and merging of the fluxes will happen episodically and only when averaged, leading to the factor α_m such that $\Delta F_P = -2\pi\alpha_m F_T$ per revolution (eq. [11]). The associated experimental paper (Beckley et al. 2003) on laboratory measurements of plume rotation implies that a rising and expanding plume, in a rotating frame, indeed rotates a finite angle $\sim \pi/2$ radians before merging with the background fluid. In this case the finite angle of rotation occurs for the same reason as that expected in the accretion disk. In the laboratory case the velocity of the plume relative to the velocity of rotation is chosen such that the plume is destroyed or broken up by striking

the end wall of the apparatus in a chosen finite fraction of a period of rotation. In an accretion disk, as pointed out earlier, the plume indeed rises and falls in π radians with the rotation angle, and also merges with background disk material, both increasing monotonically during this rise and fall time. Hence the ideal angle, $\pi/2$ radians, occurs as a result of the product and average of the three progressive deformations, but most importantly, throughout the entire sequence the incremental addition to α_m is always positive. Also we should note that with each plume there is an upward vertical flux, $+dF_Z$, equal to a downward vertical flux, $-dF_Z$, which presumably averages to zero with flux merging.

As described in equations (10) and (11), the number of plumes adding to the poloidal flux is described by the filling factor, $\bar{q}_{<r}$, of the disk by plumes, where $\bar{q}_{<r} = N(<r)H^2/r^2$. The average number of plumes on one side of the disk within a radius r at any given time is approximately equal to the number of stars with impact radii inside r , $N(<r)$, given by expression (2) in Paper I.

H is given by expression (6) in Paper I, valid for the inner zone (a) of a standard or Shakura-Sunyaev disk. The reader is referred to Paper I for the details, arguments, and caveats of using this model of an accretion disk originally proposed by Shakura (1972) and further developed in Shakura & Sunyaev (1973). Here we only remark that we use the expressions for the disk parameters valid for $r < r_{ab}$, where r_{ab} is the transition radius between zones (a) (radiation dominated) and (b) (particle pressure dominated), generally a few hundreds of r_g . As we see from expression (25) below, the dynamo growth rate is maximal at about r_{ab} . To obtain the number density of stars $n(r)$ in the vicinity of CMBH, we use analytic and numerical models of the stellar dynamics to extrapolate from the observed n at the distance of ≈ 1 pc from CMBH down to few tens of r_g . Observations typically suggest number densities of the order of 10^5 pc^{-3} at a distance 1 pc. So we write $n(1 \text{ pc}) = 10^5 n_5 \text{ pc}^{-3}$. The most notable feature of this distribution of stars is the sharp decrease of their density for r less than about $10r_t$, where $r_t = 2.1 \times 10^{-4} \text{ pc } M_8^{1/3} = 21r_g M_8^{-2/3}$ and is the tidal disruption radius for a solar mass star by the tidal forces near the CMBH with mass $M = 10^8 M_8 M_\odot$. This decrease is the effect of physical collisions of stars with each other, tidal disruptions by CMBH, and multiple passages of the stars through the accretion disk, which grind their orbits into the disk plane and reduce the number of remaining stars not trapped by the accretion disk (see Paper I for more details).

Using the approximate analytical model (eq. [2]) from Paper I, we have, for $r < 10^{-2} \text{ pc}$

$$\bar{q}_{<r} = \begin{cases} 1.9 \times 10^{-4} n_5 \left(\frac{l_E}{0.1} \right)^2 \\ \times \left(\frac{\epsilon}{0.1} \right)^{-2} \left[\frac{r}{10r_t} - \left(\frac{r}{10r_t} \right)^{-2} \right], & 10r_t < r < 10^{-2} \text{ pc}, \\ 0, & r < 10r_t \text{ (no star-disk collisions)}, \end{cases} \quad (16)$$

where the factor $1 - (3r_g/r)^{1/2}$ from the Shakura-Sunyaev model is omitted since $r \gg r_g$. Also, $l_E = L/L_{\text{Edd}}$ is the ratio of the total luminosity of the disk L to the Eddington limit L_{Edd} for the CMBH of mass M and ϵ is the fraction of the rest-mass energy of the accreted matter, $\dot{M}c^2$, that is radiated away by the disk, $L = \epsilon \dot{M}c^2$. The number given by expression (16) is not large, so the probability that any given plume overlaps with another is small,

and therefore, on the average, each plume will be an individual, isolated event.

With $\bar{q}_{<r}$ given by expression (16), the corresponding $\alpha_m = \bar{q}_{<r}\alpha_{\text{pl}}$ becomes

$$\alpha_m = \begin{cases} 1.9 \times 10^{-4} n_5 \alpha_{\text{pl}} \left(\frac{l_E}{0.1}\right)^2 \left(\frac{\epsilon}{0.1}\right)^{-2} \\ \times \left[\frac{r}{10r_t} - \left(\frac{r}{10r_t}\right)^{-2} \right], & 10r_t < r < 10^{-2} \text{ pc}, \\ 0, & r < 10r_t \text{ (no star-disk collisions)}. \end{cases} \quad (17)$$

The system of linear differential equations (11) and (12) has a growing solution

$$F_T = F_{T,0} e^{\Gamma t}, \quad (18)$$

where

$$\Gamma = \Omega_K \sqrt{\frac{3\alpha_m}{4\pi}} = \Omega_K \sqrt{\frac{3\bar{q}_{<r}\alpha_{\text{pl}}}{4\pi}}. \quad (19)$$

Similar to the toroidal field, the gradient of the poloidal magnetic field is greatest in the vertical direction on the scale H , and therefore the dissipation rate of the poloidal flux is estimated in a way analogous to the dissipation rate of the toroidal flux (eq. [13]),

$$\frac{dF_P}{dt} \approx -\frac{\eta}{H^2} F_P = -\frac{F_P}{\text{Rm}_\alpha} \frac{l^2}{H^2} \Omega_K, \quad (20)$$

where magnetic Reynolds number with respect to the α -deformation is defined as

$$\text{Rm}_\alpha = \frac{\Omega_K l^2}{\eta}, \quad (21)$$

and $l \approx 3H$ is the height above the disk midplane reached by the plume before falling back to the disk. In our approximation $\text{Rm}_\alpha \approx \text{Rm}_\Omega l^2/r^2$, but we keep Rm_α and Rm_Ω separate to evaluate the effects of Keplerian and plume motions separately. Adding the resistive dissipation, equation (20), to the poloidal gain, equation (11), results in

$$\frac{dF_P}{dt} = -\Omega_K \alpha_m F_T - \frac{l^2}{H^2} \frac{\Omega_K}{\text{Rm}_\alpha} F_P. \quad (22)$$

The system of linear differential equations (15) and (22) has a growing solution of the form given by equation (18), but with the growth rate modified as

$$\Gamma = \frac{\Omega_K}{2} \left\{ \left[\left(\frac{r^2}{H^2 \text{Rm}_\Omega} - \frac{l^2}{H^2 \text{Rm}_\alpha} \right)^2 + \frac{3\alpha_m}{\pi} \right]^{1/2} - \left(\frac{r^2}{H^2 \text{Rm}_\Omega} + \frac{l^2}{H^2 \text{Rm}_\alpha} \right) \right\}. \quad (23)$$

We note that in the limit of small resistivity, i.e., large magnetic Reynolds numbers, we recover the growth rate of equation (19); otherwise, we note the surprising circumstance that the difference in the resistive terms adds to the growth rate, whereas the

sum decreases the growth rate, as we expect for a purely diffusive resistivity. For positive growth rate, the first term, of course, must be greater than the second. In the purely diffusive limit, if we use $\text{Rm}_\alpha = \text{Rm}_\Omega l^2/r^2$, expression (23) simplifies to

$$\Gamma = \Omega_K \sqrt{\frac{3\alpha_m}{4\pi}} - \frac{\eta}{H^2} = \Omega_K \left(\sqrt{\frac{3\alpha_m}{4\pi}} - \frac{l^2}{H^2 \text{Rm}_\alpha} \right). \quad (24)$$

To the extent that the resistive terms are small, and therefore Rm is large and the compensating effect of the requirement for merging of newly minted poloidal flux with old poloidal flux is neglected, then the dynamo growth rate is large, of order $\Omega_K \alpha_m^{1/2}$. However, there is no reason to expect that the resistivity is purely diffusive, and we expect that tearing-mode reconnection drives the merging of flux at some near-constant and large $\text{Rm}_\alpha \simeq \text{Rm}_\Omega \simeq 200$ (Sovinec et al. 2001).

Then from equations (17) and (19), the maximum dynamo growth rate occurs between r_{ab} and $10r_t$ and becomes (for a $10^8 M_\odot$ CMBH)

$$\begin{aligned} \Gamma &\approx 7 \times 10^{-3} \Omega_{Kt} n_5^{1/2} \alpha_{\text{pl}}^{1/2} \\ &\times \left(\frac{l_E}{0.1} \right) \left(\frac{\epsilon}{0.1} \right)^{-1} \left(\frac{r}{10r_t} \right)^{-1} \left[1 - \left(\frac{r}{10r_t} \right)^{-3} \right]^{1/2} \\ &\text{for } r > 10r_t, \\ \Gamma &= 0 \text{ for } r < 10r_t, \end{aligned} \quad (25)$$

where $\Omega_{Kt} = 2.08 \times 10^{-7} \text{ s}^{-1}$ is the Keplerian rotation velocity at $10r_t$ for a $10^8 M_\odot$ black hole. The exponential rate of multiplication, in view of equation (25), maximizes at $r = 13.6r_t$, where

$$\Gamma_{\text{max}} \approx \begin{cases} 1.4 \times 10^{-9} \text{ s}^{-1} n_5^{1/2} \alpha_{\text{pl}}^{1/2} \left(\frac{l_E}{0.1} \right) \left(\frac{\epsilon}{0.1} \right)^{-1} & \text{at } 13.6r_t, \\ 4 \times 10^{-2} \text{ yr}^{-1} n_5^{1/2} \alpha_{\text{pl}}^{1/2} \left(\frac{l_E}{0.1} \right) \left(\frac{\epsilon}{0.1} \right)^{-1} & \text{at } 13.6r_t. \end{cases} \quad (26)$$

Since the density of stars does not actually drop sharply to 0 at $r = 10r_t$, as in our approximate analytical model, the estimate of Γ_{max} above is approximate, and the actual maximum of the growth rate is achieved at r somewhat smaller than $13.6r_t$.

We can find the ratio of toroidal to poloidal flux in the growing dynamo mode by substituting expression (23) for Γ into equation (15):

$$\begin{aligned} \frac{F_T}{F_P} &= -\frac{3}{2\pi} \left[\left(\frac{r^2}{H^2 \text{Rm}_\Omega} - \frac{l^2}{H^2 \text{Rm}_\alpha} \right) \right. \\ &\quad \left. + \sqrt{\frac{3\alpha_m}{\pi} + \left(\frac{r^2}{H^2 \text{Rm}_\Omega} - \frac{l^2}{H^2 \text{Rm}_\alpha} \right)^2} \right]^{-1}. \end{aligned} \quad (27)$$

In the purely diffusive limit, when $\text{Rm}_\alpha = \text{Rm}_\Omega l^2/r^2$, this ratio simplifies to

$$\frac{F_T}{F_P} = \frac{B_T}{2\pi B_P} = -\frac{1}{2} \sqrt{\frac{3}{\pi \alpha_m}}. \quad (28)$$

As in any α - ω dynamo, the averaged toroidal magnetic flux is much larger than the averaged poloidal magnetic flux (recall that $\alpha_m \ll 1$).

Regardless of how small α_{pl} is (we believe it is $\simeq 1$), the dynamo gain is so large within the time of formation of the CMBH, 10^8 yr, that saturation will occur early in the history of the disk dynamo, regardless of how small the initial seed field is. The origin of such a seed field (e.g., a star, the Biermann battery from decoupling, or primordial fields) becomes moot. Nevertheless, for completeness, we explore how this gain can be reduced by flux rotated by the plume process such that it opposes rather than augments either the mean toroidal or poloidal fluxes in the above estimates of dynamo gain.

3.6. Flux Compensation by Plumes

So far we have considered only the positive increment of poloidal flux to the dynamo gain by plume rotation of the toroidal flux. This same rotation will rotate the coexisting poloidal flux into opposition with the primary toroidal flux. In addition to the extent that the plumes or any other cyclonic motion continues the rotation beyond π radians, a further reduction in dynamo gain occurs because of the averaging of this opposed flux. First we note that $B_P/B_T = -(\alpha_m/3\pi)^{1/2} \ll 1$ according to expression (28).

The deformation leading to the rotation of an increment of toroidal flux into an increment of poloidal flux by the rotation of the plumes leads to a similar fraction of poloidal flux being rotated so as to oppose the toroidal flux. However, since only a small fraction is rotated by plumes, as opposed to that rotated by the shear of rotation, the negative effect on the toroidal flux is small, $\simeq \alpha_m$. Similarly, a rotation by π radians causes a decrement of both the toroidal and poloidal fluxes to oppose themselves, so that the fraction of flux rotated π radians must be small for high gain. The fraction of flux rotated $3\pi/2$ radians must be even smaller for high gain, because a rotation of $3\pi/2$ radians causes the larger toroidal flux to oppose the much smaller poloidal flux, even though a small positive effect can occur when the same rotation causes the smaller poloidal flux to add to the toroidal. This assumes that the plumes are circular in cross section, so that the cross-sectional areas for the radial and toroidal fluxes are the same. The distortion of the plume cross section by differential rotation in $\pi/2$ radians of rotation is similarly small, $\Delta\phi \simeq (1/4)(H/r)$.

We designate these fractions τ_1 , τ_2 , and τ_3 for the fraction of flux rotated $\pi/2$, $2\pi/2$, and $3\pi/2$ radians. In general we consider $\tau_1 \sim \tau_2 \gg \tau_3$; otherwise we do not expect positive gain. One can think of these coefficients as correlation coefficients of the decaying plume rotation; a plume undergoes little rotation beyond π radians, when it falls back to the disk. All plumes are considered to behave in the same way, so that these coefficients remain constant and therefore do not describe turbulence. These partial flux cancellations all reduce the dynamo gain. Equations (15) and (22) are then extended to become

$$\begin{aligned} \frac{dF_T}{dt} &= \Omega_K \left(-\frac{3}{4\pi} F_P - \frac{F_T}{\text{Rm}_\Omega} \frac{r^2}{H^2} - \alpha_m \tau_1 F_P \right. \\ &\quad \left. - \alpha_m \tau_2 F_T + \alpha_m \tau_3 F_P \right), \\ \frac{dF_P}{dt} &= \Omega_K \left(-\alpha_m \tau_1 F_T - \frac{F_P}{\text{Rm}_\alpha} \frac{l^2}{H^2} - \alpha_m \tau_2 F_P + \alpha_m \tau_3 F_T \right). \end{aligned} \quad (29)$$

Here we have introduced $\alpha_m \tau_1$ in the first term of the F_P equation, where tacitly we had assumed $\tau_1 = 1$ before. Terms with τ_3 in both parts of equation (29) are small compared to the terms with τ_1 , because $\tau_1 \gg \tau_3$. Solving system (29) for exponentially

growing solutions, we find a generalization of expression (23) for the growth rate Γ :

$$\begin{aligned} \Gamma &= \frac{\Omega_K}{2} \left(\left\{ \left(\frac{r^2}{H^2 \text{Rm}_\Omega} - \frac{l^2}{H^2 \text{Rm}_\alpha} \right)^2 \right. \right. \\ &\quad \left. \left. + \alpha_m (\tau_1 - \tau_3) \left[\frac{3}{\pi} + 4\alpha_m (\tau_1 - \tau_3) \right] \right\}^{1/2} \right. \\ &\quad \left. - \left(\frac{r^2}{H^2 \text{Rm}_\Omega} + \frac{l^2}{H^2 \text{Rm}_\alpha} + 2\alpha_m \tau_2 \right) \right). \end{aligned} \quad (30)$$

One can see that the effects of considering finite τ_2 and τ_3 act to reduce the growth rate of the dynamo from the one given by expression (23). Specifically, if $\tau_3 > \tau_1$ (recall that $\alpha_m \ll 1$), then the second term in the sum under the square root in equation (30) becomes negative, and Γ cannot have a positive real part. This means that the dynamo is impossible for $\tau_3 > \tau_1$. In fact, τ_3 enters only in combination $(\tau_1 - \tau_3)$ and effectively reduces the value of τ_1 . This implies that the plume must terminate its contribution to flux rotation by π radians, but this is expected on general grounds because by this time the plume matter will have fallen back to and be merged with the disk.

The effect of finite τ_2 on the growth rate of the dynamo is much weaker than the effect of finite τ_3 . The leading positive contribution to Γ comes from the second term in the sum under the square root and is $\propto (\alpha_m \tau_1)^{1/2}$. The negative contribution of τ_2 is the $-2\alpha_m \tau_2$ term. Since $\alpha_m \ll 1$, we see that this negative contribution will be always small compared to the positive contribution for any $\tau_2 \sim \tau_1 \sim 1$. Thus, with τ_3 assumed small, we expect to recover the very large growth rate, $\Gamma \simeq 0.04$ per revolution, of expression (26).

4. MEAN FIELD THEORY FOR THE STAR-DISK COLLISION DRIVEN DYNAMO

The mean field approach to the problem of generation of the large-scale magnetic fields by the motions of the fluid with a random component was developed in Steenbeck et al. (1966) and later was widely used for all possible astrophysical and geophysical applications (Moffatt 1978; Krause & Rädler 1980; Ruzmaikin et al. 1988; Kulsrud 1999). The basic idea of the mean field approach is to average the equations for the evolution of the magnetic field over the small-scale motions of the conducting liquid. Such small-scale motions can be either a collection of waves with random phases, turbulent pulsations, randomly occurring jets, or plumes with the sizes considerably smaller than the scale of the whole system. Formal application of the mean field theory to the star-disk collision dynamo provides one more justification that such a dynamo is operational.

The number of plumes produced by star-disk collisions is large. At any given moment of time there exist $\sim 10^4$ plumes inside $r \sim 10^{-2}$ pc (see Paper I). The radius of each plume is $r_{\text{pl}} \simeq H \simeq 3.7 \times 10^{-3} r$ at $r \leq r_{\text{ab}}$, as shown in § 4.2 and equation (8) of Paper I. Therefore, the distance between neighboring plumes is $\sim 10^{-2} r$, and the radial and azimuthal sizes of the plumes cannot exceed $\sim 10^{-2} r$ without them overlapping. This condition is well satisfied with $\bar{q}_{<r}$ given by expression (16). The magnetic field on the scale of the order of r will be the average over many individual plumes. The occurrences of plumes are statistically independent, but each plume can be considered to be nearly identical to any other because the star velocities at any given radius are about the same. However, to the extent that the star sizes vary, the energy input to each plume will vary accordingly, and therefore

the size of plumes could be considered as a random noise process, but the spectral range is limited. It is attractive to apply mean field theory for the generation of the large-scale magnetic field by plumes. The averaging over patches of the disk surface exceeding the size of individual plumes is well justified. The averaging over the vertical direction is more problematic, since the sign of helicity produced by plumes exactly reverses above and below the disk midplane. In addition, the typical size of a plume is of the same order as the vertical scale of the change of helicity. Still, we explore the results of the application of mean field theory equations for the excitation of the global large-scale field and attempt to identify the departure points of mean field theory from the more coherent flux rotation analysis in this section.

The random motions induced by the star-disk collisions are clearly statistically anisotropic due to the existence of a preferred direction perpendicular to the disk plane, as well as a preferred direction of rotation on either side of the disk. Using isotropic expressions for the equations of the mean field theory provides so many simplifications that for our purpose of obtaining a proof of principle estimate, as well as a comparison to flux rotation theory, we use isotropic equations of the mean field theory. The mean electromotive force is given by

$$\overline{\mathbf{v}' \times \mathbf{B}'} = \alpha \bar{\mathbf{B}} - \beta \nabla \times \bar{\mathbf{B}}, \quad (31)$$

where \mathbf{v}' are velocities of small-scale motions, \mathbf{B}' is a small-scale field, and the bar denotes averaging over small scales (the distances between individual plumes and sizes of the plumes in our case). The expressions for the coefficients α and β are

$$\alpha = -\frac{\tau}{3} \langle \mathbf{v}' \cdot (\nabla \times \mathbf{v}') \rangle, \quad (32)$$

$$\beta = \frac{\tau}{3} \langle \mathbf{v}'^2 \rangle, \quad (33)$$

where τ is the time of the decorrelation of the Lagrangian velocities, i.e., the time of the “memory” of a fluid particle about the past history of its velocity. The angle brackets denote averaging over the statistical ensemble and in practice can usually be replaced by average over a volume larger than the typical scale of the random flow, \mathbf{v}' , but smaller than the scale of the change of the statistical properties of \mathbf{v}' and smaller than any large scale of the variability of the mean flow and mean magnetic field.

If the mean large-scale flow and large-scale magnetic fields are axisymmetric, then we need to solve the following system of equations for the evolution of mean axisymmetric magnetic field in cylindrical coordinates r, ϕ , and z (corresponding unit vectors are $\mathbf{e}_r, \mathbf{e}_\phi$, and \mathbf{e}_z ; Roberts & Soward 1992)

$$\begin{aligned} \frac{\partial A}{\partial t} + \frac{1}{r} \mathbf{v}_P \cdot \nabla(rA) &= (\beta + \eta) \left(\nabla^2 A - \frac{1}{r^2} A \right) + \alpha B_\phi, \quad (34) \\ \frac{\partial B_\phi}{\partial t} + r \mathbf{v}_P \cdot \nabla \left(\frac{1}{r} B_\phi \right) &= r \mathbf{B}_P \cdot \nabla \Omega + (\beta + \eta) \left(\nabla^2 B_\phi - \frac{1}{r^2} B_\phi \right) \\ &\quad - \alpha \left(\nabla^2 A - \frac{1}{r^2} A \right) - \frac{1}{r} \nabla \alpha \cdot \nabla(rA), \quad (35) \end{aligned}$$

where A is related to the poloidal magnetic flux F_P as $F_P = 2\pi rA$, B_ϕ is the toroidal magnetic field, \mathbf{B}_P is the poloidal magnetic field, \mathbf{v}_P is the poloidal velocity field, and $\Omega = \Omega(r, z)$ is the angular velocity of differential rotation. The quantity A is also a ϕ -component of a vector potential of the mean magnetic field

and $\mathbf{B}_P = \nabla \times (A \mathbf{e}_\phi)$, where \mathbf{e}_ϕ is a unit vector in the toroidal direction.

Averaging over the statistical ensemble within the angle brackets in equations (32) and (33) is replaced by averaging over many neighboring plumes. The correlation time τ is approximately half of the Keplerian period, $\tau = T_K/2$.

In fact, α and β are tensors because of the statistical anisotropy of the plumes. The generalization of expression (31) for the mean electromotive force, including effects of anisotropy, is (e.g., Moffatt 1978) $\mathbf{v}' \times \mathbf{B}'_i = \alpha_{ik} \bar{B}_k - \beta_{ijk} \partial \bar{B}_j / \partial x_k$, where there is a summation over repeated indices. In the limit of the α - ω dynamo, when $\text{Rm}_\alpha \ll \text{Rm}_\Omega$, the most important term in the expression for the mean electromotive force is $\alpha_{\phi\phi} \bar{B}_\phi$. This term describes the conversion of the toroidal to poloidal magnetic flux using the language of the mean field theory. It is analogous to the term on the right-hand side of equation (11) describing the production of the poloidal flux in the language of the flux rotation dynamo. It is this term that determines the growth rate of the α - ω dynamo. The generation of the mean field in an anisotropic random medium is possible when the mean kinetic helicity, $\langle \mathbf{v}' \cdot (\nabla \times \mathbf{v}') \rangle$, is equal to zero, but the components of the tensor, $\langle v'_i (\nabla \times \mathbf{v}')_k \rangle$, are nonvanishing (Krause & Rädler 1980; Molchanov et al. 1983). Ferrière (1993a, 1993b, 1998) performed detailed calculations of the α and β tensors resulting from the plume-like motions of gas in the differentially rotating Galactic disk caused by randomly placed supernovae explosions. These motions have some limited similarity to the plumes considered in the present work in that they also result in the conversion of toroidal to poloidal magnetic flux and are anisotropic, due to the vertical density gradient in the Galaxy. Subsequently, these results were used by Ferrière & Schmitt (2000) to calculate kinematic anisotropic α - ω dynamos. In the present work, α - and β -effects are assumed to be isotropic.

We now estimate the magnitude of the coefficients α and β in equation (35). The half-thickness of the slab with the helicity produced by plumes is about the same as the vertical extent of a plume, l . We assume the dependence of α on z as $\alpha = \alpha_0 z/l$, where α_0 is a characteristic value of helicity, which can vary with the radius r . This assumption for α satisfies symmetry requirement that $\alpha(-z) = -\alpha(z)$, but exact knowledge of the dependence of α on z is beyond our accuracy. We assume that $l > H$ and that $\alpha = \alpha_0 z/l$ in the whole region $-l < z < l$, i.e., we neglect the fact that helicity is almost zero inside the disk for $-H < z < H$. We also assume the turbulent magnetic diffusivity, β , to be uniform over $-l < z < l$. The fact that the maximum height of the plume is l means that the characteristic vertical velocity of the plasma in the plume is $v'_z \approx v_K l/r$. We assume that the characteristic velocity of the sideways expansion of the plume is $v'_s \approx v'_z/2$. Then, by time $T_K/2$, the plume expands to $\approx l/2$ in the horizontal dimension (we neglect the fact that the shape of the plume becomes elliptical). We estimate $\nabla \times \mathbf{v}' \approx -2\Omega_K \mathbf{e}_z$, and therefore $\mathbf{v}' \cdot (\nabla \times \mathbf{v}') \approx -2v'_s \Omega_K = -2l\Omega_K^2$. Similarly, $\mathbf{v}'^2 = 2v_s'^2 + v_z'^2 \approx (3/2)v_K^2(l^2/r^2)$ for the plume. Let us introduce the filling factor $q = q(r)$ equal to the fraction of the surface of the one side of the disk covered by plumes. Then averaging, denoted by angle brackets, is reduced to the multiplication of the values for one plume by q . From expression (32) and the above estimate of $\mathbf{v}' \cdot (\nabla \times \mathbf{v}')$, we have

$$\alpha_0 = \frac{2\pi}{3} l \Omega_K q, \quad (36)$$

and from expression (33) and the above estimate of \mathbf{v}'^2 , we have

$$\beta = \frac{\pi}{2} \Omega_K l^2 q. \quad (37)$$

Our estimate of β coincides with the estimate of the characteristic value of β for an ensemble of supernovae explosions occurring at the midplane of the Galaxy considered by Ferrière (1993b; their eq. [35]). The numerical coefficient in our estimate of β is slightly different from that of Ferrière (1993b).

The dynamo activity is present inside the thin layer with thickness $l \ll r$. This situation is the same as for the traditional model of the α - ω Galactic dynamo. We can use the extensive theory of the α - ω dynamo in thin disks developed in the connection with the Galactic dynamo. An extensive treatment of the α - ω Galactic dynamo can be found in Stix (1975), Zeldovich et al. (1983), and Ruzmaikin et al. (1988). We look for the solution of equations (34) and (35) in the α - ω limit when $\text{Rm}_\alpha \ll \text{Rm}_\Omega$. Since the thickness of the disk, $2H$, is small, we can neglect radial derivatives of the magnetic field compared to the z -derivatives. In this way the problem becomes local, with the eigenfrequency of the dynamo determined by solving the one-dimensional eigenvalue problem in the z -direction. This local approximation is similar to the local approximation used in Appendix A to derive the vertical structure of the accretion disk. We use results from Ruzmaikin et al. (1988) and replace their parameters with ours. The important parameter is the dynamo number,

$$D = r \frac{d\Omega_K}{dr} \frac{\alpha_0 l^3}{(\beta + \eta)^2} = - \frac{\pi \Omega_K^2 q l^4}{[\eta + (\pi/2) \Omega_K l^2 q]^2}, \quad (38)$$

where D is negative for anticyclonic vortices and $d\Omega_K/dr < 0$.

The density of particles in an equilibrated nonmagnetized disk falls off with z precipitously, $\propto \exp(-z^2/H^2)$ when the gas pressure dominates and even steeper when radiation pressure dominates (Shakura & Sunyaev 1973). This means that even a small magnetic field will have a significant influence on the dynamics of the disk corona. Thus, the kinematic dynamo approximation does not work in the disk corona. There, the force-free approximation $\nabla \times \mathbf{B} = \lambda \mathbf{B}$ describes the magnetic field evolution at $|z| > l$. In the particular case $\lambda = 0$, the force-free magnetic field satisfies the vacuum equation $\nabla \times \mathbf{B} = 0$. Reyes-Ruiz & Stepinski (1999) investigated the α - ω turbulent dynamo in accretion disks with linear force-free coronae. They match axisymmetric solutions of the dynamo equations (34) and (35) inside the disk to the solutions with constant λ of a force-free equation $\nabla \times \mathbf{B} = \lambda \mathbf{B}$ outside the disk. They find that the results for the dynamo eigenvalues and dynamo eigenmodes do not change significantly with the value of λ . The α -quenched saturated mode also depends weakly on λ . Thus, in order to obtain estimates for the star-disk collisions driven dynamo, we can assume that $\lambda = 0$ and that the magnetic fields obey the vacuum condition $\nabla \times \mathbf{B} = 0$ outside the disk. Note, however, that some of the poloidal magnetic field lines obtained in Reyes-Ruiz & Stepinski (1999) have inclination angles to the surface of the accretion disk less than 60° . This means that MHD outflow should start along these poloidal magnetic field lines (Blandford & Payne 1982). The presence of the MHD outflow would make the force-free approximation invalid. However, these field lines, although radial initially, after many turns become wrapped up into a force-free helix, where the radial magnetic field becomes smaller than either the external poloidal or toroidal fields. Both of these external fields, in turn, are smaller than the toroidal field inside the disk (Li et al. 2001b). Since the magnetic field inside the disk is much stronger than that outside the disk, the boundary condition at the top of the plume zone, $z = \pm l$, can be approximated as being on the boundary with the vacuum, $B_\phi = 0$ and $B_r = 0$.

The eigenvalue problem for the α - ω dynamo in the thin slab $-l(r) < z < l(r)$ with the vacuum outside the slab (Ruzmaikin

et al. 1988) can be reduced to solving a one-dimensional eigenvalue problem in the z -coordinate. In this way, the local growth rate of the dynamo $\Gamma(r)$ is obtained. The growth rate of the global mode Γ is very close to the maximum value of $\Gamma_m = \Gamma(r_m)$ over the disk radius. The corresponding eigenmode is localized in the ring of the disk near radius r_m . The characteristic radial width of the eigenmode for the dynamo numbers, which do not much exceed the threshold limit, is $\sim (lr_m)^{1/2}$ (Ruzmaikin et al. 1988). The most easily excited mode of the dynamo has quadrupole symmetry and is steady. The excitation condition of this most easily excited mode is $D < -\pi^4/16$ for the vertical dependence of the α -coefficient $\alpha = \alpha_0 z/l$ (Ruzmaikin et al. 1988). The excitation condition varies somewhat depending on the choice of the profile of the α -coefficient, but is of the same order as for the linear profile of α . The growth rate of the most easily excited steady state quadrupole mode not far from the excitation threshold is

$$\Gamma = \frac{\beta + \eta}{l^2} \left(-\frac{\pi^2}{4} + \sqrt{|D|} \right) = \frac{\pi}{2} \Omega_K q \left(-\frac{\pi^2}{4} + \frac{2}{\sqrt{\pi q}} \right) - \frac{\pi^2}{4} \frac{\eta}{l^2}. \quad (39)$$

The growth rate for large dynamo numbers, $|D| \gg \pi^4/16$, or for small η is

$$\Gamma = 0.3 \frac{\beta + \eta}{l^2} \sqrt{\pi |D|} = 0.3 \Omega_K \pi \sqrt{q}. \quad (40)$$

This differs from equation (19) by a negligible factor, ~ 0.35 , for $\alpha_{pl} = 1$, in view of the many approximations. We therefore conclude that mean field dynamo theory results in a growth rate similar to that predicted by the flux rotation analysis. In either case the growth is so rapid, in view of equation (26), that nearly the entire history of the accretion disk dynamo will be dominated by the near steady state saturated conditions. Unfortunately, this steady state is beyond the scope of the present paper, where instead we feel satisfied in demonstrating an understanding of the dynamo gain using a flux rotation model, a mean field theory, and numerical simulations.

We see that the filling factor $q(r)$ is crucial for the mean field dynamo. Let us estimate $q(r)$. The cross section area of the plume is $\pi r_{pl}^2 \approx \pi H^2$, and the number of plumes present at any moment of time on one side of the disk is $2(nv/4)(T_K/2)$. Therefore, we have

$$q = \frac{nv}{4} 2 \frac{T_K}{2} \pi H^2.$$

Using expression (16) of Paper I for the flux of stars, $nv/4$, and expression (A5) of Paper I for the disk half-thickness, we obtain

$$q = 1.52 \times 10^{-3} n_5 \left(\frac{r}{10^{-2} \text{ pc}} \right) \left(\frac{l_E}{0.1} \right)^2 \left(\frac{\epsilon}{0.1} \right)^{-2} \\ \text{for } 10r_t < r < 10^{-2} \text{ pc}, \\ q = 0 \text{ for } r < 10r_t. \quad (41)$$

The ratio of the toroidal to the poloidal or radial magnetic field in the growing mode and inside the volume occupied by plumes is

$$\frac{B_T}{B_P} \approx |D|^{1/2} = \frac{2}{\sqrt{\pi q}}.$$

Using expression (41) for the value of q , we have

$$\frac{B_T}{B_P} \approx 63n_5^{-1/2} \left(\frac{r}{10r_i} \right)^{-1/2} \left(\frac{l_E}{0.1} \right)^{-1} \left(\frac{\epsilon}{0.1} \right).$$

As in all α - ω dynamos, the generated toroidal field is larger than the poloidal field. However, the toroidal field in the vacuum outside the region of dynamo activity vanishes, because the normal component of the current at the vacuum boundary must be zero. If there is conductivity, as we expect, and therefore force-free magnetic field above the plume region, then the toroidal magnetic field generated by the dynamo penetrates into this region (Reyes-Ruiz & Stepinski 1999). However, due to the quadrupole symmetry of the poloidal magnetic field, the toroidal field in the force-free corona has the opposite direction from the toroidal field inside the disk. The axial component of the magnetic field, B_z , is much smaller than the radial component inside the slab occupied by plumes, $B_z \approx (l/r)B_r$. However, the radial component of the magnetic field decreases down to the value comparable to B_z at $|z| = l$. The quadrupole poloidal field in the corona is weaker than the poloidal magnetic field inside the disk by the factor l/r . The structure of the force-free corona above the dynamo generation region cannot be determined without further knowledge about boundary conditions at the outer boundaries of the force-free region or physical processes, which limit the applicability of force-free ideal MHD approximation in the corona (i.e., fast reconnection of magnetic fields). If one requires that the magnetic field in the force-free region vanishes for $|z| \gg l$, as Reyes-Ruiz & Stepinski (1999) assume, then the toroidal magnetic field is comparable to the poloidal field in the corona. In this case, the toroidal magnetic field in the force-free corona is much smaller than the toroidal magnetic field inside the disk, and so we neglect it in the simulations. In the actual case of the black hole accretion disk dynamo, we expect the coronal field to be force-free and to progressively remove the flux and magnetic energy generated by the dynamo in a force-free helix as described in Li et al. (2001b), where the field strength, as discussed above, is of the order of the poloidal field.

5. THE DYNAMO EQUATIONS AND NUMERICAL METHOD

Because of limited numerical resolution and limited computing time, we cannot attempt to directly simulate the dynamo problem for the real astrophysical parameters. A three-dimensional simulation of just one star passage through the accretion disk is already quite a challenge for computational gas dynamics. Even if we assume that we know the velocity field for a single star-disk collision and treat only the kinematic dynamo problem, the existence of $\sim 10^4$ plumes, the necessity of good resolution in the space between and above the plumes, and long evolution times required by the dynamo problem make the direct computations very difficult and demanding of major computer resources. Numerical modeling done in this work illustrates and proves essential features of the star-disk collisions dynamo described above. We simulate the kinematic dynamo with only a few plumes present and adopt a simplified flow model for individual plumes. Then, we compare the numerical growth rate and magnetic field structure to the predictions of flux rotation and mean field theories extrapolated to a small number of plumes. Qualitative agreement between all three approaches in the limit of only a few plumes is observed.

5.1. Basic Equations

We have computed order-of-magnitude estimates of the growth rate and threshold for the dynamo by direct numerical simulations. For that purpose we have written a 3D kinematic dynamo code evolving the vector potential \mathbf{A} of the magnetic field in a given velocity field \mathbf{v} and with resistive diffusion. The code is written in cylindrical geometry. We start with the equations describing the evolution of fields in nonrelativistic quasineutral plasmas:

$$\nabla \cdot \mathbf{B} = 0, \quad (42)$$

$$\frac{1}{c} \frac{\partial \mathbf{B}}{\partial t} = -\nabla \times \mathbf{E}, \quad (43)$$

$$\nabla \times \mathbf{B} = \frac{4\pi}{c} \mathbf{j}, \quad (44)$$

$$\mathbf{j} = \sigma \left(\mathbf{E} + \frac{1}{c} \mathbf{v} \times \mathbf{B} \right), \quad (45)$$

where σ is the conductivity of the plasma. Because we are considering the kinematic dynamo, \mathbf{v} is specified and the momentum equation is ignored. Substituting the expression for the current \mathbf{j} from equation (44) into Ohm's law (eq. [45]) and introducing a coefficient of magnetic diffusivity η as $\eta = c^2/(4\pi\sigma)$, we obtain Ohm's law in the form

$$\mathbf{E} + \frac{1}{c} \mathbf{v} \times \mathbf{B} = \frac{\eta}{c} \nabla \times \mathbf{B}, \quad (46)$$

subject to the constraint of equation (42).

The conventional and widely accepted way of writing and solving the kinematic MHD equations (MHD without the hydrodynamical part) is to obtain a single equation for the evolution of the magnetic field. Substitution of the electric field \mathbf{E} from equation (46) into Faraday's law, equation (43), results in

$$\frac{\partial \mathbf{B}}{\partial t} = -\nabla \times (\eta \nabla \times \mathbf{B}) + \nabla \times (\mathbf{v} \times \mathbf{B}). \quad (47)$$

Introducing the vector potential \mathbf{A} with

$$\mathbf{B} = \nabla \times \mathbf{A},$$

equation (47) takes the form

$$\frac{\partial \mathbf{A}}{\partial t} + \eta \nabla \times \nabla \times \mathbf{A} - \mathbf{v} \times (\nabla \times \mathbf{A}) + c \nabla \varphi = 0, \quad (48)$$

where φ is the scalar potential; no gauge has been chosen. Any solution of equation (48) satisfying the boundary and initial conditions for the magnetic field should give a physical result for the evolution of the magnetic field. Equation (48) has the same second order in space derivatives as equation (47) for the evolution of the magnetic field.

The gauge freedom can be used to simplify the procedure for solving equation (48). The scalar potential φ may be chosen to be an arbitrary function by an appropriate choice of gauge transformation. For instance, we can choose to set $\varphi = 0$, in which case the remaining equation for \mathbf{A} takes the form

$$\frac{\partial \mathbf{A}}{\partial t} + \eta \nabla \times (\nabla \times \mathbf{A}) - \mathbf{v} \times (\nabla \times \mathbf{A}) = 0. \quad (49)$$

The boundary conditions for \mathbf{A} should be consistent with the gauge chosen. In principle, equation (49) requires three separate boundary conditions for the components of \mathbf{A} . This number is the

same as the number of boundary conditions required to solve the equation for the evolution of the magnetic field (eq. [47]). Note, however, that there is still a freedom to add $\nabla\chi$ to \mathbf{A} and therefore to the boundary conditions for \mathbf{A} , where χ is an arbitrary time-independent function, and still preserve the gauge condition $\varphi = 0$. Although any arbitrary initialization of \mathbf{A} satisfying the boundary conditions can be allowed, many initializations would result in the same magnetic field \mathbf{B} . Initializing equation (47) $\nabla \cdot \mathbf{B} = 0$ is formally required. We have the following requirements for the boundary and initial conditions for \mathbf{A} :

1. There must be boundary and initial conditions on all three components of \mathbf{A} .
2. Boundary and initial conditions should be consistent with the gauge used.
3. The physical boundary conditions and the initial conditions for the magnetic and electric fields (or any other quantities) specific to a particular problem must be satisfied.

The last requirement means that the physical boundary conditions must be derivable from the boundary condition equations imposed on \mathbf{A} . The reverse is not necessarily true, i.e., for one specific set of physical boundary conditions there may be many possible boundary conditions for \mathbf{A} . The situation with the boundary conditions for \mathbf{A} is analogous to the situation with the initial conditions for \mathbf{A} . With this specification of initial and boundary conditions, the curl of the solution to equation (48) will be equal to the solution of equation (47).

If we choose to evolve the magnetic field directly, then in addition to the equation of evolution (eq. [47]), the magnetic field must obey the constraint $\nabla \cdot \mathbf{B} = 0$, which should be specified as an initial condition. Although it follows from equation (47) that, once initialized to zero, $\nabla \cdot \mathbf{B}$ will be kept equal to zero, the numerical methods used to solve equation (47) introduce discretization errors, which after a sufficient time can accumulate so that $\nabla \cdot \mathbf{B}$ is no longer zero (e.g., Lau & Finn 1993). Special procedures are employed in the codes to deal with this problem, such as “divergence cleaning.” However, in the evolution of the vector potential there are three equations (eq. [48]) to solve, with four dynamic variables (i.e., three components of \mathbf{A} and one scalar function φ). Therefore, we can use this one extra degree of freedom in choosing φ for a suitable gauge constraint without actually imposing any constraints on three components of \mathbf{A} . This will allow us freedom to choose the gauge and at the same time will not introduce the necessity of taking special measures in order to ensure that the gauge will be kept correctly throughout the computation. The magnetic field is then obtained by taking the curl of \mathbf{A} . This way, $\nabla \cdot \mathbf{B}$ vanishes automatically within the discretization error associated with approximating the curl by finite differencing.

In the simulations presented in this work we used the gauge

$$c\varphi - \mathbf{v} \cdot \mathbf{A} + \eta \nabla \cdot \mathbf{A} = 0. \quad (50)$$

One can show that for this gauge, the basic equation (48) reduces to

$$\frac{\partial \mathbf{A}}{\partial t} = -A^k \frac{\partial v^k}{\partial x^i} - (\mathbf{v} \cdot \nabla) \mathbf{A} + \eta \nabla^2 \mathbf{A} + (\nabla \cdot \mathbf{A}) \nabla \eta. \quad (51)$$

We choose this gauge (eq. [50]) because the resulting equation for \mathbf{A} is similar to the equation for the advection of a vector quantity. It has the familiar advection term $(\mathbf{v} \cdot \nabla) \mathbf{A}$ and diffusion term $\eta \nabla^2 \mathbf{A}$. The term $-A^k (\partial v^k / \partial x^i)$ corresponds to a stretching term

$(\mathbf{B} \cdot \nabla) \mathbf{v}$ in the equation for the advection of the magnetic field. Finally, the $(\nabla \cdot \mathbf{A}) \nabla \eta$ term is associated with the nonuniformity of electric conductivity. In this work we only consider the case where $\eta = \text{constant}$ and concentrate on the effects of the plasma flow producing the dynamo. Thus, this term drops out of the equations. Note that equation (51) is valid both for incompressible and compressible flows.

Finally, we present equation (51) written out in the cylindrical coordinate system, r, ϕ, z (corresponding unit vectors are $\mathbf{e}_r, \mathbf{e}_\phi$, and \mathbf{e}_z):

$$\begin{aligned} \frac{\partial A^r}{\partial t} = & - \left(v^r \frac{\partial A^r}{\partial r} + \frac{1}{r} v^\phi \frac{\partial A^r}{\partial \phi} + v^z \frac{\partial A^r}{\partial z} - \frac{1}{r} v_\phi A_\phi \right) \\ & - \left(A^r \frac{\partial v^r}{\partial r} + A^\phi \frac{\partial v^\phi}{\partial r} + A^z \frac{\partial v^z}{\partial r} \right) + \eta \left[\frac{1}{r} \frac{\partial}{\partial r} \left(r \frac{\partial A^r}{\partial r} \right) \right. \\ & \left. + \frac{1}{r^2} \frac{\partial^2 A^r}{\partial \phi^2} + \frac{\partial^2 A^r}{\partial z^2} - \frac{A^r}{r^2} - \frac{2}{r^2} \frac{\partial A^\phi}{\partial \phi} \right] + \frac{\partial \eta}{\partial r} (\nabla \cdot \mathbf{A}), \end{aligned} \quad (52)$$

$$\begin{aligned} \frac{\partial A^\phi}{\partial t} = & - \left(v^r \frac{\partial A^\phi}{\partial r} + \frac{v^\phi}{r} \frac{\partial A^\phi}{\partial \phi} + v^z \frac{\partial A^\phi}{\partial z} + \frac{1}{r} v^\phi A^r \right) \\ & - \left(A^r \frac{1}{r} \frac{\partial v^r}{\partial \phi} + A^\phi \frac{1}{r} \frac{\partial v^\phi}{\partial \phi} + A^z \frac{1}{r} \frac{\partial v^z}{\partial \phi} + \frac{1}{r} A^\phi v^r - \frac{1}{r} A^r v^\phi \right) \\ & + \eta \left[\frac{1}{r} \frac{\partial}{\partial r} \left(r \frac{\partial A^\phi}{\partial r} \right) + \frac{1}{r^2} \frac{\partial^2 A^\phi}{\partial \phi^2} + \frac{\partial^2 A^\phi}{\partial z^2} - \frac{A^\phi}{r^2} + \frac{2}{r^2} \frac{\partial A^r}{\partial \phi} \right] \\ & + \frac{1}{r} \frac{\partial \eta}{\partial \phi} (\nabla \cdot \mathbf{A}), \end{aligned} \quad (53)$$

$$\begin{aligned} \frac{\partial A^z}{\partial t} = & - \left(v^r \frac{\partial A^z}{\partial r} + \frac{1}{r} v^\phi \frac{\partial A^z}{\partial \phi} + v^z \frac{\partial A^z}{\partial z} \right) \\ & - \left(A^r \frac{\partial v^r}{\partial z} + A^\phi \frac{\partial v^\phi}{\partial z} + A^z \frac{\partial v^z}{\partial z} \right) \\ & + \eta \left[\frac{1}{r} \frac{\partial}{\partial r} \left(r \frac{\partial A^z}{\partial r} \right) + \frac{1}{r^2} \frac{\partial^2 A^z}{\partial \phi^2} + \frac{\partial^2 A^z}{\partial z^2} \right] + \frac{\partial \eta}{\partial z} (\nabla \cdot \mathbf{A}), \end{aligned} \quad (54)$$

where

$$\nabla \cdot \mathbf{A} = \frac{1}{r} \frac{\partial}{\partial r} (r A^r) + \frac{1}{r} \frac{\partial A^\phi}{\partial \phi} + \frac{\partial A^z}{\partial z}.$$

The gauge condition (eq. [50]) takes the form

$$c\varphi = v^r A^r + v^\phi A^\phi + v^z A^z - \eta \left[\frac{1}{r} \frac{\partial}{\partial r} (r A^r) + \frac{1}{r} \frac{\partial A^\phi}{\partial \phi} + \frac{\partial A^z}{\partial z} \right]. \quad (55)$$

Expressions for the magnetic field components in cylindrical coordinates are

$$\begin{aligned} B^r &= \frac{1}{r} \frac{\partial A^z}{\partial \phi} - \frac{\partial A^\phi}{\partial z}, \quad B^\phi = \frac{\partial A^r}{\partial z} - \frac{\partial A^z}{\partial r}, \\ B^z &= \frac{1}{r} \frac{\partial}{\partial r} (r A^\phi) - \frac{1}{r} \frac{\partial A^r}{\partial \phi}. \end{aligned} \quad (56)$$

5.2. Boundary and Initial Conditions

Although the use of the vector potential eliminates the problem with the divergence cleaning, the boundary conditions in

terms of the vector potential may be somewhat more complicated and not as obvious from an intuitive physical standpoint as the boundary conditions for magnetic fields. In this work we used perfectly conducting boundary conditions at all boundaries of the cylinder. There is no general agreement as to what boundary conditions are most physically appropriate for thick accretion disk dynamo simulations. For example, Stepinski & Levy (1988) used vacuum boundary conditions outside some given spherical domain for solving the mean field dynamo equations in axial symmetry. Khanna & Camenzind (1996a, 1996b) also considered an axisymmetric mean field dynamo in the disk and in the corona surrounding the disk on the Kerr background gravitational field of a rotating black hole. They used the artificial boundary condition that the magnetic field is normal to the rectangular boundary of their computational domain, and the poloidal component of the current density vanishes near the boundary. However, the main goal of these investigations was to demonstrate that certain types of helicity distributions inside the disk produce a dynamo. As soon as the boundary of the numerical domain is extended far enough from the region of large helicity and large differential rotation, the influence of the boundary conditions on the process of the generation of the magnetic fields far inside from the boundary should be small. Since both the Keplerian profile of the angular rotational velocity and the frequency of star-disk collisions have values increasing toward the central black hole, the approximation of a distant boundary can be applicable to the case of our simulations. Therefore, we have chosen a perfectly conducting rotating cylindrical boundary as a simple boundary condition prescription. We checked that the results of our simulations do not strongly depend on the position of the outer boundary.

The magnetic field near the rotation axis is strongly influenced by the presence of the black hole, as well as the general relativistic effects associated with the black hole. Magnetic field lines in the region close to the rotation axis have their footpoints on the black hole horizon or in the region between the black hole and the inner edge of the accretion disk. Therefore, one should expect that this region of the magnetosphere will also be strongly influenced by the relativistic effects of the black hole. The influence of the central black hole on the magnetic fields produced by the dynamo is a part of the so-called black hole electrodynamics theory (e.g., see the chapter “Electrodynamics of Black Holes” in Frolov & Novikov [1998]). Since the number density of stars should decrease near the black hole due to their capture by the black hole and due to tidal disruption, one should not expect the star-disk collision dynamo to operate effectively in this region, where strong relativistic effects are important. Therefore, for the purpose of this work we replace the region close to the axis of symmetry by imposing an inner cylindrical boundary (also perfectly conducting). This may be adequate to the real astrophysical situation in the coroneae of the accretion disks, since there is highly conducting plasma there.

We choose as an initial condition a purely poloidal magnetic field with even symmetry with respect to the plane of the disk (see Appendix A for definitions and properties of odd and even magnetic fields). The field is contained within the computational boundaries such that the normal component of the magnetic field is zero on all boundaries.

Let us consider the perfectly conducting rotating boundaries. There is no magnetic flux penetrating the boundaries. This means that the normal component of the magnetic field must always remain zero on the boundary. If the velocity of the boundary is \mathbf{v}_b , then the tangential component of electric field in the rest frame of the moving boundary $\mathbf{E} + \mathbf{v}_b/c \times \mathbf{B}$ is also zero on the boundary.

If \mathbf{v}_b and \mathbf{B} are both tangential at the boundary, then this implies that the tangential component of \mathbf{E} is also zero there. This then implies that we can choose the φ and the tangential components of \mathbf{A} to be zero on the boundary. Then, from expression (50) and the vanishing of the normal component of \mathbf{v} on the boundary, we conclude that we must have $\nabla \cdot \mathbf{A} = 0$ there. Specifically, we have

$$\frac{1}{r} \frac{\partial}{\partial r}(rA^r) = 0, \quad A^\phi = 0, \quad A^z = 0 \quad (57)$$

on the $r = \text{constant}$ boundary and

$$A^r = 0, \quad A^\phi = 0, \quad \frac{\partial A^z}{\partial z} = 0 \quad (58)$$

on the $z = \text{constant}$ boundary. This forms a complete set of three boundary conditions for three components of \mathbf{A} on each boundary, which is compatible with both the physical requirements for fields on a perfectly conducting boundary and the gauge condition (eq. [50]). We can also see that the equations (57) and (58) are consistent in the corners of the computational domain, i.e., at the intersections of the planes $z = \text{constant}$ and cylinders $r = \text{constant}$.

5.3. The Numerical Scheme

We use the finite differences predictor-corrector scheme to solve equations (52)–(54) in cylindrical coordinates. For approximating advection and stretching terms, we use central differencing, which gives second-order accuracy in the coordinates. The diffusion term is approximated by the usual seven-point stencil. Since the numerical method is explicit, it requires the stability condition to be satisfied. Let us denote discretization intervals in coordinates and time as Δr , $\Delta \phi$, Δz , and Δt and define the quantities $s_r = \eta \Delta t / (\Delta r^2)$, $s_\phi = \eta \Delta t / (r^2 \Delta \phi^2)$, and $s_z = \eta \Delta t / (\Delta z^2)$ and $C_r = v_r \Delta t / (\Delta r)$, $C_\phi = v_\phi \Delta t / (r \Delta \phi)$, and $C_z = v_z \Delta t / (\Delta z)$. Then, the stability conditions that we used in our simulations are

$$s_r + s_\phi + s_z < \frac{1}{2}, \quad (C_r + C_\phi + C_z)^2 < 2(s_r + s_\phi + s_z). \quad (59)$$

One can show that these conditions follow from the local linear stability analysis of the dynamo equations (52)–(54). Before doing each new cycle of predictor-corrector calculations, we set up the value of the time step Δt . First, we choose some reasonable value of Δt dictated by the accuracy requirements or how frequently we want to get output measurements from our simulations. Then, we decrease the value of Δt until the first of the conditions in equation (59) is satisfied. After that we check the second condition in equation (59) and see if it is satisfied. If not, then we decrease Δt further. We can see that the second condition in equation (59) will be always satisfied at some value of Δt , since the right-hand side depends on Δt linearly while the left-hand side depends on Δt quadratically. The first stability criterion is the usual one for the diffusion equation and means that the diffusion per single time step propagates no further than through only a single grid cell. The second condition is specific for central differences in the advection term and means that the distance the magnetic field is advected during one time step Δt is less than the distance through which the field diffuses per single time step

Δt (e.g., Fletcher 1992). In practice, we ensure stability by using a safety coefficient of 0.9 in the inequalities (eq. [59]).

When coding the boundary conditions (57) and (58), we used a second-order one-sided difference scheme for approximating derivatives. The resulting expressions have been solved for the unknown value of the component of \mathbf{A} at the point on the boundary. Boundary conditions have been updated after both predictor and corrector steps. In the ϕ -direction, seamless periodic boundary conditions have been used, i.e., we make the first and last grid points in the ϕ -direction identical and corresponding to $\phi = 0$ and 2π and use the same difference scheme as for other values of ϕ to update these points. We used the same seamless treatment of lines $\phi = 0$ and 2π at the radial cylindrical boundaries and at the top and bottom boundaries.

The code is able to treat both the domains with an inner radial boundary and the domains that include the symmetry axis. In the latter case, there is a singularity of the grid at $r = 0$, namely, all grid points having $r = 0$ and all values of ϕ from 0 to 2π coincide. We need a special treatment of the grid points at $r = 0$ to ensure the regularity of the Cartesian components A^x , A^y , and A^z of \mathbf{A} and the correct asymptotes for A^r , A^ϕ , and A^z . If the values of the Cartesian components at $r \rightarrow 0$ are A_0^x , A_0^y , and A_0^z , then the asymptotic behavior of the polar components is $A^r \rightarrow A_0^x \cos \phi + A_0^y \sin \phi$, $A^\phi \rightarrow -A_0^x \sin \phi + A_0^y \cos \phi$, and $A^z \rightarrow A_0^z$. To impose these asymptotic conditions, we first interpolate A_0^x , A_0^y , and A_0^z by calculating the average over ϕ of the Cartesian components of the vector potential at grid points situated on a ring with radius Δr . We take this average for A_0^x , A_0^y , and A_0^z . Then, we assign the values of the components of \mathbf{A} in the cylindrical coordinate system at $r = 0$ according to $A^r(\phi) = A_0^x \cos \phi + A_0^y \sin \phi$, $A^\phi(\phi) = -A_0^x \sin \phi + A_0^y \cos \phi$, and $A^z(\phi) = A_0^z$. This finalizes the prescription for the boundary condition at $r = 0$. When the symmetry axis $r = 0$ is included in the computational region, the code slows considerably because of the small ($\Delta\phi\Delta r$) distance between grid points in the ϕ -direction and, therefore, more restrictive limitations on the time step imposed by the first of the conditions of equation (59).

5.4. Code Testing

In the process of writing the code, we performed tests for separate parts of the code and then for the complete code itself. The diffusion part of the code has been tested by reproducing the analytical solution for eigenmodes of the diffusion equation $\partial\mathbf{A}/\partial t = \eta\nabla^2\mathbf{A}$ with $\mathbf{A} = 0$ boundary conditions. A variety of different eigennumbers have been tested, and decay rates are found to be in excellent agreement with analytic expressions. The code preserves the shape of eigenmodes with very high accuracy even for a very moderate number of nodes. Coupling between equation (52) for A^r and equation (53) for A^ϕ has been tested by evolving non-axisymmetric eigenmodes.

The advection part of the code has been tested by computing the advection by the uniform flow of the magnetic field of the type $\mathbf{B} = B\mathbf{n}$, where \mathbf{n} is a fixed vector of unit length (we made a few runs with different directions of \mathbf{n}), and the magnitude of the magnetic field B has the constant gradient vector $\nabla B = \text{constant}$ perpendicular to \mathbf{n} . The current density corresponding to such a magnetic field is uniform, and therefore the magnetic field does not diffuse. The boundary condition for this test was set to time-dependent explicit values computed from the known purely advective behavior of the field. We observed good agreement with the picture of the pure advection of flow.

We also compared the results for dynamo simulations with the two-dimensional (2D) flow given by our code to the simulations

produced by two other 2D kinematic dynamo codes, one evolving the vector potential and another evolving the magnetic field. The latter 2D code has a divergence cleaning procedure for $\nabla \cdot \mathbf{B}$. The flow was an axisymmetric Beltrami flow with $\nabla \times \mathbf{v} = \lambda \mathbf{v}$. For the interior of the domain $0 < r < R_o$ and $0 < z < L$, one can obtain the following analytic solution for the Beltrami flow:

$$\begin{aligned} v^r &= J_1 \left(j_{11} \frac{r}{R_o} \right) \frac{\pi}{L} \sin \frac{\pi z}{L}, \\ v^z &= \frac{j_{11}}{R_o} J_0 \left(j_{11} \frac{r}{R_o} \right) \cos \frac{\pi z}{L}, \\ v^\phi &= \lambda_B J_1 \left(j_{11} \frac{r}{R_o} \right) \cos \frac{\pi z}{L}, \end{aligned}$$

where $J_0(x)$ and $J_1(x)$ are the Bessel functions, j_{11} is the first root of $J_1(x) = 0$, and $\lambda_B^2 = j_{11}^2/R_o^2 + \pi^2/L^2$. The solution can also be written in terms of the flux function $\Psi(r, z)$:

$$\begin{aligned} \Psi &= r J_1 \left(j_{11} \frac{r}{R_o} \right) \cos \frac{\pi z}{L}, \\ v^r &= -\frac{1}{r} \frac{\partial \Psi}{\partial z}, \quad v^z = \frac{1}{r} \frac{\partial \Psi}{\partial r}, \quad v^\phi = \frac{\lambda_B \Psi}{r}. \end{aligned}$$

The 3D kinematic code picks up the fastest growing mode of the dynamo. In the case of axisymmetric flows, the nonaxisymmetric modes of the field ($\propto e^{im\phi - i\omega t}$) with different azimuthal wave-number m evolve separately. The fastest growing mode in our simulations was with $m = 1$. The growth rate and the structure of the $m = 1$ modes obtained with 3D and 2D codes agree remarkably well. We also studied the convergence with respect to the grid resolution and found that for a magnetic Reynolds number Rm (defined as the product of maximum velocity and minimum of L and R_o) of about 200 the simulations converge for the grid resolution of about $41 \times 61 \times 41$ in the r -, ϕ -, and z -directions, respectively.

6. RESULTS OF NUMERICAL SIMULATIONS

6.1. Model of the Flow Field

We now approximate the flow for our kinematic code from the analysis of the simplified model of plumes in § 3. When describing the results of our numerical simulations, we use dimensionless units with the unit of length equal to the radius at which the star-disk collisions occur and the unit of velocity equal to the Keplerian velocity at that radius. Then, one turn of the disk at unit radius takes 2π dimensionless units of time. The disk is assumed to have constant thickness. Its top boundary is at $z = z_{\text{top}}$ and bottom boundary is at $z = z_{\text{bot}}$. We usually put the disk at $z = 0$, in the middle of computational cylindrical domain, and then $z_{\text{bot}} = -z_{\text{top}}$. However, we preserve separate notation for the top and bottom boundaries. For simplicity we assume that all star-disk collisions happen at unit radius, but are randomly distributed in azimuthal angle along $r = 1$. One remarkable feature of star-disk collisions is that the number of stars crossing the disk in both directions is equal on average. We consider two models for the position of star-disk collisions that address this property. In the first model we assume that collisions happen in pairs; at each time there are two collisions at $r = 1$, one with the star going up through the disk and the other at the opposite point on the circle $r = 1$ with the star going down through the disk. Thus, at

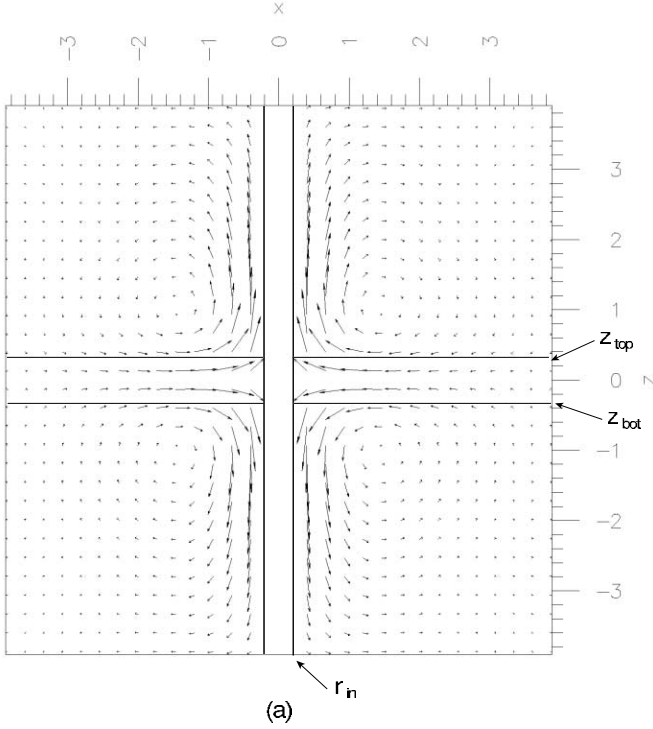


FIG. 2.—Initial even (quadrupole) axisymmetric poloidal magnetic field in the simulation box.

any moment of time the flow is symmetric with respect to the inversion relative to the central point of the disk. The second model considers random directions of plumes, as well as random distribution of plumes over the circle $r = 1$. In § 6.3 we describe the results obtained with both models.

The plume flow is superimposed onto a background of Keplerian differential rotation occupying the whole computational domain $\mathbf{v}_K = (1/r^{1/2})\mathbf{e}_\phi$. A star-disk collision is simulated by a vertically progressing cylinder of radius r_{pl} in the corotation frame. The cylinder starts at the bottom of the disk, located at $z = z_{bot}$, penetrates the disk, and rises to a height of h above the disk. At the same time, the cylinder rotates about its axis opposite to the local Keplerian frame such that the cylinder does not rotate about its axis if viewed in laboratory frame (an inertial frame where the central black hole is at rest), but the axis corotates with the local Keplerian frame. By the time the plume reaches its highest point, $\pi/2$ radians of Keplerian rotation, the axis corotates with the Keplerian flow also by $\pi/2$ radians, on average. Since the cylinder does not rotate about its axis, the relative rotation between the cylinder and Keplerian flow corresponds to an untwisting of $\pi/2$ radians, when the local frame rotates $\pi/2$ radians as measured at the radius of the axis of the jet. The length of the cylinder is progressive with time and its velocity, $v_{pz} \approx v_K$. The vertical velocity of the gas inside the cylinder is constant and is equal to v_{pz} . After the time the plume rotates by $\pi/2$, it is stopped and the velocity field is restored to pure Keplerian differential rotation everywhere. This very simplified flow field captures the basic features of actual complicated flow produced by randomly distributed star-disk collisions. We also feel that elaborating on some of the details of the flow field, such as taking a more realistic distribution of star-disk collision points in r and introducing a weak and distributed downflow, is not warranted at the present initial stage of simulations in view of the fact that we do not know other important features of the flow (no actual hydrodynamic calculations have yet been performed). Our model

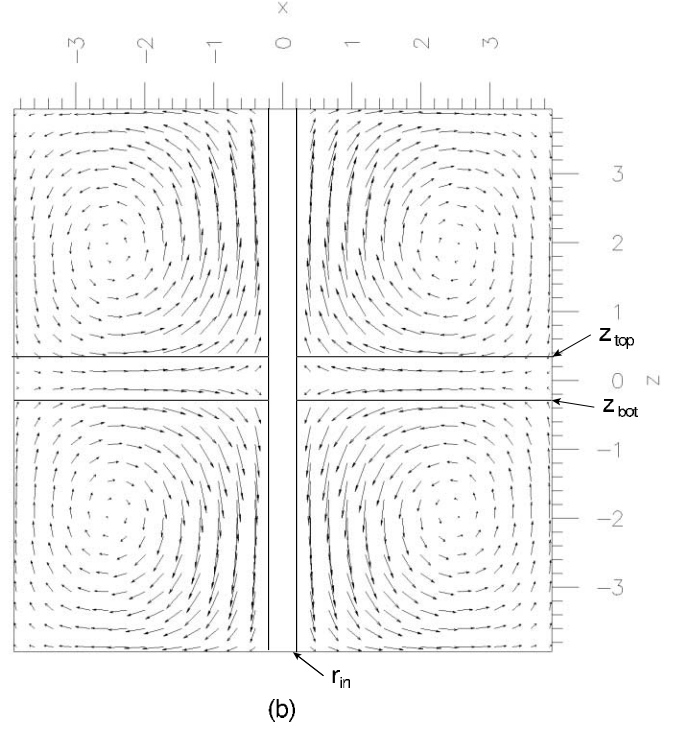


FIG. 3.—Diffusion of the initial poloidal magnetic field shown in Fig. 2. The axisymmetric poloidal field at time $t = 140$ is shown.

flow and simplified assumptions about star-disk collisions, frequency, and distribution capture qualitative features important for the excitation and symmetry properties of the dynamo. We feel that all elaborations mentioned above, as well as accurate simulations of star-disk collision hydrodynamics, would not

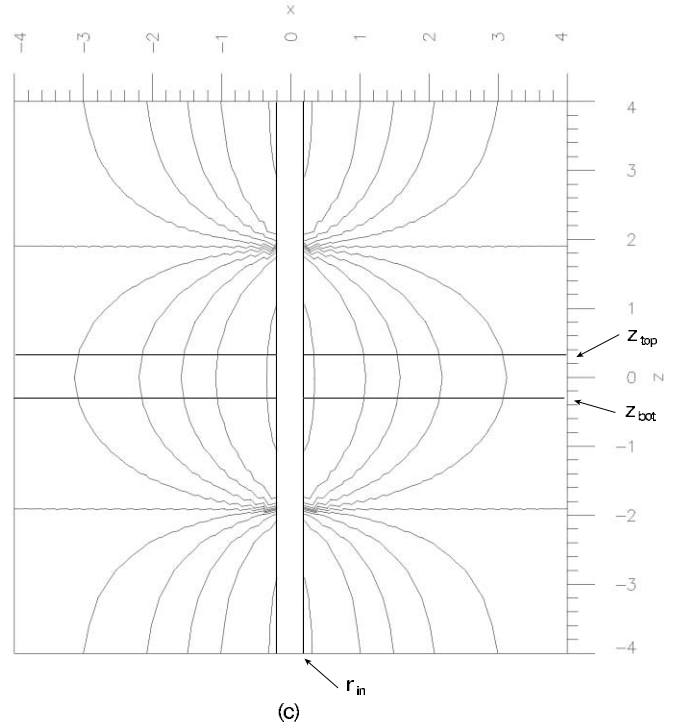


FIG. 4.—Toroidal magnetic field produced by differential rotation with the Keplerian angular velocity $\Omega_K = r^{-3/2}$ starting from the initial quadrupole poloidal magnetic field shown in Fig. 2. The contours of equal magnitude of the axisymmetric toroidal magnetic field at time $t = 140$ are shown.

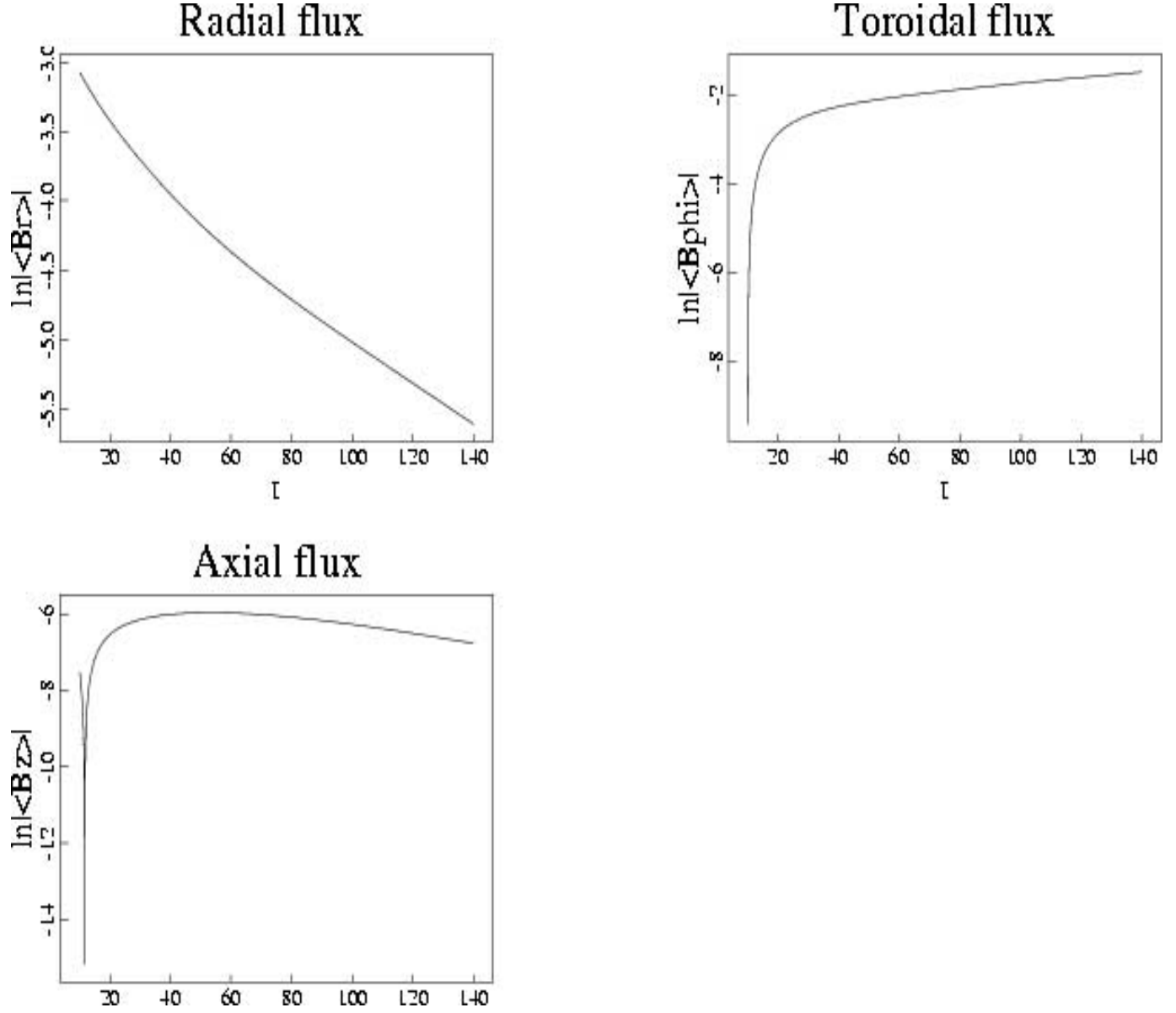


FIG. 5.—Evolution of fluxes of three components of magnetic field for the simulation presented in Figs. 2–4. Natural logarithms of the absolute value of fluxes are plotted vs. time. Flux of B_r is calculated through the part of the cylindrical surface $r = 2$ limited by lines $\phi = 0$, $\phi = \pi/2$, $z = 0$, and $z = 4$. Flux of B_z is calculated through the surface $z = 3$ limited by lines $r = R_1$, $r = R_2$, $\phi = 0$, and $\phi = \pi$. Flux of B_ϕ is calculated through the surface $\phi = 0$ limited by lines $r = R_1$, $r = R_2$, $z = 0$, and $z = 4$.

qualitatively change our conclusion about the possibility of such a dynamo.

Since equations (52)–(54) require spatial derivatives of the velocities, we apply a smoothing of discontinuities in the flow field described above. We also introduce smooth switching on and off of the plumes in time. For all three components of velocity v^k , we use the same interpolation rule for two plumes,

$$v^k = v_{in1}^k s_1 + v_{in2}^k s_2 + (1 - s_1 - s_2) v_{out}^k, \quad (60)$$

where $s_1(r, \phi, z, t)$ and $s_2(r, \phi, z, t)$ are smoothing functions for plumes 1 and 2, correspondingly. Each function s is close to 1 in the region of space and time occupied by the plume and is close to 0 in the rest of space and during times when the plume is off. Transition from 1 to 0 happens in the narrow layer at the boundary of the plume and during an interval of time that is short compared to the characteristic time of the plume rise. We define v_{in1}^k

and v_{in2}^k as the velocities of the flow of plumes 1 and 2, and v_{out}^k as the velocity of the flow outside the regions occupied by the plumes. For spatial derivatives of the velocity components, we have, from equation (60),

$$\begin{aligned} \frac{\partial v^k}{\partial x^i} = & \frac{\partial s_1}{\partial x^i} (v_{in1}^k - v_{out}^k) + \frac{\partial s_2}{\partial x^i} (v_{in2}^k - v_{out}^k) + s_1 \frac{\partial v_{in1}^k}{\partial x^i} \\ & + s_2 \frac{\partial v_{in2}^k}{\partial x^i} + (1 - s_1 - s_2) \frac{\partial v_{out}^k}{\partial x^i}. \end{aligned} \quad (61)$$

It is easy to generalize this approach for an arbitrary number of plumes.

Let us assume that the position of the axis of a cylindrical jet launched upward (in the positive direction of the z -axis) is $r = r_0$ and $\phi = \phi_0$. We keep $r_0 = 1$ for all plumes, and the initial ϕ_0 is randomly taken between 0 and 2π . Let us denote this plume as number 1 and the symmetric plume going down from the

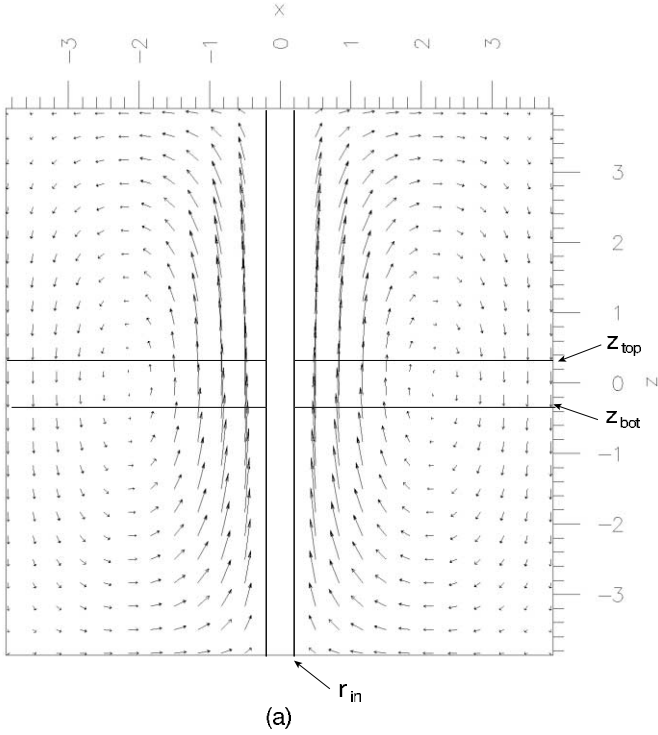


FIG. 6.— Evolution of the initial odd (dipole-like) poloidal magnetic field in differentially rotating plasma with the Keplerian angular velocity $\Omega_K = r^{-3/2}$. The poloidal axisymmetric magnetic field at time $t = 210$ is shown.

equatorial plane as number 2. Then, after time $(t - t_p)$ from the starting moment of the plume $t = t_p$, its position is

$$\phi_1 = \phi_0 + (t - t_p)r_0\Omega_{K0}, \quad (62)$$

where $\Omega_{K0} = \Omega_K(r_0)$ is the Keplerian angular rotational velocity at $r = r_0$ and in the simulations presented in this work, $\Omega_{K0} = 1$. The position of the axis of the symmetric plume is

$$\phi_2 = \phi_1 + \pi. \quad (63)$$

The radii of both plumes are r_{pl} . The bottom surface of plume 1 is at $z = z_{bot}$, the top surface of the plume 1 is at $z_1 = z_{bot} + v_{pz}(t - t_p)$, the top surface of the plume 2 is at $z = z_{top}$, and the bottom surface of the plume 2 is at $z_2 = z_{top} - v_{pz}(t - t_p)$. Due to symmetry, $z_2 = -z_1$. The velocity field inside the upward jet is

$$v_1^r = r_0\Omega_{K0} \sin(\phi - \phi_1), \quad (64)$$

$$v_1^\phi = r_0\Omega_{K0} \cos(\phi - \phi_1), \quad (65)$$

$$v_1^z = v_{pz}. \quad (66)$$

The velocity field inside the downward jet is

$$v_2^r = r_0\Omega_{K0} \sin(\phi - \phi_2), \quad (67)$$

$$v_2^\phi = r_0\Omega_{K0} \cos(\phi - \phi_2), \quad (68)$$

$$v_2^z = -v_{pz}. \quad (69)$$

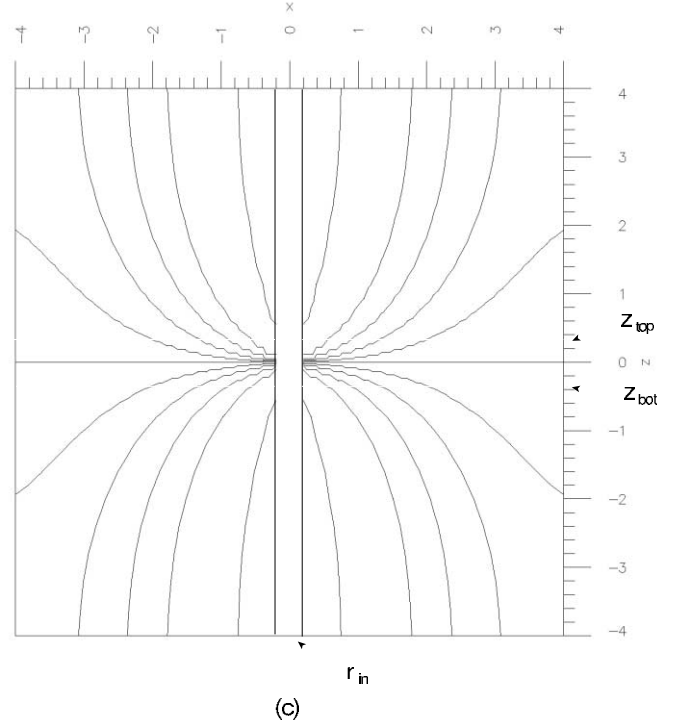


FIG. 7.— Evolution of the initial odd (dipole-like) poloidal magnetic field in a differentially rotating plasma with the Keplerian angular velocity $\Omega_K = r^{-3/2}$. The contours of toroidal axisymmetric magnetic field at time $t = 210$ are shown.

We choose the interpolation functions

$$s_1 = \left(\frac{1}{2} + \frac{1}{\pi} \arctan \frac{r_{pl}^2 - r_1'^2}{2r_{pl}\Delta} \right) \times \left[\frac{1}{2} + \frac{1}{\pi} \arctan \frac{(z - z_{bot})(z_1 - z)}{\Delta \sqrt{(z_1 - z_{bot})^2 + \Delta^2}} \right] S(t) \quad (70)$$

and

$$s_2 = \left(\frac{1}{2} + \frac{1}{\pi} \arctan \frac{r_{pl}^2 - r_2'^2}{2r_{pl}\Delta} \right) \times \left[\frac{1}{2} + \frac{1}{\pi} \arctan \frac{(z - z_{top})(z_2 - z)}{\Delta \sqrt{(z_{top} - z_2)^2 + \Delta^2}} \right] S(t), \quad (71)$$

where $r_1'^2 = r_0^2 + r^2 - 2r_0r \cos(\phi - \phi_1)$ is the distance from the axis of the plume 1, $r_2'^2 = r_0^2 + r^2 - 2r_0r \cos(\phi - \phi_2)$ is the distance from the axis of the plume 2, and Δ is the thickness of the transition layer of the functions s_1 and s_2 from their value 1 inside the plume to 0 outside the plume, with $\Delta \ll r_{pl}$. Square root expressions in the z -parts of s_1 and s_2 ensure that the thickness of the transition layer in the z -direction is never less than Δ , even just after the plumes are started, when the differences $(z_1 - z_{bot})$ and $(z_{top} - z_2)$ are zero. We choose $\Delta = 0.01$.

The function $S(t)$ ensures smooth “turning on” and “turning off” of the plumes at prescribed moments of time. If the plumes

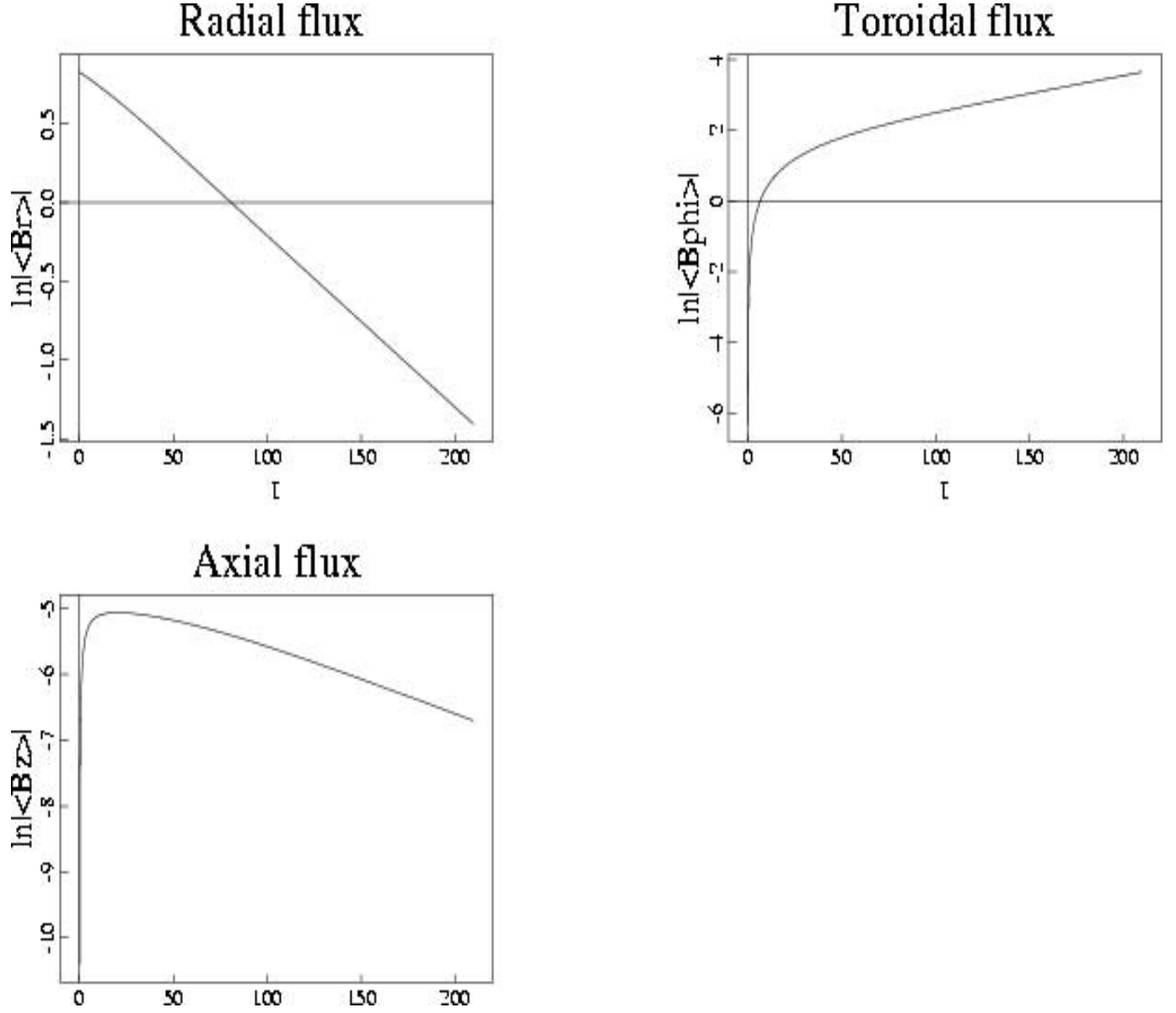


FIG. 8.— Evolution of fluxes of three components of magnetic field for the simulation presented in Figs. 6 and 7. Natural logarithms of the absolute value of the flux are plotted vs. time. The flux of B_r is calculated through the part of the cylindrical surface $r = 2$ limited by lines $\phi = 0$, $\phi = \pi/2$, $z = 0$, and $z = 4$. The flux of B_z is calculated through the surface $z = 3$ limited by lines $r = R_1$, $r = R_2$, $\phi = 0$, and $\phi = \pi$. The flux of B_ϕ is calculated through the surface $\phi = 0$ limited by lines $r = R_1$, $r = R_2$, $z = 0$, and $z = 4$.

are to be started at $t = t_p$ and to be turned off at $t = t_d$ ($t_d > t_p$), then we adopt the form of the function $S(t)$

$$S(t) = \begin{cases} 0 & \text{for } t < t_p - \delta t/2, \\ \frac{1}{2} + \frac{1}{2} \sin\left(\pi \frac{t - t_p}{\delta t}\right) & \text{for } t_p - \delta t/2 < t < t_p + \delta t/2, \\ 1 & \text{for } t_p + \delta t/2 < t < t_d - \delta t/2, \\ \frac{1}{2} - \frac{1}{2} \sin\left(\pi \frac{t - t_d}{\delta t}\right) & \text{for } t_d - \delta t/2 < t < t_d + \delta t/2, \\ 0 & \text{for } t > t_d + \delta t/2, \end{cases}$$

where δt is the length of the transition period, $S = 0$ corresponds to the flow without plumes, and $S = 1$ corresponds to the flow with plumes. We need to ensure that $\delta t < t_d - t_p$. We took $\delta t = (t_d - t_p)/5$. The cycles that have cylindrical jets present are

interchanged periodically with the cycles that have pure Keplerian rotation only. The time between two consecutive launchings of the plumes is Δt_p , and we always have $\Delta t_p > t_d - t_p$, such that at any time only one pair of plumes is present. This eliminates the occurrences of overlapping jets. Note that during time $t_d - t_p$ the disk makes only about one-quarter of the turn.

Our second model of random directions of the plumes introduces obvious changes into the expressions above. Namely, we set $s_2 = 0$ in equations (60) and (61), and we intermittently use either expressions (64)–(66) for the velocity, when the jet is directed upward, or expressions (67)–(69), when the jet is directed downward. We also use the same “switch” function $S(t)$ for both models.

Finally, let us list the parameters that are important for the growth of the magnetic field in our model: the magnetic diffusivity η (or magnetic Reynolds number $\text{Rm}_\Omega = r^2 \Omega_K(r)/\eta$), the radius of the

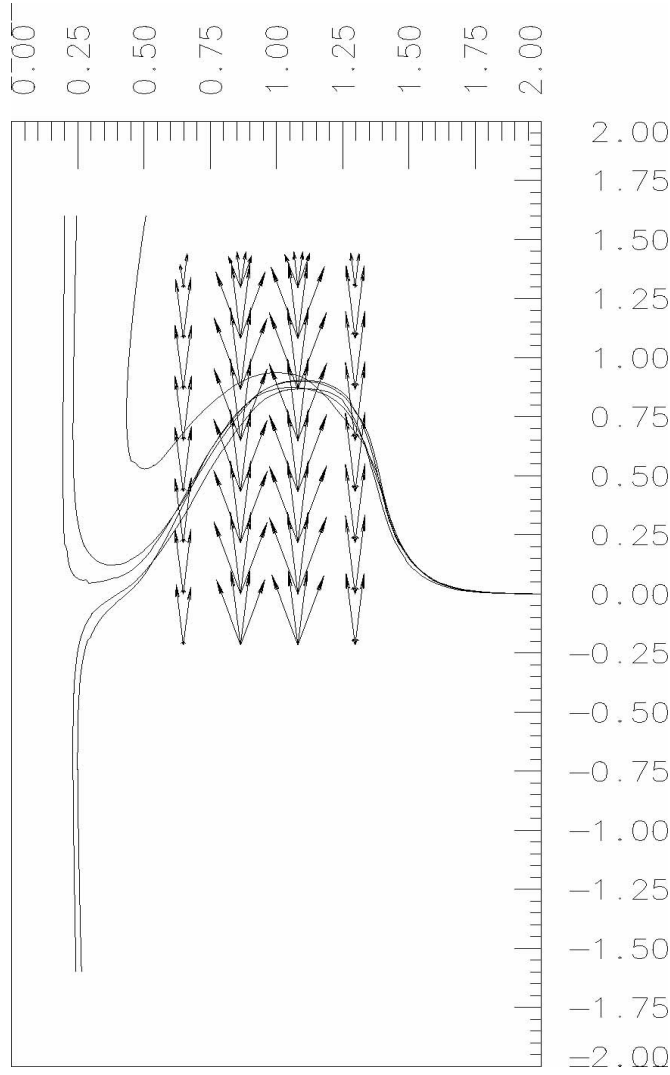


FIG. 9.—Distortion of magnetic field lines of a quadrupole field by a single cylindrical plume rising in a fluid, which is at rest. The side view is from the ϕ -direction. The picture shows the lifting of a bundle of field lines. Arrows indicate the velocities of the flow at different depths in the plume. The corkscrew motion of the plume is clearly seen on the side view.

plumes r_{pl} , the frequency of star-disk collisions, Δt_p , the vertical velocity of the plume v_{pz} , and the duration of the plumes $t_d - t_p$.

6.2. Analytic Solution in the Asymptotic Region

Because the equations for the evolution of the magnetic field \mathbf{B} and vector potential \mathbf{A} are parabolic, the boundary conditions will always influence the solutions inside the computational region. However, the distribution of the frequency of star-disk collisions is concentrated toward the center, meaning that most of dynamo activity happens in a limited region of space (around $r = 1$ in our dimensionless units). If one is willing to disregard a relatively small α -effect for $r \gg 1$, then the solutions of the field equations in the region $r \gg 1$ can be obtained analytically, because the flow is just the differential rotation with the Keplerian angular velocity.

The equations for the evolution of the axisymmetric magnetic field in the presence of only the differential rotation are analogous to equations (34) and (35) for the evolution of the axisymmetric mean field. We can obtain the necessary equations when replacing the mean field by the actual field and

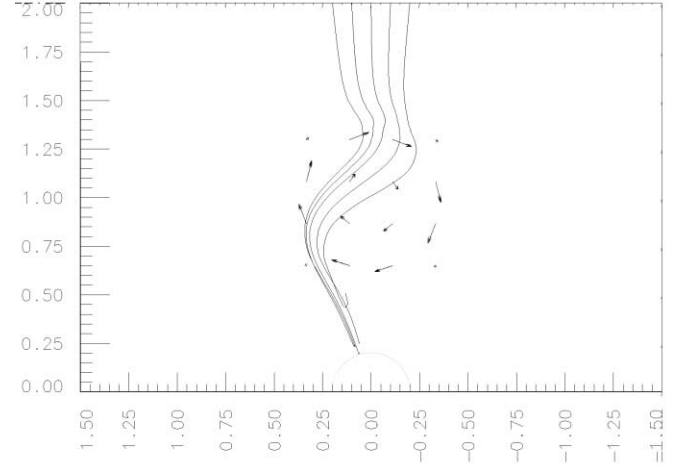


FIG. 10.—Same field configuration as Fig. 9, but viewed from the top z -direction. The picture shows the twisting of the bundle of field lines. Arrows indicate velocities of the flow. The time is the same as in Fig. 9.

using the same functions A and B_ϕ for the poloidal magnetic flux and toroidal magnetic field. If we set $\alpha = 0$, $\beta = 0$, $\mathbf{v}_p = 0$, and $\Omega = \Omega_K(r)$ in equations (34) and (35), the resulting equations for axisymmetric magnetic field in a purely rotating flow are

$$\frac{\partial A}{\partial t} = \eta \left(\nabla^2 A - \frac{1}{r^2} A \right), \quad (72)$$

$$\frac{\partial B_\phi}{\partial t} = r \frac{d\Omega_K}{dr} B_r + \eta \left(\nabla^2 B_\phi - \frac{1}{r^2} B_\phi \right). \quad (73)$$

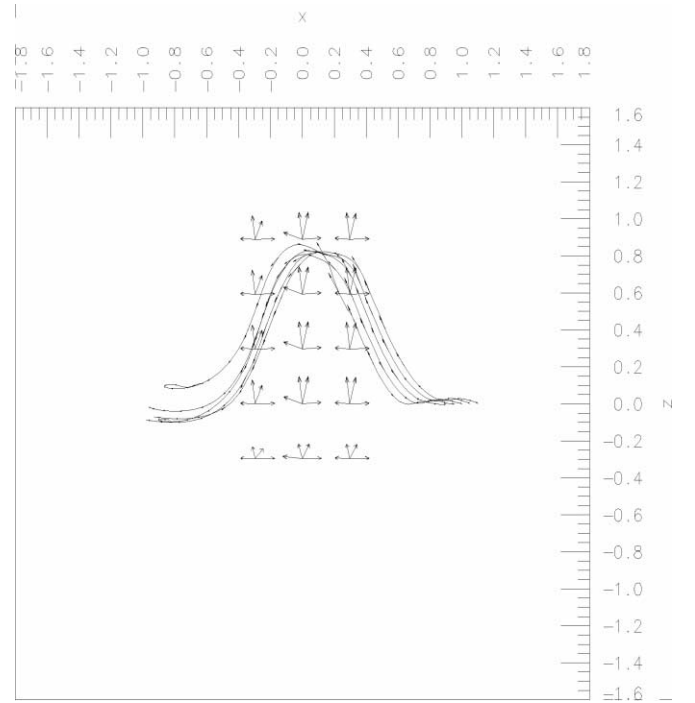


FIG. 11.—Creation of the poloidal magnetic field from the toroidal by the rising and unwinding jet produced by star-disk collisions in a differentially rotating plasma. Side view from r -direction. Arrows indicate velocities of the flow in the frame corotating with the base of the plume. The picture shows the rising bundle of field lines.

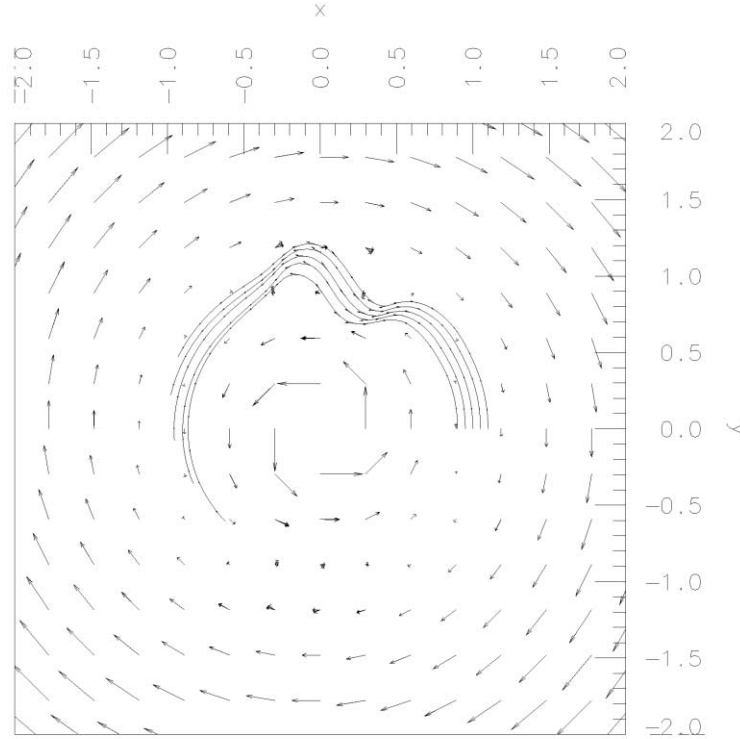


FIG. 12.— Same field configuration as Fig. 11, but viewed from the top z -direction. Arrows indicate the velocities of the flow in the frame corotating with the base of the plume. The picture shows the twisting of the bundle of field lines.

Equation (72) is a diffusion equation for the poloidal magnetic field without sources. Its solutions are determined by boundary conditions imposed on the poloidal magnetic field. Equation (73) is a diffusion equation for the toroidal magnetic field, but with the source term due to the Ω -effect. We see that the evolution of poloidal magnetic field is decoupled from the evolution of the toroidal magnetic field (unless boundary conditions mix them together). After we know the solution for the poloidal field, we can solve equation (73) to find the toroidal magnetic field. If we look for stationary solutions of equations (72) and (73), then the outer boundary condition is very important for determining the solution. However, in the case of a dynamo, the magnetic field in the dynamo domain $r \approx 1$ grows exponentially. This growing field diffuses into the surrounding conducting medium according to equations (72) and (73). The phenomenon is analogous to the skin layer in plasma. The growing magnetic field decreases exponentially outward from the generation region. Therefore, if the growth rate is sufficiently high that the skin depth is smaller than the distance to the ideally conducting boundary, the boundary conditions at the boundary do not influence the dynamo process.

We computed an analytic solution of equation (72) in the region $r > 1$ when the magnetic field grows exponentially. This solution is presented in Appendix B. We have checked with numerical simulations of the dynamo that the magnetic field in the zone outside of dynamo activity but inside the outer radius of our computational domain is very closely approximated by expression (B6), which result from our analytic solution. We also varied the outer sizes of the outer ideally conducting boundaries in our three-dimensional simulations to verify that the growth rate and the structure of the growing magnetic field are insensitive to the placement of the boundaries. It is necessary to stress that the simulations are insensitive to the boundary conditions only when the magnetic field is exponentially growing; the simulations in

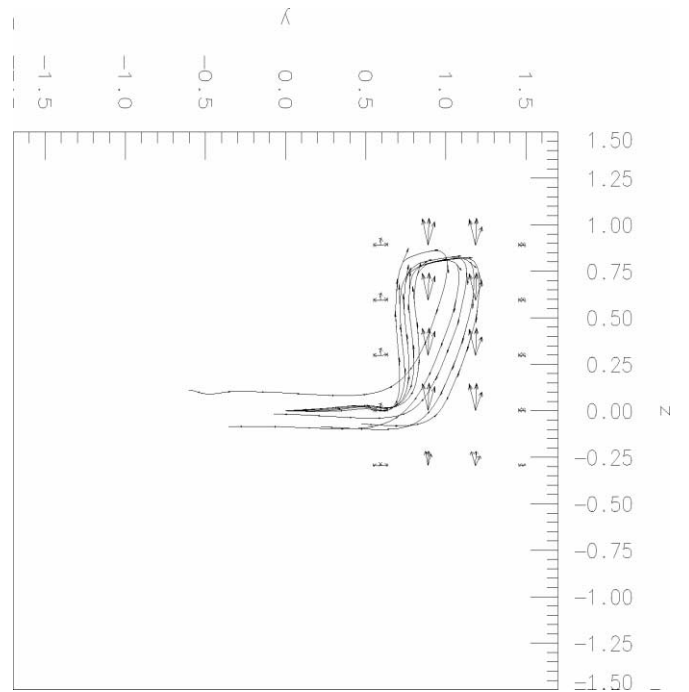


FIG. 13.— Same field configuration as Fig. 11, but viewed from the side ϕ -direction. Arrows indicate velocities of the flow in the frame corotating with the base of the plume. The picture shows the formation of the loop of poloidal field lines by the rising plume.

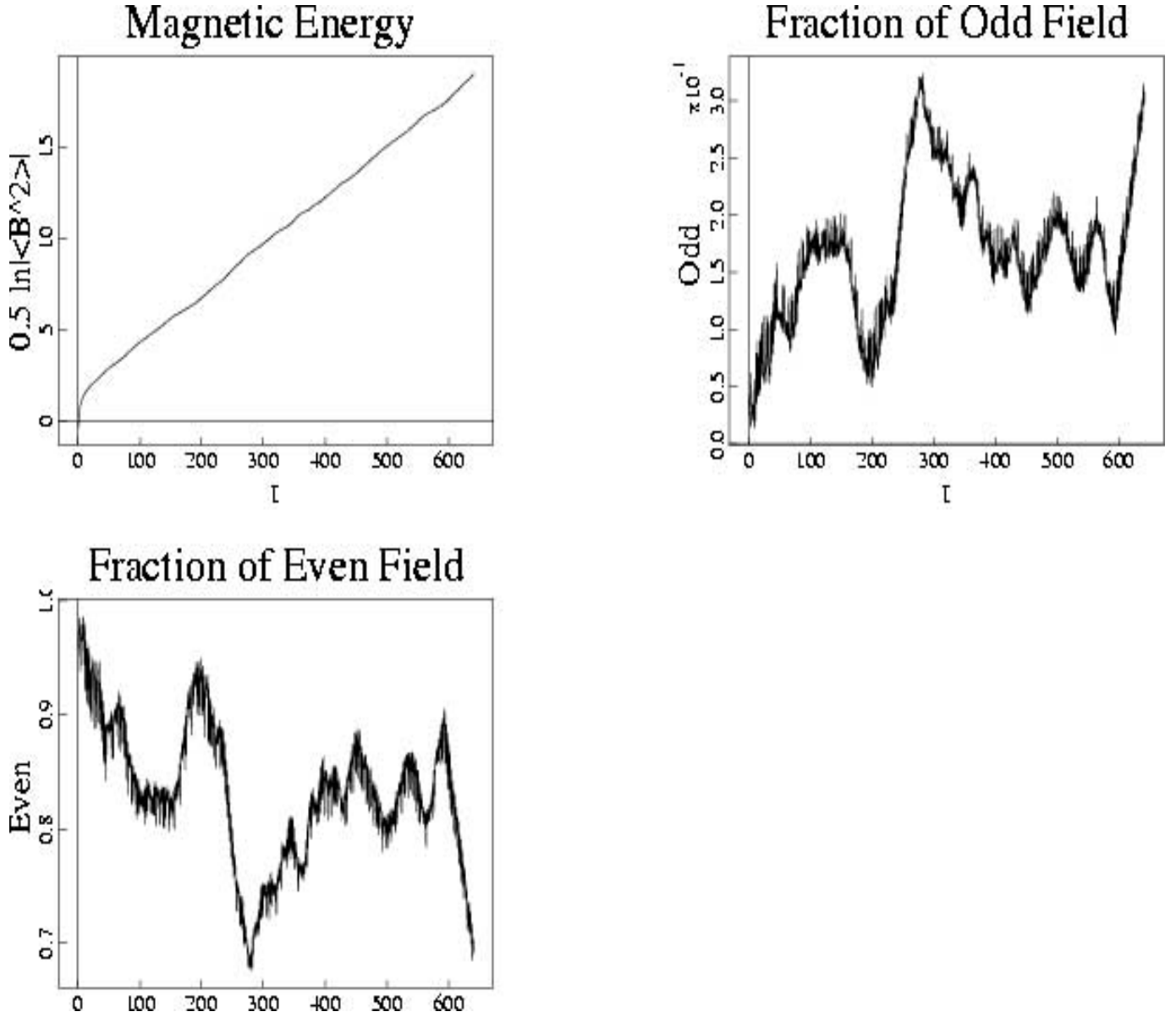


FIG. 14.—Exponential growth of the dynamo magnetic field. Half of the logarithm of the B^2 averaged over all computational domain is plotted vs. time in the top-left plot. Time evolution of the fractions of the energy of the odd and even components of the magnetic field is in the top-right and bottom-left plots. The sum of the fractions of odd and even components is always equal to 1.

the cases of decaying or steady fields do depend on how far away the ideally conducting boundaries are placed.

6.3. Simulations of the Dynamo Growth

The simulation is shown in a sequence of stages. We use the dimensionless units described in § 6.1. Our computational domain is the space between two cylinders with inner radius $R_1 = 0.2$ and outer radius $R_2 = 4$, filled with a media having uniform magnetic diffusivity η . The computational space is limited from below by the surface $z = -4$ and from above by the surface $z = 4$. The total length of the cylindrical volume between surfaces $z = -4$ and 4 is 8. All boundaries of the computational volume are ideally conducting. There is no magnetic field penetrating the boundaries, and the boundary conditions (57) and (58) are applied.

An initial quadrupole-like field establishes a primarily radial field within the midplane of the cylindrical volume, $|z| < 1/3$. The initial field is purely poloidal, concentrated toward the inner parts

of the disk, and is shown in Figure 2 by arrows. The accretion disk is indicated at $z_{\text{top}} = 1/3$ and $z_{\text{bot}} = -1/3$.

Keplerian differential rotation is initiated and generates the toroidal field. At the same time, the poloidal field diffuses toward the outer boundary and becomes distributed over the volume more uniformly. The magnetic diffusivity is $\eta = 0.01$, and the magnetic Reynolds number for rotation at $r = 1$ is $\text{Rm}_\Omega = r^2 \Omega_K(r) / \eta = 100$. With no source term present in equation (72), the poloidal magnetic field will decay away in a purely toroidal flow. The toroidal magnetic field B_ϕ will first grow because of the source term $r(d\Omega_K/dr)B_r$ in equation (73), then reach a saturation value $\approx B_r \text{Rm}_\Omega / (2\pi)$ determined by the balance between the source term $r(d\Omega_K/dr)B_r$ and the diffusion term $\eta(\nabla^2 B_\phi - r^{-2} B_\phi)$ in equation (73), and finally decay as the poloidal magnetic field B_r decays, and so the source term for B_ϕ also decays (Cowling's theorem).

Figure 3 illustrates the poloidal magnetic field obtained after several revolutions at $r = 1$, Figure 4 shows the contours of

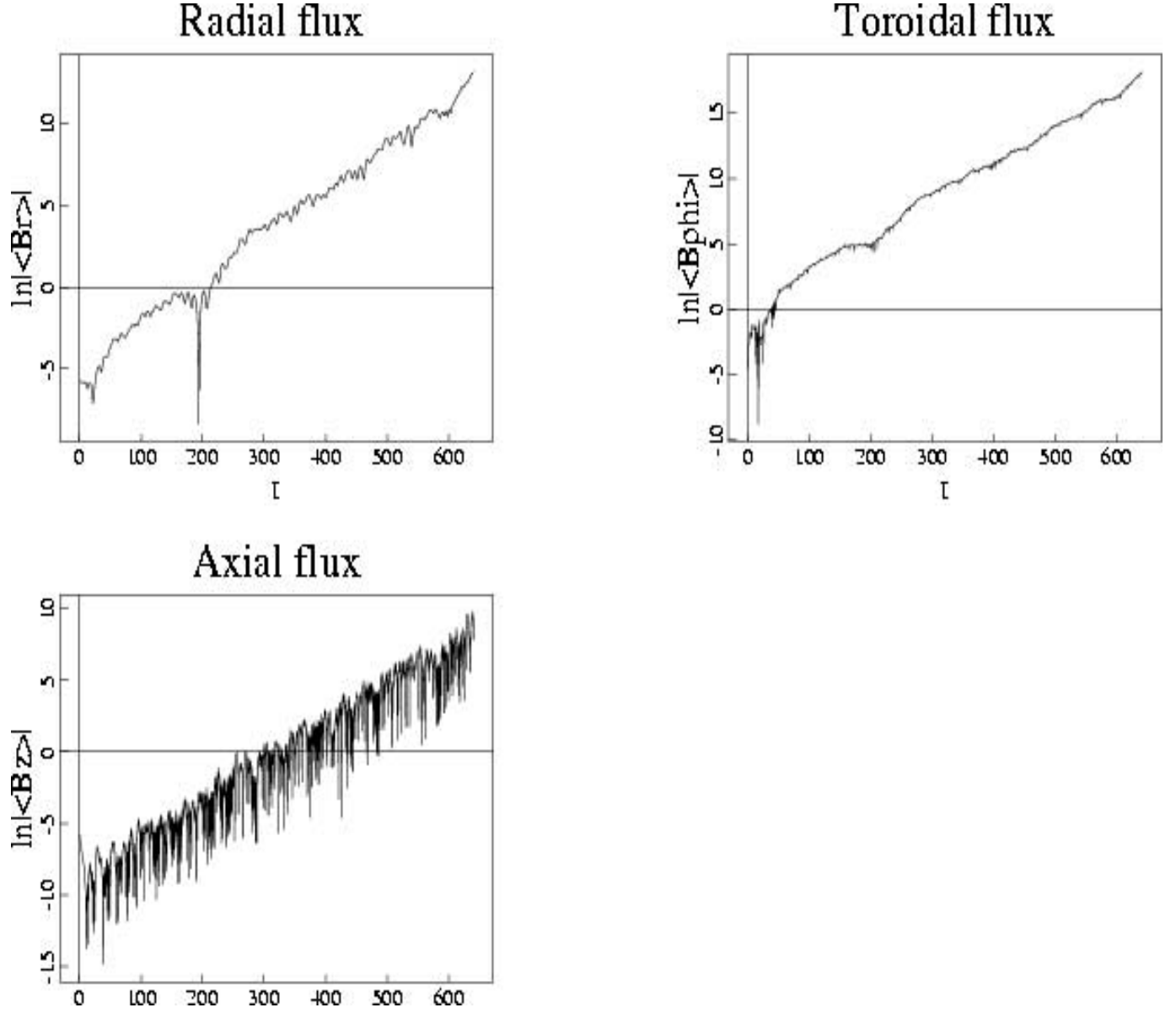


FIG. 15.—Time evolution of logarithms of the absolute values of the components of magnetic field averaged over the surfaces described in the text. Exponential growth of all three components is evident.

toroidal field at the same moment of time as in Figure 3. The time evolution of the fluxes of magnetic field is shown in Figure 5. We also show the process of winding up the dipole-like (odd) field in Figures 6 and 7 (poloidal and toroidal fields) and Figure 8 (the evolution of fluxes). Note that the toroidal field produced from the initial quadrupole field (and any even symmetry field) has the same sign throughout the disk thickness, as well as in the space above and below the disk. In contrast, the toroidal field produced from an initial dipole field (and any odd symmetry field) is zero at the equatorial plane and has opposite signs in the upper and lower halves of the disk thickness.

We now examine how the simulated star-disk collisions (approximated by a flow model described in § 6.1) deform the wound up, toroidal magnetic field and create poloidal field from the toroidal field. Figures 9 and 10 illustrate the action of the rising plume on the poloidal magnetic field in a fluid that is at rest. The initial magnetic field here is a quadrupole-like field, shown in Figure 2. The radius of the inner cylinder is 0.2 and the radius of the plume is 0.2. The velocity of the plume is equal to the

Keplerian velocity at $r = 1$ and the plume moves $\pi/4$ radians in the ϕ -direction before it disappears. Figure 9 is a side view on the plume. Figure 10 is a view on the plume from the top. One can clearly see the lifting of the field lines of the quadrupole field from the midplane of the disk by the plume flow. Because the plume flow is strongly compressible near the head of the plume, it forms a narrow layer of enhanced magnetic field near the top boundary of the plume. Magnetic field diffuses inside the plume from this layer. On the top view we can see the twisting of magnetic field lines by the unwinding of the flow in the plume. It creates toroidal field from the poloidal field. More importantly, Figures 11, 12, and 13 illustrate the action of the same plume on the primarily toroidal magnetic field wound up from the initial quadrupole field (as in Fig. 4). The plume rises through the differentially rotating fluid with the Keplerian profile of angular velocity. Figure 11 is a side view from the r -direction, Figure 12 is a top view from the z -direction, and Figure 13 is a side view from the ϕ -direction. The arrows show the flow velocity in the reference frame corotating with the base of the plume with the angular

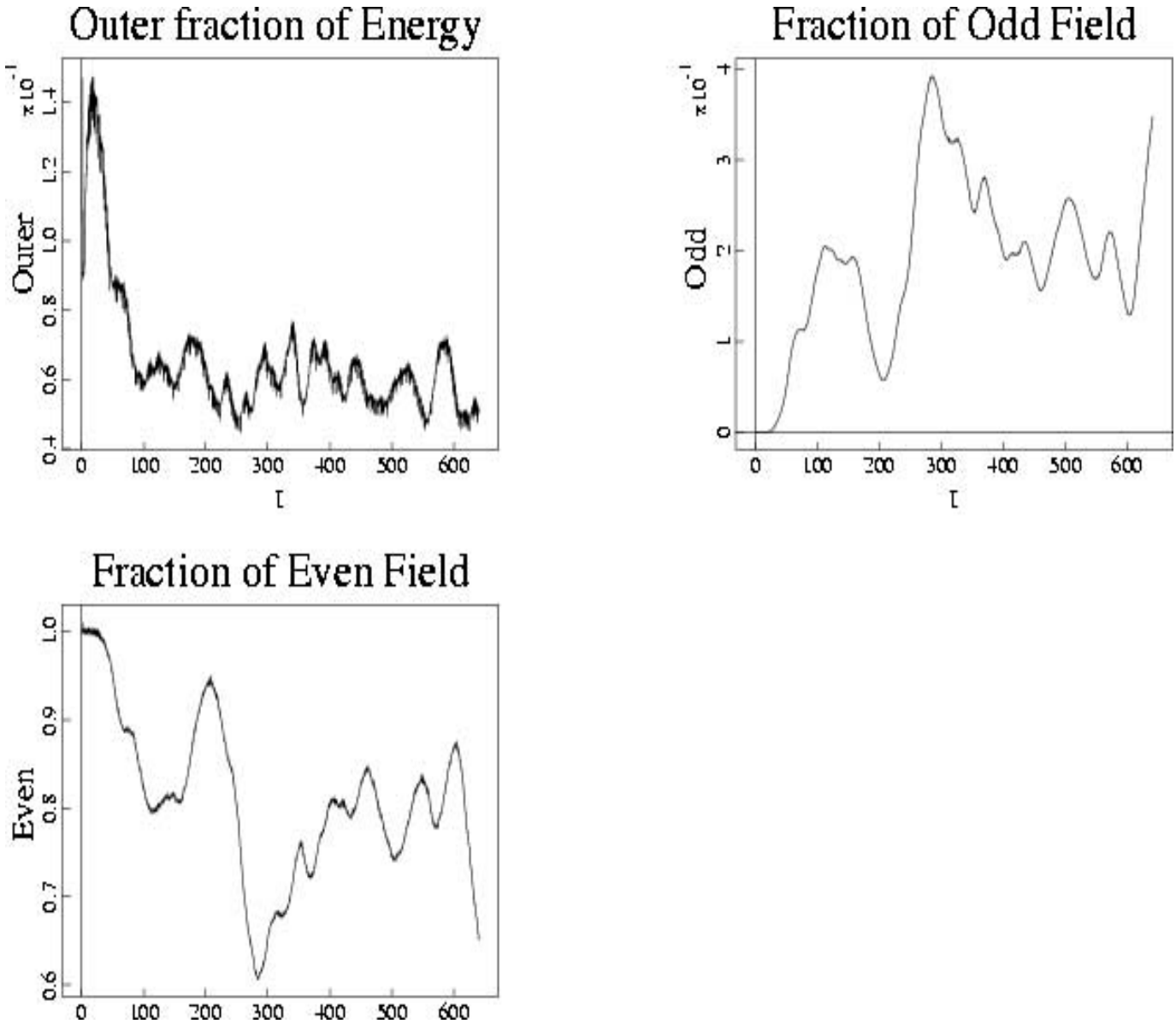


FIG. 16.—Time evolution of the ratio of the energy of the magnetic field in the outer domain to the total energy of the magnetic field in the computational domain (top-left). Time evolution of the fractions of energy of the odd and even components of the magnetic field in the outer domain is on the top-right and bottom-left plots. The sum of the fractions of odd and even components is always equal to 1.

velocity at the point of the location of the plume, i.e., the value $\mathbf{v}' = \mathbf{v} - \Omega_{K0} r \mathbf{e}_\phi$. As with Figure 9, the side view from the r -direction on Figure 11 shows the lifting up of the toroidal field by the rising plume. One can see from the projection viewed from the ϕ -direction that the magnetic field is entrained into forming a loop of poloidal field. The top view clearly shows the twisting of toroidal magnetic field and the creation of poloidal field from the toroidal field, i.e., the α -effect. The resulting loop of flux translated and rotated from the toroidal plane is shown at the time of maximum jet extension. After that time the jet velocities are smoothly set to zero.

By close examination of the positions of field lines in Figures 11, 12, and 13, one can discover the presence of another, more subtle effect; as the bundle of magnetic field lines is rotated and bent by the plume, magnetic field lines twist around each other in this bundle. The direction of this twist can be observed to be opposite to the direction of the helical twisting associated with the lifting and bending of the bundle as a whole. The bundle of

magnetic field lines behaves like a ribbon when it is bent and curved. The reason for the additional opposite twist of the magnetic field lines in this ribbon is the conservation of magnetic helicity (Blackman & Brandenburg 2003). This small-scale twist does not influence our flux rotation or mean field estimates of the kinematic stage of the dynamo.

The problem is continued with the jets or plumes repeated. The model of the flow described in § 6.1 is applied. Below, we present the results for a representative case for the model with the plumes randomly distributed along the circle $r = 1$ and launched in periodic intervals in random directions up and down through the disk. The parameters are (in the dimensionless units introduced in § 6.1) $R_1 = 0.2$, $R_2 = 4$, $\eta = 0.01$, $r_{pl} = 0.3$, $\Delta t_p = \pi/2 + 0.4$, $t_d - t_p = \pi/2$, $v_{pz} = 1$, $z_{bot} = -1/3$, and $z_{top} = 1/3$, and the centers of plumes are located on the circle $r = 1$. The run is started with the initial field being purely poloidal. The initial poloidal field is the linear superposition of odd and even magnetic fields shown in Figures 6 and 3, respectively. The exact

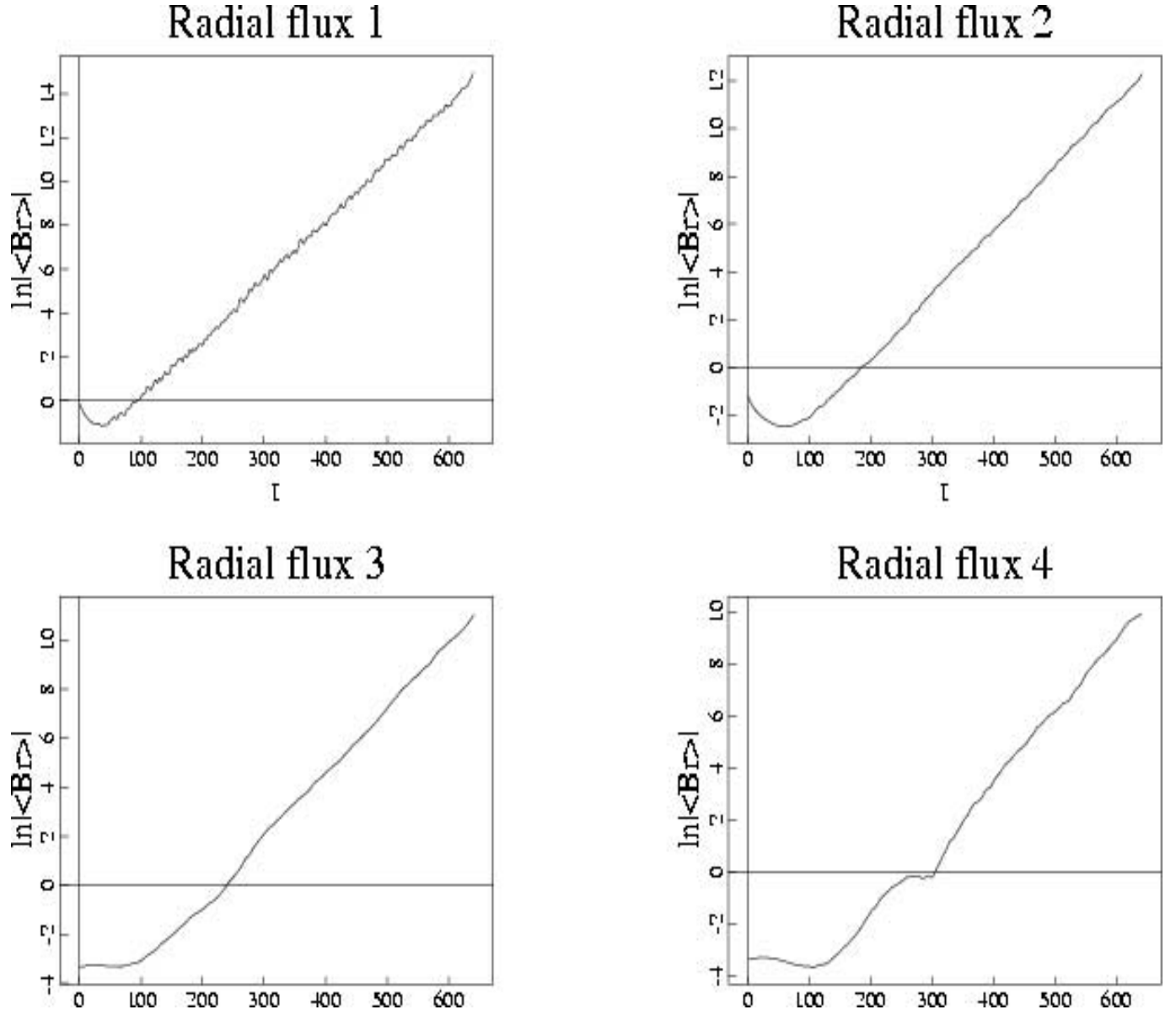


FIG. 17.—Time evolution of logarithms of the absolute values of the radial component of the magnetic field averaged over the four surfaces described in the text. All four surfaces are located in the outer region described in the text.

meaning of odd (dipole-like) and even (quadrupole-like) parity fields is described in Appendix A. Here we only note that the total energy of the magnetic field is equal to the sum of energies of odd and even components. The odd component contributes 5% of the total energy of the initial field. The remaining 95% of the total energy is the energy of the even field. The first plume is launched at the moment $t = 0.2$ after the beginning of the simulation, and the subsequent plumes are launched in periodic moments of time with the period Δt_p . This rate of plume launches corresponds to an average $2\pi/\Delta t_p = 3.2$ plume launches per revolution at $r = 1$. The simulation is continued until time $t = 640$. By that time the magnetic field grows by ~ 10 orders of magnitude. The resolution of our typical dynamo simulation is $41 \times 81 \times 41$ nodes in the radial, azimuthal, and vertical directions respectively. Although this resolution seems to be quite modest to resolve the plumes (there are typically only about 6×6 nodes to resolve the cross section of a plume), we checked the convergence of our simulations by performing trial runs with $61 \times 121 \times 61$ resolution. The growth rate of the dynamo and the structure of the

growing magnetic fields do not change with the increased resolution. We also performed trial runs with the larger size of the computational domain, $-6 < z < 6$ and $0.2 < r < 6$ with $61 \times 121 \times 61$ resolution. We did not observe significant changes of the growth rates and magnetic field structure of the dynamo when we increased the size of computational domain. The reasons for insensitivity to the boundary conditions are described above in § 6.2.

The time evolution of the total energy of the magnetic field integrated over the computational volume is presented in Figure 14, along with the time evolution of the fractions of total energy of odd and even components of the magnetic field. An arbitrary value of the initial magnitude of the magnetic field is used. The initial rapid growth of the energy is due to rapid buildup of the toroidal magnetic field. After a couple of revolutions at $r = 1$, the dynamo effect overcomes the linear growth of the toroidal magnetic field, and the growth of the magnetic energy becomes exponential. The magnetic field experiences oscillations with a period equal to Δt_p , due to the repeated actions of single plumes. More significant oscillations of odd and even components of the

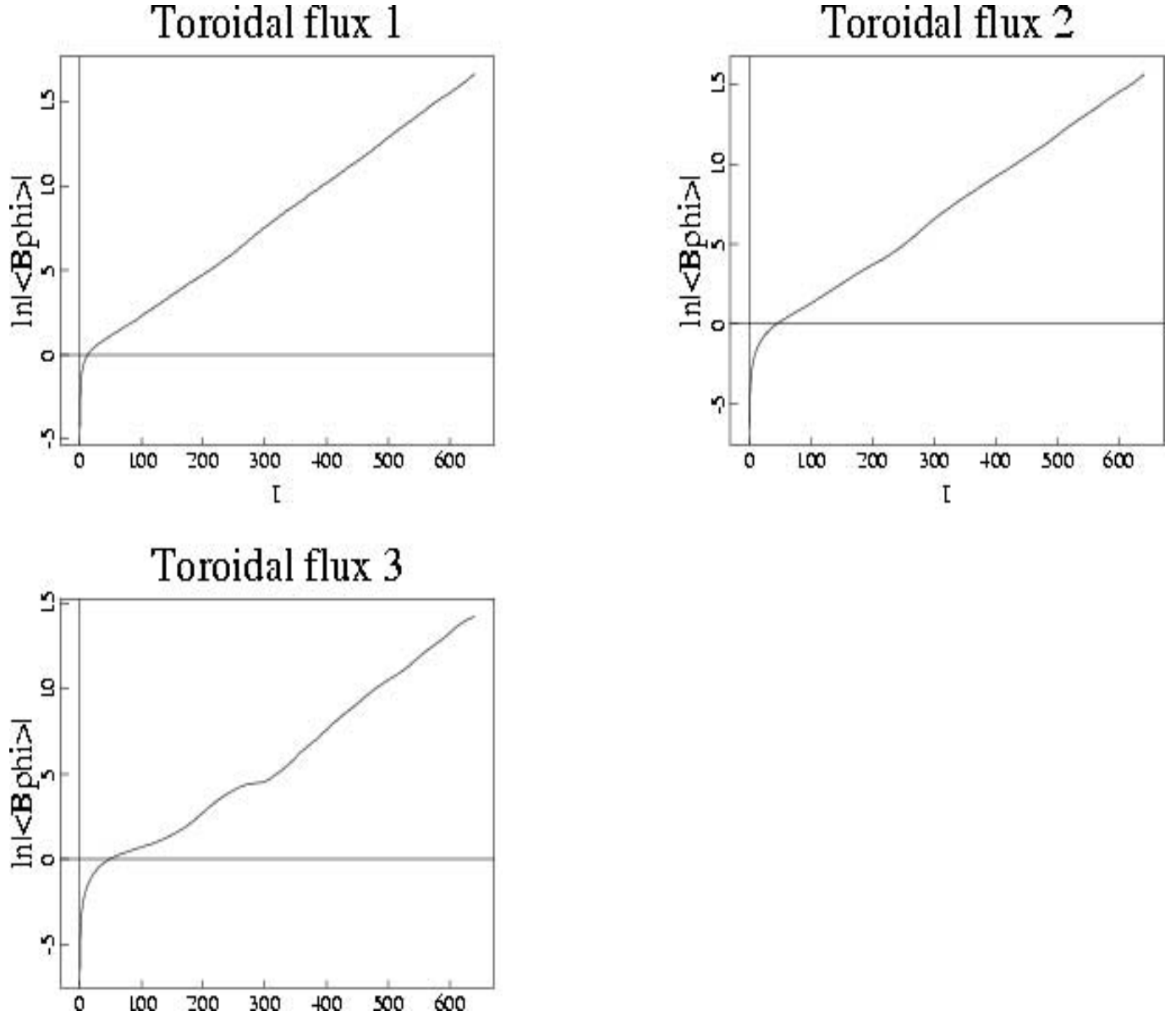


FIG. 18.—Time evolution of logarithms of the absolute values of the toroidal component of the magnetic field averaged over the three surfaces described in the text. All three surfaces are located in the outer region described in the text.

field occur on the timescale of the diffusion over the region of dynamo activity ≈ 100 . Despite the significant variation of the fraction of the odd field, which can become up to 30%, the even (quadrupole) field dominates. Since the flow does not have symmetry with respect to reflections $z \rightarrow -z$, the odd and even components of magnetic field are coupled to each other and grow with the same exponential rate.

The time evolution of fluxes of three components of the magnetic field is shown in Figure 15. We calculate the fluxes of magnetic field through the following three surfaces: the flux of B_r through the part of cylindrical surface $r = 1/2$ limited by lines $z = 0, z = 4, \phi = 0$, and $\phi = \pi/2$; the flux of B_ϕ through the rectangle in the plane $\phi = 0$ limited by lines $z = 0, z = 4, r = R_1$, and $r = R_2$; and the flux of B_z through the half of the ring in the plane $z = -2$ limited by lines $r = R_1, r = R_2, \phi = 0$, and $\phi = \pi$. Then, we divide each of the three fluxes by the areas of the corresponding surfaces. In this way, the values of the magnetic field averaged over the surfaces, $\langle B_r \rangle$, $\langle B_\phi \rangle$, and $\langle B_z \rangle$, are obtained. The time evolution of the logarithms of absolute values of these

averaged values of the magnetic field is presented in Figure 15. All three fluxes grow exponentially (if averaged over fluctuations) with the same growth rate, $\Gamma = 0.026$. The growth rate of the mean square of the magnetic field plotted in Figure 14 is equal to 2Γ , which is consistent with the growth rate of fluxes. The value of $\langle B_\phi \rangle$ is larger than the values of poloidal fluxes, meaning that the toroidal field is predominant in the dynamo, which is also in the agreement with the conclusion from the mean field theory. While radial and toroidal fluxes grow monotonically, the flux of the axial magnetic field experiences oscillations with exponentially growing amplitude. The z -flux remains zero, on average. This is due to the fact that both dipole and quadrupole growing magnetic fields have zero z -flux through the surface described above. However, the z -flux experiences oscillations due to individual plumes creating nonaxisymmetric magnetic field.

The behavior of dynamo magnetic fields immediately outside of the generation region is especially interesting in connection with the magnetic fields in the jets (magnetic helices) and

observed magnetic field in galactic disks. In Figure 16 we plot the fraction of energy of the magnetic field that resides outside of the region of dynamo activity. In particular, we divide the whole computational domain in two; the inner domain is the region $-2 < z < 2$ and $r < 2$, and the outer domain is the rest of the computational domain with $|z| > 2$ or $r > 2$. Initially, the fraction of the outer energy grows because of the diffusion of the initial magnetic field outside the central region (compare the poloidal fields in Figs. 2 and 3). However, after the dynamo action sets in, the skin effect described in § 6.2 and Appendix B occurs. The skin depth of the steadily growing magnetic field, given by equation (B8) for $\eta = 0.01$ and $\Gamma = 0.026$, is $l_s = 0.6$. Thus, the outer domain is in the zone of pure diffusion of the magnetic field, where the variations due to individual plumes are smoothed out. The average value of the outer fraction of the magnetic energy is ≈ 0.06 of the total magnetic energy. This is roughly consistent with the estimate one can obtain from the skin depth analysis of Appendix B, $\sim (0.6/e)^2 \approx 0.05$. The field in the outer region is predominantly even, as is the field in inner region. The time dependence of the fraction of even field in Figure 16 follows closely the time dependence of the fraction of the even field in Figure 14. Note, however, that the curves in Figure 16 are smoother than in Figure 14. Rapid oscillations of the field caused by individual plumes are smoothed out in the diffusion process of the magnetic field into the outer region as the exponential decay scale l_s becomes shorter for higher oscillatory frequencies ω' (Appendix B). Only slow variations with a timescale close to or longer than the diffusive timescale remain present in the outer domain.

Another diagnostic of our simulation is to calculate the time behavior of the magnetic fluxes through the surfaces in the outer part of computational domain. By looking at the time evolution of these fluxes, we can learn about the time evolution of the magnetic field in the asymptotic diffusion region. We calculate magnetic fluxes of a radial magnetic field, or, equivalently, $\langle B_r \rangle$ through the following cylindrical surfaces: radial flux 1 through the part of the surface $r = 2$ limited by lines $\phi = 0$, $\phi = \pi/2$, $z = -1/3$, and $z = 1/3$; radial flux 2 through the part of the surface $r = 3$ limited by lines $\phi = 0$, $\phi = \pi/2$, $z = -1/3$, and $z = 1/3$; radial flux 3 through the part of the surface $r = 3$ limited by lines $\phi = 0$, $\phi = \pi/2$, $z = 2$, and $z = 4$; and radial flux 4 through the part of the surface $r = 3$ limited by lines $\phi = 0$, $\phi = \pi/2$, $z = -4$, and $z = -2$. The first two radial fluxes describe the evolution of the magnetic field close to the equatorial plane. The third and fourth fluxes describe the evolution of the magnetic field in the outer corners of the computational domain. We plot these four radial fluxes in Figure 17. We calculate three fluxes of the toroidal magnetic field, or, equivalently, $\langle B_\phi \rangle$ through the following rectangular areas of the plane $\phi = 0$: toroidal flux 1 through the rectangle limited by lines $r = 2$, $r = 4$, $z = -1/3$, and $z = 1/3$; toroidal flux 2 through the rectangle limited by lines $r = 2$, $r = 4$, $z = 3$, and $z = 4$; and toroidal flux 3 through the rectangle limited by lines $r = 2$, $r = 4$, $z = -4$, and $z = -3$. We plot these three toroidal fluxes in Figure 18. We calculate two fluxes of the axial magnetic field, or, equivalently, $\langle B_z \rangle$ through the following ring-shaped surfaces: axial flux 1 through the quarter of the ring in the plane $z = 2$ limited by the lines $\phi = 0$, $\phi = \pi/2$, $r = 3$, and $r = 4$; and axial flux 2 through the quarter of the ring in the plane $z = -2$ limited by the lines $\phi = 0$, $\phi = \pi/2$, $r = 3$, and $r = 4$. We plot these two axial fluxes in Figure 19. One can see that none of the radial, toroidal, and axial fluxes change sign during the exponential growth of the dynamo (after time $t \approx 100$). Therefore, the star-disk collisions dynamo produces steadily growing nonoscillating magnetic fields. The signs of the fluxes (not shown in Figs. 17–19) are consistent with the quad-

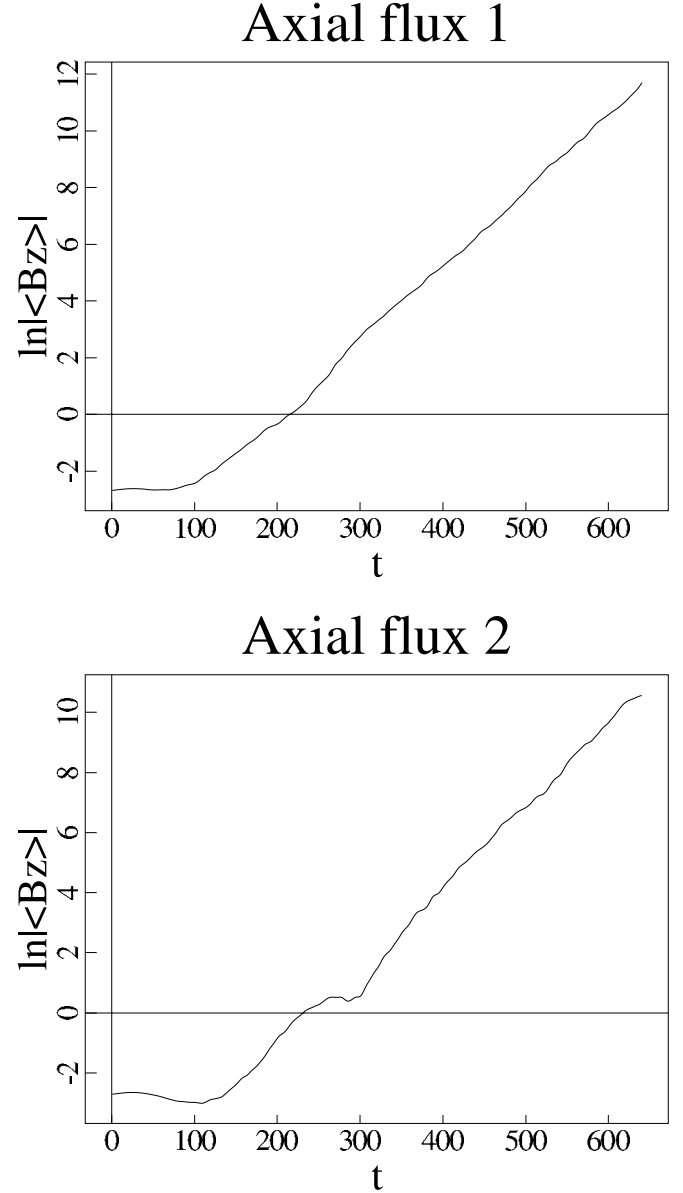
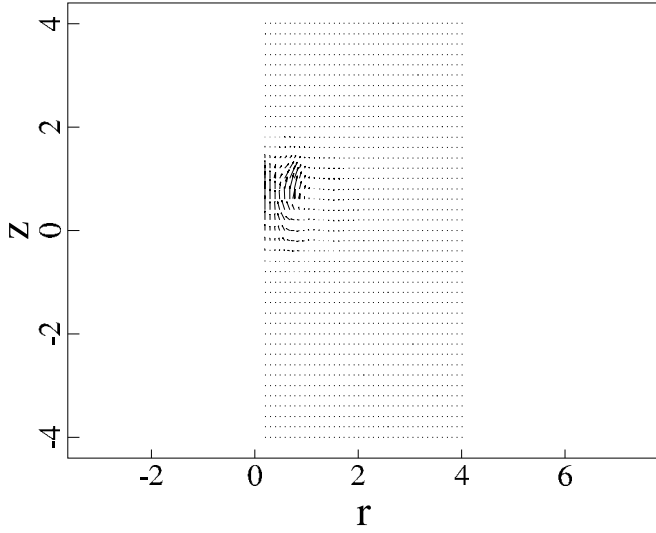


FIG. 19.—Time evolution of logarithms of the absolute values of the axial component of the magnetic field averaged over the two surfaces described in the text. Both surfaces are located in the outer region described in the text.

rupole geometry of the magnetic field in the outer region of the dynamo.

In Figure 20 we show two vector plots of the poloidal magnetic field at the plane $\phi = 0$ at the final moment of the simulation $t = 640$: in the top plot, the length of arrows is proportional to the magnitude of the poloidal magnetic field; on the bottom plot, all arrows have unit length and the direction of the arrows indicate the direction of the same magnetic field as in the top plot. The concentration of the magnetic field toward the central region with the plumes is clearly visible in the top plot. The imaging with arrows picks up only the region of the strong field, while the arrows outside this region are so short that they cannot be pictured at all. The bottom plot illustrates the structure of the poloidal field in the asymptotic outer region. This structure can be described as a “shifted quadrupole,” implying the presence of a significant dipole component. The toroidal field is ~ 20 times stronger than the poloidal. The direction of the toroidal field agrees well with the direction of the field produced by the

Vector plot B



Vector plot B

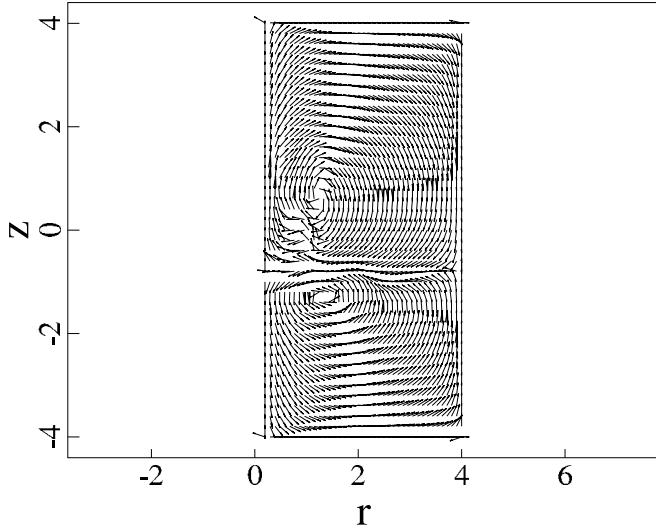


FIG. 20.— Vector plots of the poloidal magnetic field of the growing dynamo at time $t = 640$ in the plane $\phi = 0$. The length of arrows in the top plot is proportional to the magnitude of the poloidal magnetic field. Arrows on the bottom plot have unit length and are directed along the poloidal field.

stretching of the poloidal field by Keplerian differential rotation. The structure of the field at different ϕ -positions is similar to that at $\phi = 0$. The nonaxisymmetric variations of the field are most significant at the location of the plumes at $r \approx 1$ and quickly decay outward. Each individual plume perturbs the magnetic field significantly. This is also reflected in the oscillations of fluxes in Figure 15. The three-dimensional plot of the dynamo magnetic field is presented in Figure 21. Here we plot only the poloidal component of the magnetic field at the two meridional slices, $\phi = \pi/2$ and $\phi = 3\pi/2$, in the computational domain. In order to smooth out the strong contrast between magnitudes of the magnetic field in the inner and outer regions of the computational domain, we plotted a vector field $\mathbf{B}_p/|B_p|^{2/3}$. The dominance of the quadrupole magnetic field in the outer asymptotic region is obvious from Figure 21. In the central region for $r \approx 1$, the field is strongly perturbed by individual plumes, and the nonaxisymmetric field caused by the action of each single plume is visible.

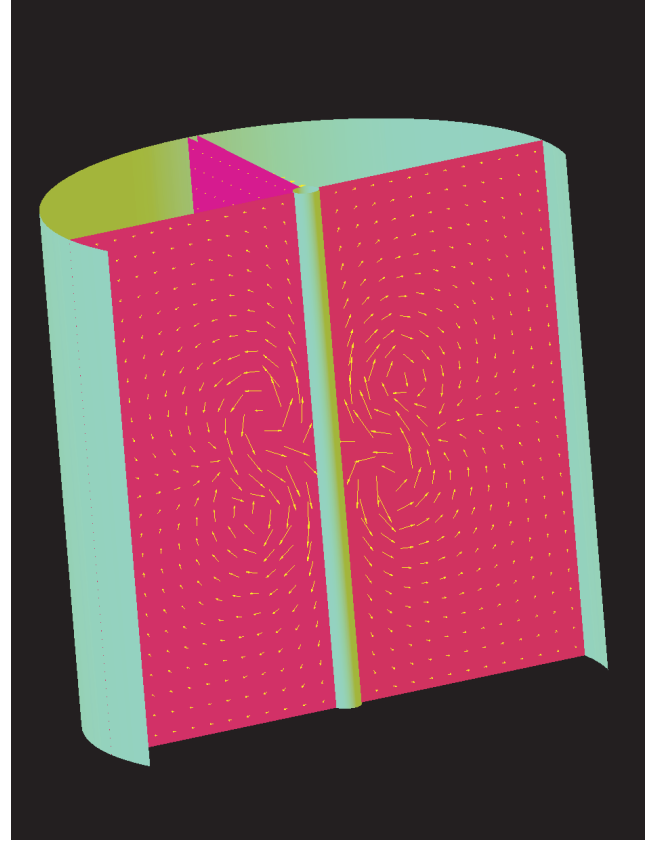


FIG. 21.— Three-dimensional plot of the poloidal magnetic field of the growing dynamo at time $t = 320$. The length of the arrows scales as $1/3$ of the power of the magnitude of the poloidal magnetic field. The magnetic field on the planes $\phi = \pi/2$ and $3\pi/2$ is shown. The boundaries of the cylindrical region are $z = \pm 4$, $R_1 = 0.2$, and $R_2 = 4$.

Toroidal magnetic field is also strongest in the central part of the computational domain.

Finally, let us compare the predictions of the flux rotation and the mean field theories with the results of our numerical simulation. All three predict that the growing magnetic field will be a quadrupole. The simulation formally corresponds to $q \approx \bar{q}_r = (r_{pl}^2/r^2)[(t_d - t_p)/(2\Delta t_p)] = 0.036$, $H = -z_{bot} = 1/3$, and $l = z_{bot} + v_{pz}(t_d - t_p) = 1.24$ in dimensionless units of simulation. Using these parameters and $\alpha_{pl} = 1$ in the expression for the growth rate in the flux rotation theory, equation (24), we obtain $\Gamma = 0.084$. For the mean field theory, expression (37) gives $\beta = 0.09$, the dynamo number (eq. [38]) is $D = -28$, and both expressions (39) and (40) give $\Gamma \approx 0.18$. This is to be compared to numerical growth rate $\Gamma = 0.026$. Both the flux rotation and especially the mean field theory growth rates are higher, but all three are within 1 order of magnitude from each other. Such a result is satisfactory, considering the far-reaching extrapolations of the applicability of both flux rotation and mean field theories.

7. CONCLUSIONS

We believe that by theory and calculation we have demonstrated that a robust α - ω dynamo is likely to occur in conducting accretion disks with a robust source of helicity. Growth rates as large as $\Gamma \simeq 0.1$ – $0.01 \Omega_K$ are expected. We have discussed, in depth, one such source of helicity in the accretion disk forming the central massive black hole of most galaxies. This is the almost inevitable star-disk collisions that should occur in the dense stellar populations at the center of the galaxy. We estimate that

this source of helicity is far larger than necessary for the dynamo fields to reach saturation in less than the formation time of the black hole. Star-disk collisions should also be the most robust source of helicity, because the resulting plumes are driven several scale heights above the surface of the disk as compared to turbulence, where the vertical motions are limited to a fraction of a scale height. The advantage of the α - ω dynamo is that it produces a large-scale coherent field, the poloidal field, outside the disk; the differential winding of this poloidal field leads to a large-scale force-free helix that transports the magnetic energy away from both the disk and the dynamo. The back-reaction of this force-free field (force-free except at the disk surface boundary) only acts as a torque on the Keplerian flow, and thus the field energy of the force-free helix can grow at the expense of the free energy of formation of the black hole. The back-reaction of this force-free field, being much smaller than the toroidal field, does not affect the plume formation by star-disk collisions. Only the much larger toroidal field affects the plumes, and this in turn must be less than the pressure inside the disk. Thus, star-disk collisions produce a robust dynamo in which the back-reaction does not quench the dynamo action at low values of field. The resulting exponential gain of this dynamo is an instability converting kinetic to magnetic energy. Since the gain is large, the dynamo fields should rapidly grow to saturation or the back-reaction limit. This limit we conjecture is the torque corresponding to the ac-

cretion flow of angular momentum away from the black hole. Hence, the dynamo should convert a large fraction of the free energy of the black hole formation to magnetic energy.

V. P. is pleased to thank Richard Lovelace and Eric Blackman for helpful discussions and Benjamin Bromley for support with computer simulations. Eric Blackman is thanked again for his support during the late stages of this work. The facilities and interactions of Aspen Center for Physics are gratefully acknowledged, and particular support has been given by Hui Li through the support of the Director Funded Research, “Active Galaxies.” We are particularly pleased to acknowledge the careful reading of the text by the anonymous referee and furthermore the significant improvement of readability and putting our work in more perspective due to the referee’s efforts. This work has been supported by the US Department of Energy through the LDRD program at Los Alamos National Laboratory. V. P. also acknowledges partial support by DOE grant DE-FG02-00ER54600 and by the Center for Magnetic Self-Organization in the Laboratory and Astrophysical Plasmas at the University of Wisconsin-Madison. The Cray supercomputer used in this research was provided through funding from the NASA Offices of Space Sciences, Aeronautics, and Mission to Planet Earth.

APPENDIX A

ON THE PARITY OF MAGNETIC FIELDS

Any arbitrary vector field $\mathbf{C} = \mathbf{C}(r, \phi, z)$ can be decomposed into the sum of parts that are even and odd with respect to the reflection $z \rightarrow -z$, $\mathbf{C} = \mathbf{C}^e + \mathbf{C}^o$. The following symmetry rules are valid for an even field:

$$C_r^e(-z) = C_r^e(z), \quad C_\phi^e(-z) = C_\phi^e(z), \quad C_z^e(-z) = -C_z^e(z), \quad (\text{A1})$$

and for an odd field:

$$C_r^o(-z) = -C_r^o(z), \quad C_\phi^o(-z) = -C_\phi^o(z), \quad C_z^o(-z) = C_z^o(z). \quad (\text{A2})$$

Often even fields are called quadrupole-type fields and odd fields are called dipole-type fields. This terminology reflects the largest scale modes possible within each symmetry class and allows one to visualize fields of each symmetry type easily. The even and odd decompositions of an arbitrary field \mathbf{C} are

$$C_r^e(r, \phi, z) = \frac{1}{2} [C(r, \phi, z) + C(r, \phi, -z)], \quad (\text{A3a})$$

$$C_\phi^e(r, \phi, z) = \frac{1}{2} [C(r, \phi, z) + C(r, \phi, -z)], \quad (\text{A3b})$$

$$C_z^e(r, \phi, z) = \frac{1}{2} [C(r, \phi, z) - C(r, \phi, -z)], \quad (\text{A3c})$$

$$C_r^o(r, \phi, z) = \frac{1}{2} [C(r, \phi, z) - C(r, \phi, -z)], \quad (\text{A3d})$$

$$C_\phi^o(r, \phi, z) = \frac{1}{2} [C(r, \phi, z) - C(r, \phi, -z)], \quad (\text{A3e})$$

$$C_z^o(r, \phi, z) = \frac{1}{2} [C(r, \phi, z) + C(r, \phi, -z)]. \quad (\text{A3f})$$

One can check that for any volume V symmetric with respect to the plane $z = 0$,

$$\int_V \mathbf{C}^2 dV = \int_V (\mathbf{C}^e)^2 dV + \int_V (\mathbf{C}^o)^2 dV. \quad (\text{A4})$$

This implies that if $\mathbf{C} = \mathbf{B}$ is a magnetic field, then the energy of the magnetic field is equal to the sum of the energies of its even and odd components. The even and odd components of solutions of equations (34) and (35) decouple if the mean velocity field is even,

$v_{Pr}(-z) = v_{Pr}(z)$, $v_{Pz}(-z) = -v_{Pz}(z)$, $\Omega(-z) = \Omega(z)$, the coefficient α is antisymmetric with respect to reflection $z \rightarrow -z$, and the coefficient β is symmetric with respect to reflection $z \rightarrow -z$. Thus, even (quadrupole) and odd (dipole) modes will have different growth rates. The axisymmetric magnetic field is even if $A(-z) = -A(z)$ and $B_\phi(z) = B_\phi(-z)$ and is odd if $A(-z) = A(z)$ and $B_\phi(-z) = -B_\phi(z)$.

APPENDIX B

SKIN EFFECT FOR THE MAGNETIC DYNAMO

Let us consider equation (72) written in spherical coordinates ϱ , θ , and ϕ such that $\theta = 0$ and π corresponds to the symmetry axis of the system. In the case of time-dependent flow described in § 6.1 there are no eigenmodes with a fixed frequency. Instead, the magnetic field can be represented as an integral over frequencies in the Fourier transform. However, in the case of a growing (and possibly oscillating) magnetic field, there is a characteristic growth rate Γ of the dynamo averaged over plume pulses. In addition, the magnetic field will possess oscillating Fourier components associated with the period of the emergence of plumes and, possibly, some intrinsic oscillatory behavior of the dynamo. We consider the behavior of one such Fourier component assuming the dependence $A \propto \exp(-i\omega t)$, where the complex ω is the sum of the real and imaginary parts as $\omega = \omega' + i\Gamma$. Here, Γ is the average growth rate of the dynamo, while ω' can take on a whole range of values, including the frequency of plumes, the Keplerian period, all its harmonics, etc. We impose the boundary condition for A on some sphere of radius ϱ_{in} such that $\varrho_{\text{in}} > 1$, but ϱ_{in} still is of the order of 1. We assume that the value of A at $\varrho = \varrho_{\text{in}}$ is dictated by the dynamo process inside ϱ_{in} . Then, for one Fourier component, equation (72) becomes

$$-i\omega \frac{A}{\eta} = \frac{1}{\varrho^2} \frac{\partial}{\partial \varrho} \left(\varrho^2 \frac{\partial A}{\partial \varrho} \right) + \frac{1}{\varrho^2} \hat{L} A, \quad (\text{B1})$$

where

$$\hat{L} = \frac{1}{\sin \theta} \frac{\partial}{\partial \theta} \left(\sin \theta \frac{\partial}{\partial \theta} \right) - \frac{1}{\sin^2 \theta}$$

is the angular operator acting on A . In spherical geometry, equation (B1) has separable variables ϱ and θ . Thus, we look for solutions in the form $A = R_l(\varrho) Q_l(\theta) \exp(-i\omega t)$.

The operator \hat{L} commonly occurs in problems with axisymmetric flows, when solving the equation for the stream function. Since the magnetic field should be finite on the axis $\theta = 0$, the quantity

$$\frac{1}{\sin \theta} \frac{\partial}{\partial \theta} (\sin \theta A)$$

must be finite at $\theta = 0$ and π , because $\mathbf{B}_P = \nabla \times (A \mathbf{e}_\phi)$. The eigenvalues and eigenfunctions $\hat{L} Q_l = \lambda_l Q_l$ satisfying these boundary conditions are

$$\lambda_l = -l(l+1), \quad Q_l = \sin \theta P'_l(\cos \theta), \quad (\text{B2})$$

where prime denotes the differentiation of the Legendre polynomial $P_l(x)$ with respect to x and $l = 1, 2, 3, \dots$. Besides these eigenvalues, $\lambda = 0$ is also an eigenvalue with the eigenfunction $Q_0 = (1 - \cos \theta)/\sin \theta$. The first three eigenfunctions given by formula (B2) are

$$Q_1 = \sin \theta, \quad Q_2 = \sin \theta \cos \theta, \quad Q_3 = \sin \theta \left(\cos^2 \theta - \frac{1}{5} \right). \quad (\text{B3})$$

The angular dependence $Q_l(\theta)$ determines the symmetry of the solutions. The mode proportional to Q_0 describes the radially directed magnetic field with nonzero total flux through the sphere from $\theta = 0$ to π . All terms with $l \geq 1$ correspond to the magnetic field with vanishing total flux through the sphere from $\theta = 0$ to π . The Q_0 term cannot be excited by the dynamo operating inside ϱ_{in} because of the $\nabla \cdot \mathbf{B} = 0$ condition. This is also clear from the fact that $Q_0 \rightarrow \infty$ when $\theta \rightarrow \pi$, which means that the vector potential cannot be well defined for a magnetic field with $\nabla \cdot \mathbf{B} \neq 0$. The terms with $l \geq 1$ represent multipole expansion of the magnetic field in the far zone of the generation region; $R_1(\varrho) Q_1(\theta)$ is a dipole term, $R_2(\varrho) Q_2(\theta)$ is a quadrupole term, and so on.

For the radial part of the solution we obtain the equation

$$\frac{d^2 R_l}{d\varrho^2} + \frac{2}{\varrho} \frac{dR_l}{d\varrho} - \frac{l(l+1)}{\varrho^2} R_l - \frac{\Gamma - i\omega'}{\eta} R_l = 0. \quad (\text{B4})$$

We introduce a new variable $z = \varrho/\chi$ where

$$\chi^2 = \frac{\eta(\Gamma + i\omega')}{\Gamma^2 + \omega'^2}. \quad (\text{B5})$$

Then, equation (B4) reduces to the Bessel equation of imaginary argument. Solutions of this equation, which vanishes at $\varrho \rightarrow \infty$, are given in terms of modified Bessel function $K_\nu(z)$ as

$$R_l = \sqrt{\frac{\pi}{2z}} K_{l+1/2}(z).$$

The Bessel functions of half-integer order can be expressed through elementary functions (e.g., Abramowitz & Stegun 1972). Thus, we obtain for the dipole and quadrupole terms

$$R_1(z) = \frac{\pi}{2z} e^{-z} \left(1 + \frac{1}{z}\right), \quad R_2 = \frac{\pi}{2z} e^{-z} \left(1 + \frac{3}{z} + \frac{3}{z^2}\right).$$

Finally, collecting all the terms together and retaining only the leading dipole and quadrupole terms, we obtain the following solution for A

$$A = a_1 \sin \theta \frac{\pi\chi}{2\varrho} e^{-\varrho/\chi} \left(1 + \frac{\chi}{\varrho}\right) e^{-i\omega t} + a_2 \sin \theta \cos \theta \frac{\pi\chi}{2\varrho} e^{-\varrho/\chi} \left(1 + \frac{3\chi}{\varrho} + \frac{3\chi^2}{\varrho^2}\right) e^{-i\omega t}, \quad (\text{B6})$$

where the coefficients a_1 and a_2 should be determined by the condition of the continuity of harmonics of A at the surface $\varrho = \varrho_{\text{in}}$. The values of a_1 and a_2 are determined by the dynamo action inside the radius ϱ_{in} . We see that both dipole and quadrupole components (and all higher multipole components) decay as $\propto e^{-\varrho/\chi}$. Using expression (B5) for χ , we obtain

$$e^{-\varrho/\chi} = \exp\left(-\frac{\varrho}{\sqrt{2\eta}} \sqrt{(\Gamma^2 + \omega'^2)^{1/2} + \Gamma} + i \frac{\varrho}{\sqrt{2\eta}} \sqrt{(\Gamma^2 + \omega'^2)^{1/2} - \Gamma}\right), \quad (\text{B7})$$

where we assume $\Gamma > 0$ and $\omega' > 0$. The thickness of the skin layer is determined by the real part of the expression under the exponent in equation (B7). The larger the growth rate Γ , the faster the magnetic field decays with the radius. Also, oscillating modes with $\omega' > 0$ decay faster with the radius than the steady modes with $\omega' = 0$. Thus, far from the dynamo source one should expect the magnetic field to be growing in time, steadily, without oscillations.

The characteristic length of the exponential decay of the field, l_s , is found from equation (B7) to be

$$l_s = \sqrt{\frac{2\eta}{(\Gamma^2 + \omega'^2)^{1/2} + \Gamma}}. \quad (\text{B8})$$

For a steady magnetic field, $l_s = (\eta/\Gamma)^{1/2}$. When ϱ is approaching the radius of the outer boundary R_2 , the solution (eq. [B6]) starts to “feel” the boundary condition as an ideally conducting boundary, and the numerical results at $\varrho \geq R_2$ are not approximated by formula (B6).

REFERENCES

- Abramowitz, M., & Stegun, I. A. 1972, *Handbook of Mathematical Functions* (New York: Dover)
- Bayliss, R. A., Forest, C. B., Nornberg, M. D., Spence, E. J., & Terry, P. W. 2006, *Phys. Rev. E*, submitted (physics/0602126)
- Beckley, H. F., Colgate, S. A., Romero, V. D., & Ferrel, R. 2003, *ApJ*, 599, 702
- Biskamp, D. 1993, *Nonlinear Magnetohydrodynamics* (Cambridge: Cambridge Univ. Press)
- Blackman, E. G., & Brandenburg, A. 2003, *ApJ*, 584, L99
- Blandford, R. D., & Payne, D. G. 1982, *MNRAS*, 199, 883
- Boldyrev, S. A. 2006, *Phys. Rev. Lett.*, 96, 115002
- Boldyrev, S. A., & Cattaneo, F. 2004, *Phys. Rev. Lett.*, 92, 144501
- Bondi, H. 1952, *MNRAS*, 112, 195
- Bondi, H., & Hoyle, F. 1944, *MNRAS*, 104, 273
- Bondi, H., Hoyle, F., & Lyttleton, R. A. 1947, *MNRAS*, 107, 184
- Bourgoin, M., Odier, P., Pinton, J.-F., & Ricard, Y. 2004, *Phys. Fluids*, 16, 2529
- Bourgoin, M., et al. 2002, *Phys. Fluids*, 14, 3046
- Busse, F. H. 1991, in *Advances in Solar System Magnetohydrodynamics*, ed. E. R. Priest & A. W. Hood (Cambridge: Cambridge Univ. Press), 51
- Chakrabarti, S. K., Rosner, R., & Vainshtein, S. I. 1994, *Nature*, 368, 434
- Childress, S., Collet, P., Frish, U., Gilbert, A. D., Moffatt, H. K., & Zaslavsky, G. M. 1990, *Geophys. Astrophys. Fluid Dyn.*, 52, 263
- Colgate, S. A., Cen, R., Li, H., Currier, N., & Warren, M. S. 2003, *ApJ*, 598, L7
- Colgate, S. A., & Li, H. 1997, in *Relativistic Jets in AGNs*, ed. M. Ostrowski (Krakow: Poland), 170
- . 1999, *Ap&SS*, 264, 357
- Colgate, S. A., Li, H., & Pariev, V. I. 2001, *Phys. Plasmas*, 8, 2425
- Cowling, T. G. 1981, *ARA&A*, 19, 115
- Dudley, M. L., & James, R. W. 1989, *Proc. R. Soc. London A*, 425, 407
- Ferrière, K. 1993a, *ApJ*, 404, 162
- . 1993b, *ApJ*, 409, 248
- . 1998, *A&A*, 335, 488
- Ferrière, K., & Schmitt, D. 2000, *A&A*, 358, 125
- Finn, J. M. 1992, in *AIP Conf. Proc. 267, Electromechanical Coupling of the Solar Atmosphere*, ed. D. S. Spicer & P. MacNeice (New York: AIP), 79
- Finn, J. M., Ott, E., Hanson, J. D., & Kan, I. 1991, *Phys. Fluids B*, 3, 1250
- Fletcher, C. A. J. 1992, *Computational Techniques for Fluid Dynamics* (Heidelberg: Springer)
- Frolov, V. P., & Novikov, I. D. 1998, *Black Hole Physics: Basic Concepts and New Developments* (Dordrecht: Kluwer)
- Gailitis, A., & Freiberg, Ya. 1976, *Magnetohydrodynamics*, 12, 127
- Gailitis, A., Lielausis, O., Dement'ev, S., et al. 2000, *Phys. Rev. Lett.*, 84, 4365
- Gailitis, A., et al. 2001, *Phys. Rev. Lett.*, 86, 3024
- Goldreich, P., & Sridhar, S. 1995, *ApJ*, 438, 763
- Hoyle, F. 1949, *Some Recent Researches in Solar Physics* (Cambridge: Cambridge Univ. Press)
- Iroshnikov, P. S. 1963, *Astron. Zh.*, 40, 742
- Khanna, R., & Camenzind, M. 1996a, *A&A*, 307, 665
- . 1996b, *A&A*, 313, 1028
- Kraichnan, R. H. 1965, *Phys. Fluids*, 8, 1385
- Krause, F., & Rädler, K. H. 1980, *Mean-Field Magnetohydrodynamics and Dynamo Theory* (Oxford: Pergamon Press)
- Kronberg, P. P., Dufton, Q. W., Li, H., & Colgate, S. A. 2001, *ApJ*, 560, 178
- Kulsrud, R. M. 1999, *ARA&A*, 37, 37
- Lau, Y.-T., & Finn, J. M. 1993, *Phys. Fluids B*, 5, 365

- Laval, J.-P., Blaineau, P., Leprovost, N., Dubrulle, B., & Daviaud, F. 2006, *Phys. Rev. Lett.*, 96, 204503
- Li, H., Colgate, S. A., Wendroff, B., & Liska, R. 2001a, *ApJ*, 551, 874
- Li, H., Finn, J. M., Lovelace, R. V. E., & Colgate, S. A. 2000, *ApJ*, 533, 1023
- Li, H., Lovelace, R. V. E., Finn, J. M., & Colgate, S. A. 2001b, *ApJ*, 561, 915
- Lovelace, R. V. E., Li, H., Colgate, S. A., & Nelson, A. F. 1999, *ApJ*, 513, 805
- Marić, L., Burguete, J., Daviaud, F., & Léorat, J. 2003, *European J. Phys. B*, 33, 469
- McCrea, W. H. 1953, *MNRAS*, 113, 162
- Mestel, L. 1999, *Stellar Magnetism* (Oxford: Clarendon)
- Moffatt, H. K. 1978, *Magnetic Field Generation in Electrically Conducting Fluids* (Cambridge: Cambridge Univ. Press)
- Molchanov, S. A., Ruzmaikin, A. A., & Sokoloff, D. D. 1983, *Magnetohydrodynamics*, 19, 402
- Nornberg, M. D., Spence, E. J., Kendrick, R. D., & Forest, C. B. 2006, *Phys. Plasmas*, 13, 055901
- O'Connell, R., Kendrick, R. D., Nornberg, M. D., Spence, E. J., Bayliss, R. A., & Forest, C. B. 2001, in *Dynamo and Dynamics: A Mathematical Challenge*, ed. P. Chossat, D. Ambruster, & I. Oprea (Dordrecht: Kluwer), 59
- Pariev, V. I., & Colgate, S. A. 2007, *ApJ*, in press (Paper I)
- Parker, E. N. 1955, *ApJ*, 122, 293
- . 1979, *Cosmical Magnetic Fields: Their Origin and Their Activity* (Oxford: Clarendon)
- Peffley, N. L., Cawthorne, A. B., & Lathrop, D. P. 2000, *Phys. Rev. E*, 61, 5287
- Pétrélis, F., et al. 2003, *Phys. Rev. Lett.*, 90, 174501
- Ponomarenko, Yu. B. 1973, *J. Appl. Mech. Tech. Phys.*, 14, 775
- Ponty, Y., Mininni, P. D., Montgomery, D. C., Pinton, J.-F., Politano, H., & Pouquet, A. 2005, *Phys. Rev. Lett.*, 94, 164502
- Priest, E. R. 1982, *Solar Magneto-hydrodynamics* (Boston: Kluwer)
- Reyes-Ruiz, M., & Stepinski, T. F. 1999, *A&A*, 342, 892
- Roberts, P. H., & Soward, A. M. 1992, *Ann. Rev. of Fluid Mechanics*, 24, 459
- Ruzmaikin, A. A., Sokoloff, D. D., & Shukurov, A. M. 1988, *Magnetic Fields of Galaxies* (Moscow: Nauka)
- Sakharov, A. D. 1982 *Divertissement 11*, in *Collected Scientific Works* (New York: Marcel Dekker) 285
- Shakura, N. I. 1972, *Astron. Zh.*, 49, 921
- Shakura, N. I., & Sunyaev, R. A. 1973, *A&A*, 24, 337
- Sisan, D. R., Mujica, N., Tillotson, W. A., Huang, Y.-M., Dorland, W., Hassam, A. B., Antonsen, T. M., & Lathrop, D. P. 2004, *Phys. Rev. Lett.*, 93, 114502
- Sovinec, C. R., Finn, J. M., & del-Castillo-Negrete, D. 2001, *Phys. Plasmas*, 8, 475
- Spence, E. J., Nornberg, M. D., Jacobson, C. M., Kendrick, R. D., & Forest, C. B. 2006, *Phys. Rev. Lett.*, 96, 055002
- Steenbeck, M., Krause, F., & Rädler, K. H. 1966, *Z. Naturforsch.*, 21, 369
- Stepinski, T. F., & Levy, E. H. 1988, *ApJ*, 331, 416
- Stieglitz, R., & Müller, U. 2001, *Phys. Fluids*, 13, 561
- Stix, M. 1975, *A&A*, 42, 85
- Sweet, D., Ott, E., Antonsen, T. M., Lathrop, D. P., & Finn, J. M. 2001, *Phys. Plasmas*, 8, 1944
- Vainshtein, S. I., & Zeldovich, Ya. B. 1972, *Soviet Phys.-Uspekhi*, 15, 159
- Zeldovich, Ya. B., Ruzmaikin, A. A., & Sokoloff, D. D. 1983, *Magnetic Fields in Astrophysics* (New York: Gordon and Breach Science Publishers)